



The
University
Of
Sheffield.

Assessing The Volatility Of Caesium During The Vitrification Of Intermediate Level Waste

Joshua T. Radford, BEng(Hons)

A thesis submitted in partial fulfilment for the degree of Doctor of Philosophy

Immobilisation Science Laboratory

Department of Materials Science and Engineering

University of Sheffield

Sponsored by the EPSRC and National Nuclear Laboratory as part of an iCASE award



Engineering and
Physical Sciences
Research Council

NucleUS
Immobilisation Science Laboratory



Acknowledgements

Firstly, a slightly more formal acknowledgment needs to go to the CINDE project, as the Raman spectrometer used in the off-gas system was purchased with funds from this project. Without this, it is unlikely my thesis would be half as interesting, or useful. I'd also like to thank my industrial sponsor, the National Nuclear Laboratory and in particular Charlie Scales. Charlie just let me get on with things and was always available when help was needed.

It goes without saying that I am extremely grateful for the support of my supervisors. I can honestly say that it has been a pleasure to work with Russell for both my undergraduate final year project and throughout my PhD. I'm still scared by how much Russell knows about glass and I suspect that I'll need to be in academia for several more decades before that feeling goes away. Russell has allowed me almost free rein over this project, always supporting my ideas and I hope to continue collaborating in the future.

I'd also like to thank my parents, I still don't think my mum really knows what I do, but she keeps saying she's proud of me, so thanks mum!

Sarah – how you've put up with me being during my thesis writing stage, locked up together thanks to covid, I don't know, but your support has always been appreciated.

Lisa – Who else would I go to, to ask the stupid questions I'm too embarrassed to ask Russell. From answering my questions to unsticking expensive DSC components from faulty crucibles, you've always been there to help and I can't thank you enough.

I've also met some great people working within the ISL and I'd like to thank you all for putting up with me. Particular thanks go to Dan, Martin, Sam, Seb and Shishir, we could probably have funded a PhD with the amount we've spent in various pubs, but I like to think we're just really keen to help the local economy. Safe to say that without you guys this entire experience would have been far less enjoyable.

I'm also thankful to the great postdoc team that helped me out with everything from ICP to welding. In particular, I have to thank Colleen, I have no idea why you had so much faith in me, but it's very much appreciated! Dan B, Sam and Laura also deserve thanks, usually for helping me with time wasting side projects but it was all good fun.

To anyone that I've missed – sorry! I'll buy you a pint.

Abstract

Thermal treatment of the UK's intermediate level nuclear waste, such as vitrification, offers significant long-term storage savings compared to cementation. However, concerns exist surrounding the volatility of components present in intermediate level waste streams that must be addressed for thermal treatment to be a viable immobilisation option. Of particular interest are caesium radioisotopes, which account for a large proportion of the radioactivity in intermediate level waste.

This thesis aims to assess the volatility of caesium species during vitrification using a bespoke laboratory apparatus, allowing for in-situ assessment of the volatile species produced. This information can be fed back into the glass formulation to minimise/eliminate volatility during vitrification.

A bespoke, in-situ off-gas capture and analysis system has been designed and commissioned to enable this work, briefly comprising of a gas tight stainless steel system, a fibre coupled Raman spectrometer, connected to the steel apparatus using a quartz window Raman flow cell and gas washing bottles to allow for the analysis of off-gas solutions to aid a caesium mass balance.

To aid the identification of caesium bearing volatiles produced during the glass melts, trials were conducted in the system described above using caesium carbonate, caesium borate, and a mixed alkali borate. The purpose of these trials was to collect reference spectra of known volatile caesium species in the same experimental apparatus as the glass melts were to be conducted in.

Two glass series were designed to facilitate this work, an iron phosphate series and a sodium borosilicate series. Alkali borosilicate glasses are the most commonly used glass type for the immobilisation of high activity nuclear waste, in this work, the influence of additives (CaO and ZnO) on caesium retention during the vitrification process were investigated. The results presented in this thesis feed into the wider body of research conducted on the effect of CaO and ZnO on glass structure, which in turn influences important properties such as chemical durability and wastestream solubility. Iron phosphate glasses were selected for this study as a promising candidate for UK wastestreams that are poorly suited to borosilicate glasses. Both glass types were thoroughly analysed before being re-melted with varying caesium oxide waste loadings in the system described above.

The iron phosphate glass series investigated three additives, B_2O_3 , MnO and ZnO . Each of the additives were substituted into a $40Fe_2O_3-60P_2O_5$ iron phosphate system in place of Fe_2O_3 . The main aim of studying a range of additives at varying concentration was to investigate their effect on caesium retention, however each additive was expected to influence the glass system in a different way. B_2O_3 was selected to investigate the relationship between B_2O_3 and caesium volatility at varying B_2O_3 concentrations, as the existence of caesium borate species above glass melts has been demonstrated in the literature. MnO was selected to investigate the relationship between the iron oxidation state and caesium retention, as Mn was expected to form a redox couple with the Fe present in the glass system. Finally, ZnO was selected as studies conducted on borosilicate glass systems have shown ZnO to have a positive influence on caesium retention and this study aimed to investigate if the same effect would be observed in an iron phosphate glass system. It was found that B_2O_3 and ZnO additions improve caesium retention, whilst MnO additions showed minimal improvement when compared to the $40Fe_2O_3-60P_2O_5$ system. All glasses with additive concentrations of less than 7.5 mol% crystallised during the caesium doped remelt, with B_2O_3 melts crystallising regardless of the additive concentration. Glasses containing 7.5 and 10 mol% MnO or ZnO remained amorphous after the caesium doped remelt with Raman spectroscopy of the bulk glass indicating no significant structural changes.

The sodium borosilicate system investigated the influence of ZnO on caesium volatility, using a modified version of the UK'S CaZn composition, which is currently used to immobilise high level waste in the UK. Glasses with varying Zn:Ca ratios (100:0 to 20:80) were produced and remelted at Cs_2O waste loadings of 2, 5, and 10 wt.%. A correlation was found between the measured Zn:Ca ratio and caesium retention. Glasses with low ZnO concentrations performed worse than the glasses with higher ZnO concentration. However, the NaBSZn100Ca0 composition did not perform as well as glasses containing CaO. Off-gas Raman analysis of the caesium vapours showed that at Cs_2O loadings of 5 and 10 wt.%, a mixed alkali borate ($NaCs(BO_2)_2$) species was the dominant volatile identified. At the 2 wt.% Cs_2O loading, the off-gas Raman spectra indicated that a caesium borate species was dominant. Importantly, this work showed that off-gas Raman spectroscopy can be used to detect differences in caesium volatiles during thermal treatments such as vitrification.

Overall, the NaBS series performed better than the IPG series in terms of caesium retention. However, it would be useful for further studies to compare the two glass systems at similar viscosities rather than arbitrary melting temperatures.

Contents

List of Figures	viii
List of Tables	xiii
List of Acronyms	xiv
1 Introduction	1
2 Project Objectives	4
2.1 Project Methodology	4
3 Literature Review	6
3.1 Oxide Glasses	6
3.1.1 Glass Formation and Transformation Behaviour	9
3.1.2 Effect of Alkali and Alkaline Earth Additions to Different Glass Systems	10
3.2 Nuclear Waste	13
3.3 Sodium Borosilicate Glasses	15
3.3.1 Caesium volatilisation from borate and borosilicate melts	19
3.4 Iron Phosphate Glasses	21
3.5 Concluding Remarks	27
4 Experimental Methods	28
4.1 Base Glass Preparation	28
4.2 Caesium Doped Glass Melts	29
4.3 Analytical Sample Preparation	29
4.3.1 As-Cast Monolith Samples	29
4.3.2 Powder Samples	30
4.3.3 Pellets	30
4.3.4 Off-gas Solutions	31
4.4 Density Measurements	31
4.5 X-Ray Diffraction	31

4.5.1	Bruker D2 Phaser	31
4.5.2	Panalytical XPert3	31
4.5.3	Phase Identification	31
4.6	Induced Coupled Plasma – Mass Spectroscopy	32
4.7	XRF Spectroscopy	32
4.8	Mössbauer Spectroscopy	32
4.9	Raman Spectroscopy	33
4.9.1	Bulk Studies	33
4.9.2	Gas State Raman Spectroscopy	33
4.9.3	Analysis and Data Treatment of Solid-State Raman Spectra	33
4.10	Scanning Electron Microscopy (SEM)	33
4.11	Thermal Analysis	34
4.12	Design and Modification of Off-gas System	35
4.12.1	Design Criteria	35
4.12.2	Initial Design	36
4.12.3	Second Iteration of Off-Gas Design	39
4.12.4	Final Design Used in This Work	41
5	Raman Spectroscopy	45
5.1	Basic Theory	45
5.2	Temperature corrections	48
5.3	Raman Spectroscopy and glasses	49
5.4	Vibrational Modes of Cs Containing Compounds	51
5.5	Raman Spectroscopy and Gases	52
5.6	Current Experimental Apparatus	53
5.7	Data Treatment	54
5.8	Initial Caesium Oxide and Caesium Borate Trials	55
6	Iron Phosphate Glasses	58
6.1	Introduction	58

6.2	XRD	59
6.3	Thermal Analysis	63
6.4	Raman Spectroscopy	67
6.6	Deconvolution of the main Raman band	74
6.7	Mössbauer Spectroscopy	76
6.8	Compositional Data, Density Measurements and Caesium Retention	80
6.9	SEM	84
6.10	Discussion	87
6.11	Conclusions	90
7	Sodium Borosilicate Glasses	91
7.1	Introduction	91
7.2	XRD	92
7.3	Thermal Analysis	94
7.4	Raman Spectroscopy of the bulk glasses	96
7.5	Deconvolution of the main Raman band	101
7.6	Compositional Analysis and Density Measurements	104
7.7	SEM	108
7.8	Off-gas Raman Spectroscopy	109
7.9	Discussion	115
7.10	Conclusion	120
8	Discussion	121
9	Conclusions and Further Work	123
9.1	Conclusions of Work to Date	123
9.2	Suggestions for Further Work	124
10	References	126

11	Appendix	136
11.1	Appendix A	136
11.2	Appendix B	136
11.3	Appendix C	137

List of Figures

Figure 3.1: Oxygen bonding variation due to sodium content.....	8
Figure 3.2: Enthalpy-Temperature diagram of glass formation.....	9
Figure 3.3: Q-speciation in silicate glasses.....	10
Figure 3.4: Q-speciation in phosphate glasses.....	11
Figure 3.5: Alkali bonding in phosphate structures. Left: Coordination number of alkali ion < number of TO. Right: Coordination number of alkali ion > number of TO.....	12
Figure 3.6: Wastestreams found in ILW waste in the UK (Data from 2019 Waste Inventory Report [1]).....	14
Figure 3.7: ZnO addition to a borosilicate network [42]	18
Figure 3.8: Mass loss behaviour of various volatiles at several temperatures.....	19
Figure 4.1: Schematic of apparatus used by Kamizono et al.....	36
Figure 4.2: Schematic of apparatus used by Sill et al.....	37
Figure 4.3: Schematic of apparatus used by Banerjee et al.	37
Figure 4.4: Left - Standard HIP Canister, Right - Modified HIP canister.....	38
Figure 4.5: First Iteration of Off-Gas Design	39
Figure 4.6: Second iteration of off-gas design.....	40
Figure 4.7: Scaling observed in 316 stainless steel canisters. Left: Inside surface of the lid, right: external scaling.....	40
Figure 4.8: Third iteration of off-gas system.....	41
Figure 4.9: Final design for off-gas system with in-situ Raman spectrometer.....	42
Figure 4.10: Caesium concentrations in off-gas wash through solutions (top=expected Cs concentrations, bottom = measured Cs concentrations)	43
Figure 5.1 - Energy levels for Raman shift. Reproduced from [99].....	46
Figure 5.2: Schematic of experimental apparatus used for in-situ Raman spectroscopy experiments.....	53

Figure 5.3: A comparison of CeO ₂ Raman spectra collected on the Renishaw InVia spectrometer (solid blue line) and the spectra collected using the QEPro spectrometer (solid red orange line=raw data, dot-dash line= corrected data).....	54
Figure 5.4: Off-gas Raman spectra of Cs ₂ O, CsBO ₂ and NaCs(BO ₂) ₂ samples	55
Figure 6.1: XRD of IPG-Base Glass.....	59
Figure 6.2: XRD of IPG-B Series	59
Figure 6.3: XRD of IPG-Mn Series	60
Figure 6.4: XRD of IPG-Zn Series	60
Figure 6.5: XRD of IPG-Base-2Cs and IPG-B-2Cs Series.....	61
Figure 6.6: XRD of IPG-Mn-2Cs series	62
Figure 6.7: XRD of IPG-Zn-2Cs series	62
Figure 6.8: DTA trace of IPG-Base	63
Figure 6.9: DTA traces of IPG-B Series.....	64
Figure 6.10: DTA traces of IPG-Mn Series	64
Figure 6.11: DTA traces of IPG-Zn Series	65
Figure 6.12: Raman spectra of IPG-Base Glass.....	67
Figure 6.13: Raman spectra of IPG-B Series.....	68
Figure 6.14: Residual difference between IPG-Base and IPG-B series.....	68
Figure 6.15: Raman spectra of IPG-Mn Series.....	69
Figure 6.16: Residual difference between IPG-Base and IPG-Mn series.....	69
Figure 6.17: Raman spectra of IPG-Zn Series	70
Figure 6.18: Residual difference between IPG-Base and IPG-Zn series.....	70
Figure 6.19: Raman spectra of IPG-Base-2Cs and IPG-B-2Cs series.....	71
Figure 6.20: Raman spectra of IPG-Mn-2Cs series	71
Figure 6.21: Raman spectra of IPG-Zn-2Cs series	72
Figure 6.22: A comparison of the Raman spectra of IPG-Mn7.5 and IPG-Mn10 before and after caesium doping	72

Figure 6.23: A comparison of the Raman spectra of IPG-Zn7.5 and IPG-Zn10 before and after caesium doping	73
Figure 6.24: Residual Difference in Raman spectra of IPG-Mn7.5, IPG-Mn10, IPG-Zn7.5 and IPGZn10, before and after caesium additions.....	73
Figure 6.25: Example of the deconvolution of the Raman spectra of an iron phosphate glass	74
Figure 6.26: Q-speciation across all base glasses	75
Figure 6.27: Mössbauer spectra of selected base samples and an example fit with the Lorentzian components	76
Figure 6.28: Mössbauer spectra of selected caesium doped and an example fit with the Lorentzian components.....	77
Figure 6.29: Quadrupole splitting against isomer shift values for selected base samples.....	78
Figure 6.30: Quadrupole splitting against isomer shift values for selected caesium doped samples.....	78
Figure 6.31: Caesium retention vs. additive concentration.....	80
Figure 6.32: Entrenched crystalline phase observed in IPG-B2.5-2Cs sample	84
Figure 6.33: SEM-EDX elemental mapping of IPG-Base-2Cs sample.....	85
Figure 6.34: SEM-EDX elemental mapping of IPG-Mn5-2Cs sample	85
Figure 6.35: Crystalline phase observed in IPG-Zn2.5-2Cs sample.....	86
Figure 7.1: XRD patterns of base glass samples.....	92
Figure 7.2: XRD patterns of NaBS-Cs2 series	92
Figure 7.3: XRD patterns of NaBS-Cs5 series	93
Figure 7.4: XRD patterns of NaBS-Cs10 series	93
Figure 7.5: DSC traces of NaBS series.....	94
Figure 7.6: First derivative of NaBS heat flow data to determine T_g	94
Figure 7.7: T_g variation with ZnO concentration.....	95
Figure 7.8: Raman Spectra of NaBS base glasses	96

Figure 7.9: Raman Spectra of NaBS-2Cs Series	96
Figure 7.10: Raman Spectra of NaBS-5Cs Series	97
Figure 7.11: Raman Spectra of NaBS-Cs10 Series	97
Figure 7.12: A comparison of the MRO region (200 – 800 cm ⁻¹) in the NaBS base glasses..	98
Figure 7.13: A comparison of the MRO region (200 – 800 cm ⁻¹) in the NaBS-Cs2 glasses ..	99
Figure 7.14: A comparison of the MRO region (200 – 800 cm ⁻¹) in the NaBS-Cs5 glasses ..	99
Figure 7.15: A comparison of the MRO region (200 – 800 cm ⁻¹) in the NaBS-Cs10 glasses	100
Figure 7.16: An example of a typical deconvolution of NaBS series glass.....	101
Figure 7.17: Q-speciation of NaBS base glasses	102
Figure 7.18: Q-speciation of NaBS-Cs2 glasses.....	102
Figure 7.19: Q-speciation of NaBS-Cs5 glasses.....	103
Figure 7.20: Q-speciation of NaBS-Cs10 glasses.....	103
Figure 7.21: Density comparison of all NaBS glasses.....	106
Figure 7.22: Caesium retention in NaBS glass series.....	107
Figure 7.23: SEM-EDX elemental mapping of NaBSZn60Ca40 sample.....	108
Figure 7.24: SEM-EDX elemental mapping of NaBSZn100Ca0Cs2 Sample.....	108
Figure 7.25: Gas phase Raman spectra for NaBS-Base glass with 2,5, and 10 wt.% Cs ₂ O additions.....	109
Figure 7.26: Gas phase Raman spectra for NaBSZn20Ca80 glass with 2,5, and 10 wt.% Cs ₂ O additions.....	110
Figure 7.27: Gas phase Raman spectra for NaBSZn40Ca60 glass with 2,5, and 10 wt.% Cs ₂ O additions.....	110
Figure 7.28: Gas phase Raman spectra for NaBSZn60Ca40 glass with 2,5, and 10 wt.% Cs ₂ O additions.....	111
Figure 7.29: Gas phase Raman spectra for NaBSZn80Ca20 glass with 5, and 10 wt.% Cs ₂ O additions.....	111

Figure 7.30: Gas phase Raman spectra for NaBSZn100Ca0 glass with 2,5, and 10 wt.% Cs ₂ O additions.....	112
Figure 7.31: Gas phase Raman spectra for glasses doped with 2 wt.% Cs ₂ O.	113
Figure 7.32: Gas phase Raman spectra for glasses doped with 5 wt.% Cs ₂ O.	113
Figure 7.33: Gas phase Raman spectra for glasses doped with 10 wt.% Cs ₂ O	114
Figure 7.34: Residual difference between the base glasses and NaBS-Cs ₂ glasses.....	116
Figure 7.35: Residual difference between the base glasses and NaBS-Cs ₅ glasses.....	116
Figure 7.36: Residual difference between the base glasses and NaBS-Cs ₁₀ glasses.....	117
Figure 7.37: The ratio of MRO structures plotted against caesium retention for the NaBS-Cs ₂ series	118
Figure 7.38: Q ₃ concentrations (top) against caesium retention values (bottom).....	119
Figure 8.1: Suggested final modifications to the off-gas analysis system.....	125
Figure 10.1: NaBSZn60Ca40Cs ₂ off-gas Raman spectra plotted in 3-dimensions to show intensity variation with time	136
Figure 10.2: Thermal analysis of Cs ₂ CO ₃	137

List of Tables

Table 3.1: Role of the Major Oxides Considered in this Thesis	6
Table 3.2: Compositions of nuclear waste glasses currently used. Adapted from [39].....	15
Table 3.3: Waste loaded glass composition used by Day et al. [65]	22
Table 4.1: Purity and supplier information for glass making reagents	28
Table 4.2: Grinding and polishing procedure for monolith samples	30
Table 4.3: Off-gas wash through procedures to accompany Figure 3.10	43
Table 5.1: Table of major Raman modes considered for borosilicate glasses.....	50
Table 5.2: Table of major Raman modes considered for iron phosphate glasses.....	51
Table 5.3: Caesium vibrational modes in solid and liquid state Raman spectroscopy	52
Table 5.4: Peaks identified in off-gas Raman trials.....	57
Table 6.1: Thermal event information for all IPG base glasses.....	66
Table 6.2: Mössbauer spectroscopy parameters for selected samples.....	79
Table 6.3: Compositional Data for IPG-Base and IPG-B Series	81
Table 6.4: Compositional Data for IPG-Mn Series	82
Table 6.5: Compositional Data for IPG-Zn Series.....	83
Table 7.1: Compositional data for NaBS base glasses	104
Table 7.2: Compositional data for NaBS-Cs2 glasses	105
Table 7.3: Compositional data for NaBS-Cs5 glasses	105
Table 7.4: Compositional data for NaBS-Cs10 glasses	106

List of Acronyms

BOs	Bridging Oxygens
CCD	Charge-coupled Device
CCIM	Cold Crucible Induction Melting
CRN	Continuous Random Network
CS	Isomer Shift
DAP	Dihydrogen Ammonium Phosphate
DOE	Department of Energy (US)
DSC	Differential Scanning Calorimetry
DTA	Differential Thermal Analysis
GDF	Geological Disposal Facility
HIP	Hot Isostatic Pressing
HLW	High Level Waste
ICP-MS	Induced Coupled Plasma - Mass Spectrometry
ICP-OES	Induced Coupled Plasma - Optical Emission Spectrometry
ICV	In Container Vitrification
ILW	Intermediate Level Waste
IPG	Iron Phosphate Glass(es)
IR	Infra-Red
LAW	Low Activity Waste
LLW	Low Level Waste

LRO	Long Range Order
MAE	Mixed Alkali Effect
MRN	Modified Random Network
MRO	Medium Range Order
NBOs	Non-bridging Oxygens
NMR	Nuclear Magnetic Resonance
PEG	Poly(ethylene glycol)
PFA	Perfluoroalkoxy alkane
QS	Quadrupole Splitting
RT	Room Temperature
SEM	Scanning Electron Microscopy
SEM-EDX	Scanning Electron Microscopy - Energy Dispersive X-Ray
SRO	Short Range Order
STA	Simultaneous Thermal Analyser
TEC	Thermoelectric Cooling/Cooler
TO	Terminal Oxygens
VLLW	Very Low Level Waste
WD	Wavelength Dispersive
XAS	X-Ray Absorption Spectroscopy
XRD	X-Ray Diffraction
XRF	X-Ray Fluorescence

1 Introduction

The first commercial nuclear reactor in the UK went online in 1956 at Calder Hall in Windscale, Cumbria. Since then the UK has accumulated a large amount of nuclear waste, with the latest radioactive waste inventory estimating a total of 4560000 m³ [1]. The waste is categorised as high level waste (HLW), intermediate level waste (ILW), low level waste (LLW) and very low level waste (VLLW) – for full details see Chapter 3.2. In the UK, the immobilisation of our nuclear waste inventory is already underway with a focus on the vitrification of HLW and cementation of some ILW/LLW. Borosilicate glass was selected as an immobilisation medium for HLW due to its acceptably high chemical durability, radiation tolerance and thermal stability [2]. These properties are important as they ensure the final wastefrom will contain the waste over the long timescales considered for nuclear waste disposal [3]. The waste glass is contained in a steel canister and is currently in interim storage awaiting relocation to a Geological Disposal Facility (GDF) where it will remain until it no longer poses a risk to humans or the environment [4]–[6].

ILW accounts for 102,000 m³ of the UK’s nuclear waste inventory and produces approximately 4.1×10^6 TBq of radioactivity [1]. There are a number of problematic contaminants that have to be considered during the treatment of ILW wastestreams. Amongst these, caesium radioisotopes are of particular concern as they account for approximately 12% of the total radioactivity in ILW and are volatile at the temperatures required for thermal treatments [7].

There are a number of immobilisation routes available for ILW, with the main two methods being vitrification and cementation [5]. Volatility is not an issue for cementation due to the low processing temperatures, however it is not an ideal wastefrom candidate for all ILW [3], [6]. Cements have poor chemical durability compared to the glass types considered in the nuclear sector, which is problematic for wastestreams with longer lived isotopes present [6]. They also incur a volume increase when considering the final wastefrom, leading to increased long term storage costs. Therefore, vitrification has been identified as a potentially more suitable immobilisation technique, offering high chemical durability and a considerable volume reduction of the final wastefrom. As previously mentioned, the issue of volatility must be addressed when considering vitrification as it is seen as one of the main challenges that must be overcome if vitrification is to be used in place of cementation for the UK’s ILW stockpile.

This work therefore focusses on the influences of caesium volatility during vitrification, and identifying methods to minimise caesium volatility. To explore these influences, a lab-scale experimental off-gas system has been developed to allow the capture and analysis of volatiles produced during vitrification. The system also incorporates a Raman spectrometer, connected to the off-gas system using fibre optic coupling and a single-pass gas flow cell. Careful interpretation of the results obtained using this system will allow for the speciation of the volatiles produced. Using this information, the glass formulation can be modified to increase the retention of volatile species.

The second chapter of this thesis will outline the project aims and objective, demonstrating how they have evolved over the course of the project.

The third chapter of this thesis briefly introduces where nuclear waste comes from, how much there is in the UK and how we categorise it. Furthermore, the immobilisation strategies employed by the UK and the long term storage plans are discussed. This section also discusses the issues surrounding vitrification and volatile elements, such as caesium. Chapter 3 also addresses the nature of glass as a material and review the literature on the two main glass types considered in this work: iron phosphate glasses and borosilicate glasses.

Chapter 4 covers the experimental methods employed to investigate the structural and chemical properties of the glasses used in this work. A standard suite of characterisation techniques were used to analyse the glasses before and after re-melting with caesium, including density measurements, Induced Coupled Plasma – Mass Spectroscopy (ICP-MS), Differential Scanning Calorimetry (DSC) and Differential Thermal Analysis (DTA), Mössbauer spectroscopy, Scanning Electron Microscopy (SEM), Scanning Electron Microscopy – Electron Dispersive X-Ray analysis (SEM-EDX), X-Ray Diffraction (XRD) and X-Ray Fluorescence spectroscopy (XRF). The use of Raman spectroscopy is also outlined here but is discussed in greater detail in Chapter 5 due to the more novel application of this technique in this work. Finally, an overview of the development of the off-gas system used for all the work reported in this thesis is given.

Chapter 5 summarises the basic theory behind Raman spectroscopy and includes a short literature survey, covering the vibrational modes of interest to this work investigated using Raman spectroscopy and literature surrounding caesium species detected using Raman spectroscopy. The commissioning process of the Raman spectrometer and a description of the initial experiments conducted are thoroughly discussed. The initial experiments aimed to identify the expected Raman spectra from known gaseous caesium species, such as caesium oxide, caesium peroxide, caesium hydroxide and caesium borate and mixed alkali borates. To aid this, a suite of caesium containing compounds were produced and held at elevated temperatures in the off-gas system described in Chapter 5. Raman spectra were collected for all these samples and used in the qualitative analysis of the caesium doped glasses discussed later in this thesis.

Chapter 6 covers the results pertaining to iron phosphate glasses (IPG). A total of 13 IPG formulations were made for this work. The compositions are based around a binary iron phosphate ($40\text{Fe}_2\text{O}_3\text{-}60\text{P}_2\text{O}_5$), with three additives; B_2O_3 , MnO and ZnO , substituted in place of Fe_2O_3 . The chapter is split into two main subsections; base glass analysis and caesium doped glass analysis. All caesium containing IPGs, were batched with a target of 2 wt.% Cs_2O . The results obtained are discussed in terms of glass composition.

The results obtained for borosilicate glasses are presented in Chapter 7. For the borosilicate glasses, a series of 6 base glasses were produced with a varying Ca:Zn ratio between 80:20 and 0:100. The composition of this series is based around the CaZn formulation currently being used at Sellafield to immobilise HLW. The final section of this chapter covers the analysis of the off-gas Raman spectra collected and speculates on the speciation of the caesium volatiles.

Finally, Chapters 8 and 9 offer further discussion of the results reported above, concluding remarks and suggestions for further work.

2 Project Objectives

The objectives set at the beginning of this project were to achieve:

- A fundamental scientific understanding of volatile evolution during melting to underpin the use of vitrification technologies in the immobilisation of ILW wastestreams.
- A mechanistic understanding of the kinetics of volatile evolution as a function of waste type, redox conditions and waste loading.
- An understanding of how melt chemistry and processing conditions can be used to maximise incorporation of volatile radionuclides in the final wasteform and minimise their emission during vitrification.

As the project progressed, the main objective that was focussed on was to further our understanding of caesium volatility behaviour during vitrification. Therefore, the objectives achieved during this project were:

- Develop a functional in-situ, real time off-gas analysis system that will further our understanding of caesium volatility.
- Investigate the effect of glass composition on caesium volatility during vitrification.

2.1 Project Methodology

The initial project plan was to study the incorporation of three volatile bearing simulant wastestreams in 3 glass systems (silicate, borosilicate, and boro-aluminosilicate). The wastestreams selected contained caesium, plutonium/PCM and technetium (or surrogates where appropriate). In-situ measurements during vitrification were a key aim of the project and the design of an in-situ system became the primary focus during the early stages of the project.

As the project progressed, an opportunity was identified to further explore the relationship between caesium volatility losses and the species of caesium vapours identified using the in-situ Raman. The results discussed in this thesis pertain to two glass systems (iron phosphate glasses and sodium borosilicate glasses), doped with caesium carbonate as a simulant volatile wastestream.

The results discussed in the iron phosphate glasses chapter were collected during the final commissioning stages of the off-gas system and therefore do not include a section analysing the in-situ Raman spectroscopy. This chapter does however fulfil the initial project aims by investigating the effect of glass chemistry on volatility.

The sodium borosilicate glass results chapter includes a section analysing the results of the in-situ Raman, covering the effect of initial caesium concentration/waste-loading on the retention rate and volatile species produced and the effect of glass composition on the retention rate and volatile species produced.

3 Literature Review

3.1 Oxide Glasses

Glasses are non-crystalline solids that display glass transformation behaviour (see Section 3.1.1). This thesis will only consider the most common glass type, oxide glasses. Oxide glasses are comprised of structural units with short range order (SRO), interactions can occur between these units, leading to medium range order (MRO) [8]. However, no long-range order (LRO) occurs due to the variation in bond lengths and bond angles between SRO structural units [9]. The role of different cations within glass can be separated into the following categories: network formers, intermediates (also known as conditional formers) and network modifiers. Network formers provide the main structure of the glass and can be form a single component glass using conventional melt-quench methods (i.e.- an easily achievable cooling rate from supercooled liquid to solid state). In this work, the main glass formers considered are B_2O_3 , SiO_2 and P_2O_5 , each of which form different base units. Borate glasses are based around trigonal BO_3 units whilst silica and phosphate glasses are based around tetrahedral units (SiO_4 and PO_4 respectively). The glass network is connected via $M - O - M$ bonds (where M is the network former ion, i.e. B, Si, P), where the oxygens connecting the two network forming ions are referred to as bridging oxygens (BOs). Non-bridging oxygens (NBOs) are therefore oxygens that are only connected to one network forming ion. Network modifiers depolymerise the glass network, creating NBOs and decreasing the T_g . In turn this affects the mechanical and structural properties of the glass. Intermediates can act as both network formers and modifiers. However, whilst intermediates can act as network formers, they are unable to form a glass in a single component system. In a similar manner to network modifiers, intermediates can act as a flux, reducing the melting temperatures required to form a glass. Table 3.1. contains some of the main oxides used in this work, categorised by their class (former, intermediate, modifier).

Table 3.1: Role of the Major Oxides Considered in this Thesis [9]

Network Formers	Intermediates	Network Modifiers
B_2O_3	Al_2O_3	Cs_2O
SiO_2	Fe_2O_3	Na_2O
P_2O_5	MnO	CaO
	ZnO	

Many of the earlier theories postulated regarding the structures found in oxide glasses could be largely split into two categories, one approach concentrates on the co-ordination numbers of the network forming ions and the second approach considers the electronegativity of the ions [10], [11]. However, there is a common agreement that some form of structure must exist that defines the properties of the material without causing periodicity. One of the most cited theories for glass formation was first proposed by Zachariasen, whose rules for glass formation are listed below. In his original paper, Zachariasen refers to a vitreous network, however his name is now synonymous with the term continuous random network (CRN), a model based around the network formation rules set out Zachariasen's paper [12]. The concept of a continuous random network identifies the similarity between a glass and its corresponding crystal structure but accounts for the lack of periodicity due to the small variations in bond lengths and angles found between the SRO units.

Zachariasen's rules for glass formation:

1. Each oxygen atom must be linked to no more than 2 cations
2. The oxygen coordination number of the network cation is small
3. Oxygen polyhedra share only corners and not edges or faces
4. At least three corners of each oxygen polyhedron must be shared in order to form a three-dimensional network.

Experiments conducted by Warren et al. were in agreement with Zachariasen's theory for a vitreous network [13], [14]. Warren et al. state that it is reasonable to suppose that even in such a non-crystalline arrangement, the interatomic distances and coordination will essentially be the same as found in the crystalline forms of silica. Each silicon atom will be tetrahedrally surrounded by four oxygens and each oxygen will be shared between two silicon atoms. The closest Si-Si distance can be perfectly defined, however the orientation of the two tetrahedra can be completely random [13]. Whilst investigating a series of sodium silicates it was observed that increasing the sodium content increased the O:Si ratio to be greater than two, meaning not all oxygen bonds would be Si-O but also a proportion of the oxygens would bond with sodium ions. This demonstrated that the idea of a random network was still applicable to a mixed oxide glass system [13]. Figure 3.1 is reproduced from Warren et al.'s paper, showing the two types of oxygen bonding presents. 'O1' oxygens are bonded to only one silicon atom, whilst 'O2' oxygens are shared between two silicon atoms [14].

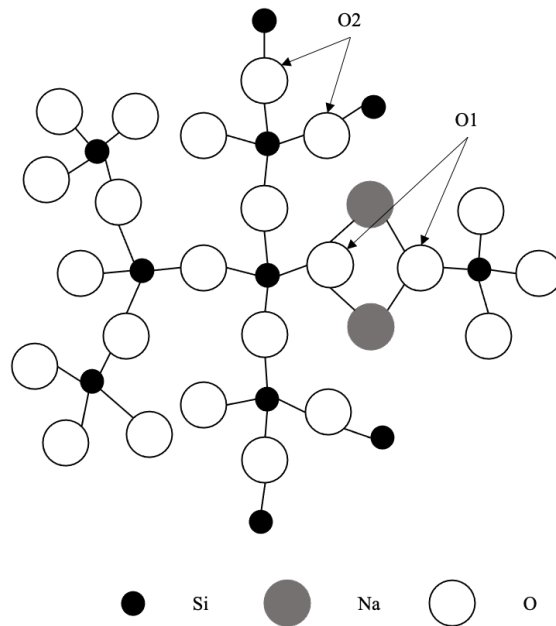


Figure 3.1: Oxygen bonding variation due to sodium content

Building on the work of Zachariasen and Warren, Greaves et al. suggested a modified random network (MRN) to incorporate network modifiers into the glass network [15]. Using data from X-Ray absorption spectroscopy (XAS) experiments, Greaves suggested that a glass network would actually consist of two components; a network former component and a network modifier component. The network former component can be described using Zachariasen's rules mentioned above. However, Greaves suggest that the network former regions are surrounded by the network modifier components, described by Greaves as percolation channels. The volume of these channels dictate some of the physical properties observed such as viscosity and melt temperature. Greaves' model suggests that the modified random network will consist of both covalent and ionic bonding [16].

3.1.1 Glass Formation and Transformation Behaviour

All glasses display glass transformation behaviour [17]. As can be seen in Figure 3.2 if a liquid is cooled below the melting point of the crystalline solid, a rapid drop in enthalpy is observed, accompanied by the formation of LRO. However, if a liquid can be cooled below T_m without crystallising, a supercooled liquid is formed [17]. As supercooled liquids do not display LRO, no rapid decrease in enthalpy is observed. Many supercooled liquids will crystallize at a temperature a little below T_m however in a glass forming liquid, as the temperature decreases, the viscosity becomes high enough to prevent atoms rearranging. At this point the structure is no longer temperature dependent and the enthalpy of the system diverges from the equilibrium line (shown as a dashed extension of the liquid line in Figure 3.2). The viscosity continues to increase, eventually locking in the structure of the supercooled liquid. The range over which this takes place is referred to as the glass transformation range. Figure 3.2 also highlights the effect of cooling rate on the final glass structure, as systems cooled at a faster rate will have less time to equilibrate during cooling and exhibit a higher final enthalpy than a glass cooled at a slower rate.

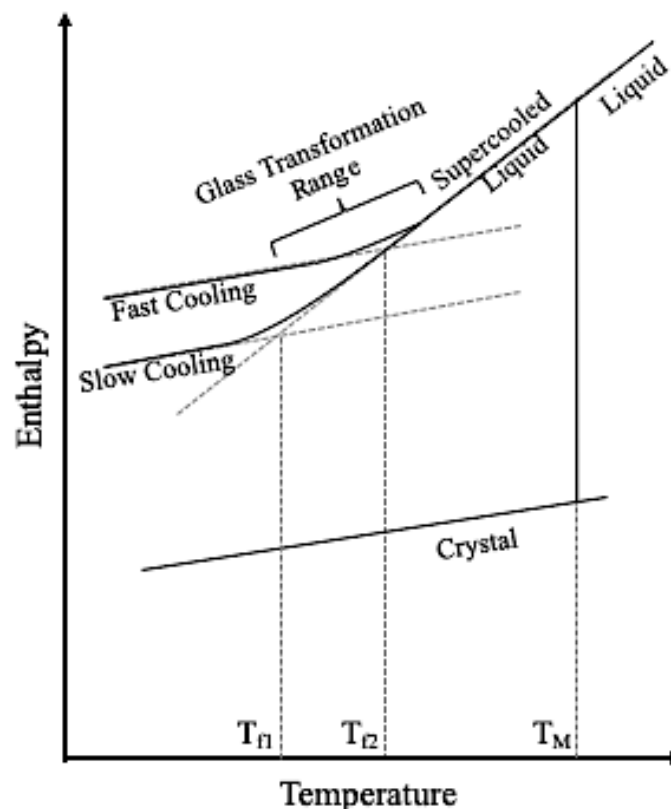


Figure 3.2: Enthalpy-Temperature diagram of glass formation

3.1.2 Effect of Alkali and Alkaline Earth Additions to Different Glass Systems

Alkali and alkali earth oxides are commonly used during glass making as fluxing agents. In silicate glasses, the addition of alkali/alkali earth dramatically decreases the viscosity of the melt, reducing the required melt temperature. As lower melt temperatures are generally desirable for practical glass production, alkali/alkali earth oxides are regularly added to both silicate and borosilicate systems. However, increasing the alkali/alkali earth content of a glass system decreases the network connectivity due to the formation of NBOs to charge balance the positively charged alkali/alkali earth ions [18], [19]. When discussing network connectivity, silicate glasses are generally classified by the number of bridging oxygens per silica tetrahedra. These units are generally referred to as Q-species, where n of Qⁿ denotes the number of BOs in the unit. Figure 3.3 shows the different Q-species that are found in silicate glasses, with an increasing number of NBOs from left to right.

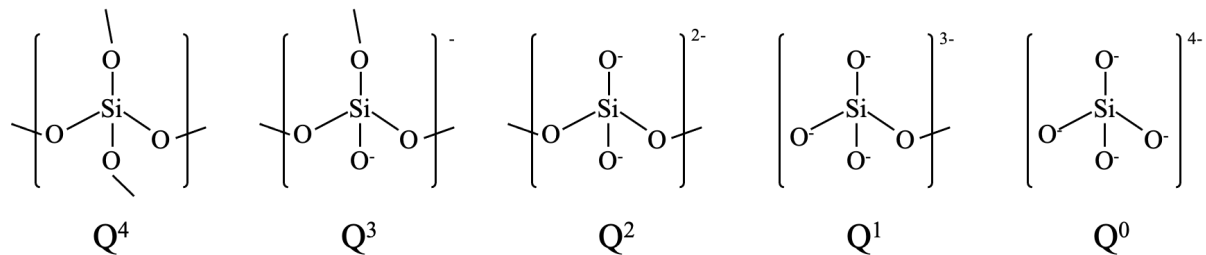


Figure 3.3: Q-speciation in silicate glasses

In borosilicate glasses, the effect of alkali and alkali earth oxide additions differs depending on the ratio of Si:B and R:B (where R is the alkali/alkali earth concentration). Dell et al. proposed a model based on increasing sodium oxide concentrations in borosilicate systems [20]. Dell et al. defined the SiO₂:B₂O₃ ratio as K and the Na₂O:B₂O₃ ratio as R. The following equations to define compositional regions where the effect of alkali additions varies:

$$R < 0.5$$

Equation 3.1

$$0.5 \leq R \leq R_{max} = \frac{1}{2} + \frac{1}{16}K$$

Equation 3.2

$$R_{max} \leq R \leq R_{D1} = \frac{1}{2} + \frac{1}{4}K$$

Equation 3.3

$$R_{D1} \leq R \leq R_{D3} = 2 + K$$

Equation 3.4

The first region is defined by Equation 3.1, where R is less than 0.5. In this region, all the alkali content is associated with four-coordinated boron units (N_4) and both units are present in equal concentrations (i.e. $-R = N_4$). This is not influenced by the amount of silica present. Equation 3.2 shows the upper and lower bounds of the second region. In this region, the additional alkali content combines with diborate groups (two BO_3 and two BO_4 units) and silica tetrahedra, forming reedmergnerite ($0.5[Na_2O-B_2O_3-8SiO_2]$). The end point for this region is when all the available silica is associated with reedmergnerite units. The third region is defined by Equation 3.3. Here, all additional sodium is absorbed by the reedmergnerite leading to the formation of NBOs on silica tetrahedra [20].

Finally, region four is defined by Equation 3.4. In this region, additional sodium oxide is shared proportionally between diborate groups and reedmergnerite. The sodium oxide that combines with diborate units leads to pyroborate units. The sodium oxide that combines with reedmergnerite also produced pyroborate units, along with Q^2 silica units [20].

When a network modifier such as an alkali oxide is added to a glass system, the effect on properties relating to ionic mobility is generally linear. However, if the total alkali content remains fixed, and the initial alkali is replaced by a second alkali source, the effect of the total alkali content on the system becomes non-linear. This effect is referred to in the literature as the mixed alkali effect (MAE), or the mixed cation effect [21], [22]. Zhong et al. investigated a series of single alkali borates of varying alkali concentrations, as well as equimolar mixed-alkali borate glasses. It was found that the mixed alkali glasses displayed lower glass transition temperatures and smaller N_4 fraction when compared to the constituent alkali borates. NMR investigations supported the theory of mixed alkali pairing, which suggested that mixed alkali pairs were less mobile and exhibited a higher electrostatic attraction to NBOs [23].

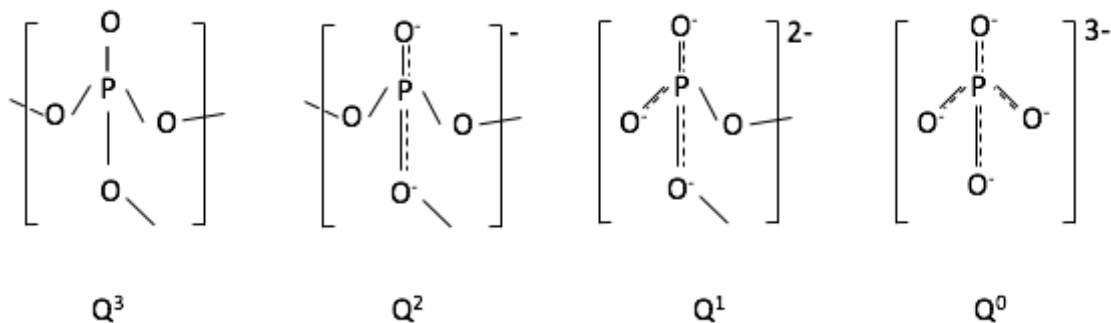


Figure 3.4: Q -speciation in phosphate glasses

Phosphate glasses are comprised of phosphate tetrahedra and their connectivity can be described using Q-species in a similar manner to that of silicate glasses. Figure 3.4 shows the Q-species found in phosphate glasses. When alkali and alkali earth oxides are added to phosphate glasses they depolymerise phosphate tetrahedra, breaking P-O-P bonds [24], [25]. However, the effect of this is not the same as that observed in silicate and borosilicate systems as the terminal oxygens (TO) found in phosphate tetrahedra also coordinate with modifier cations [24], [25]. In Q₃ tetrahedra, the NBO that associated with modifier cations is a double bonded oxygen. Q₂ tetrahedra have a double bonded oxygen and single bonded, negatively charged NBO, both of which are referred to as TO [26]. However, in both Q-species, the TO form ionic bonds with modifying cations. Hoppe suggests 3 compositional ranges exist, depending on the amount of modifier present [27].

Initial modifier additions to a vitreous P₂O₅ network begin the process of re-polymerisation, that is described by Hoppe as an increasing number of modifier cations bonding to TO, creating new Me-O-P bonds (where Me is the modifier cation), converting Q₃ units into Q₂ units in the process [27]. As the modifier content increases, the number of TO adjacent to modifier cations increases. This process continues until all TO have an adjacent modifier cation and forces the formation of highly coordinated MeO_n polyhedra.

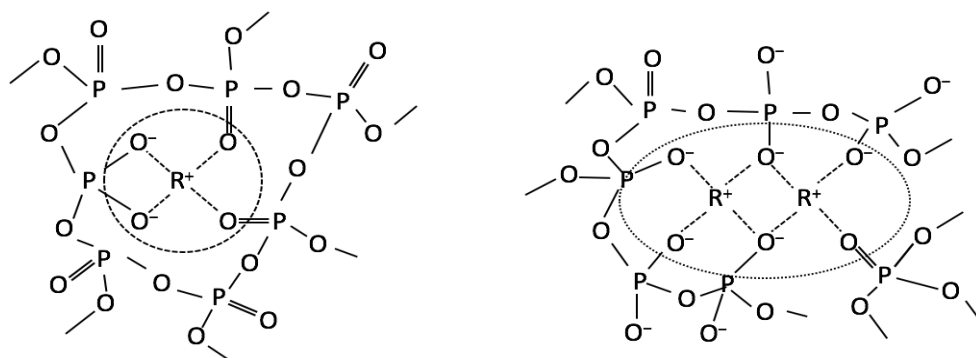


Figure 3.5: Alkali bonding in phosphate structures. Left: Coordination number of alkali ion < number of TO. Right: Coordination number of alkali ion > number of TO [28]

The second compositional range is an extension of the first range but considers the covalent bonding of the modifier cations. If the modifier cations display covalent behaviour, they can weaken the π bond of adjacent P-O bonds, stabilising Me-O-P bridges. In the first two ranges, the coordination number of the modifier cation is less than the number of associated TO as can be seen in the left hand side of Figure 3.5 (reproduced from [28]). However, in the third range, there are not enough TO available to create a stable modifier coordination environment and the MeO_n polyhedra begin to share corners and edges. In this range, the coordination number of

the modifier alkali is greater than the number of associated TO, as can be seen in the right hand side of Figure 3.5. This behaviour matches that described by Greaves' MRN for silicate systems [16].

The structure of iron phosphate glasses has been compared to the structure of various iron phosphate crystal structures. Typically for a standard $40\text{Fe}_2\text{O}_3\text{-}60\text{P}_2\text{O}_5$ composition, the FePO_4 system is considered [29]. In terms of glass structure, this translates to a combination of FeO_4 and PO_4 structures with corner sharing of the oxygens [29]. Marasinghe et al. compared the structure of IPGs to the $\text{Fe}_3(\text{P}_2\text{O}_5)_4$ crystal structure based on data from thermal analysis, however a similar logic was employed to Wright et al., implying iron oxide and phosphate structures (typically tetrahedral) with some form of corner sharing leading to Fe-O-P bonding [30]. Reis et al. describe the IPG structure as $(\text{Fe}_3\text{O}_{12})^{16-}$ clusters, interconnected through $(\text{P}_2\text{O}_7)^{4-}$ groups [31].

3.2 Nuclear Waste

Following the conclusion of World War II, several countries began nuclear programmes with the aim of developing nuclear weapons. As a result of these programmes and subsequent programmes developing nuclear power generators for civilian applications, a large stockpile of radioactive waste was produced. The majority of the UK's inventory (in terms of radioactivity) can be classified as high and intermediate level waste and is associated with fuel reprocessing activities. The exact composition of the waste varies depending on the source of the wastestream, however the main components of high level waste (HLW) are fission products, uranium, plutonium, actinides, corrosion products, fuel additives and cladding. Intermediate level waste (ILW) is mainly composed of steel, graphite, concrete, cement, sludges and ion exchange materials [32]. As a result, there has been several decades worth of research into the immobilisation and safe disposal of nuclear waste (see, for example, Ojovan and Lee [33], Corkhill and Hyatt [34]).

In the UK, waste is categorised according to its radioactivity and heat generation properties. High Level Waste (HLW) is any wastestream that produces more than 4 GBq/t of alpha activity or 12 GBq/t of beta/gamma activity, with the potential to significantly increase in temperature due to its radioactivity. Intermediate Level Waste (ILW) is classified as any wastestream that produces more than 4 GBq/t of alpha activity or 12 GBq/t of beta/gamma activity but does not produce a significant amount of heat. The remaining 2 categories are Low Level Waste (LLW); which produces less than 4 GBq/t of alpha activity and/or 12 GBq/t of beta/gamma activity and

Very Low Level Waste (VLLW); 400 kBq/t of activity [35]. As of 2019, the UK has 102,000 m³ of nuclear waste, 75% of this waste is located at the Sellafield site awaiting immobilisation and disposal. HLW accounts for 2150 m³ of waste, with 1240 m³ yet to be immobilised. The remaining 910 m³ has been vitrified using a borosilicate glass, referred to as MW, or a modified version; CaZn [1]. Over 40% of ILW waste can be accounted for by two sources, graphite (27 %) and PCM (16 %) [1]. The majority of the graphite waste is associated with Magnox and AGR reactor cores, whilst the PCM waste is associated with spent fuel reprocessing [1]. Figure 3.6 highlights the different wastestreams present in ILW waste in the UK (figures taken from 2019 Waste Inventory Report [1]).

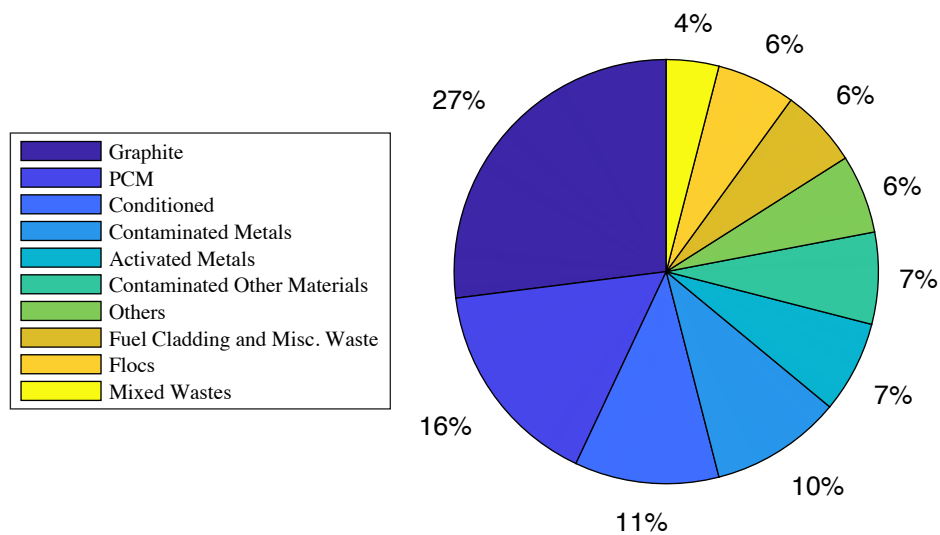


Figure 3.6: Wastestreams found in ILW waste in the UK (Data from 2019 Waste Inventory Report [1])

Nuclear Waste Glasses

The main three types of material considered for nuclear waste immobilisation are cements, ceramics and glasses [5]. For higher activity wastes, the immobilisation medium must offer high chemical durability to ensure the wastefrom remains intact for the long durations associated with radioactive decay. Additionally, the wastefrom must have high radiation damage tolerance in order to maintain the other desirable properties and maintain a safe, passive wastefrom. Finally, it is desirable to have a high waste loading, as this will lead to smaller wastefrom volumes and reduce the long-term storage costs. Considering these criteria, it becomes apparent as to why glass is such an impressive material. Whilst crystalline materials can boast higher densities, amorphization due to radiation damage can be problematic and the waste loading is limited as elements must fit within certain sites of the ceramic structure [36].

As glass is already an amorphous material, the structure is more tolerant towards radiation damage [37]. Glasses can also accommodate a higher waste loading compared to ceramics due to their high solubility limits, which given the wide range of fission products present in the reprocessing wastes is of particular importance. However, crystallisation in glasses can be problematic, as crystal formation can lead to processing issues and can negatively affect the wasteform's chemical durability [38], [39]. In comparison to cements, glasses offer superior chemical durability and produce much smaller waste packages due to the associated volume reduction. Some of the currently used compositions for HLW nuclear waste glasses can be seen in Table 3.2 below.

Table 3.2: Compositions of nuclear waste glasses currently used. Adapted from [40]

Glass	Oxide, wt%							
	SiO ₂	P ₂ O ₅	B ₂ O ₃	Al ₂ O ₃	CaO	MgO	Na ₂ O	Others
R7T7 (France)	47.2	-	14.9	4.4	4.1	-	10.6	18.8
DWPF (USA)	49.8	-	8.0	4.0	1.0	1.4	8.7	27.1
MW (UK)	47.2	-	16.9	4.8	-	5.3	8.4	17.4
CaZn (UK)	35.71	-	17.56	3.15	4.56	1.65	6.45	30.92
PAMELA (Germany, Belgium)	52.7	-	13.2	2.7	4.6	2.2	5.9	18.7
Defence HLW (Russia)	-	52.0	-	19.0	-	-	21.2	7.8
K-26 Commercial LILW (Russia)	48.2	-	7.5	2.5	15.5	-	16.1	10.2
P0798 (Japan)	46.6	-	14.2	5.0	3.0	-	10.0	20.2
GC-12/9B (China)	46.2	-	13.4	4.2	5.8	1.5	9.1	23.1

Note: Others includes a range of miscellaneous oxides reflecting the complexity of the wastestreams involved

3.3 Sodium Borosilicate Glasses

Borosilicate glasses are used for the treatment HLW in a number of countries including UK, US, France, Belgium, Germany, India. Their high chemical durability and flexible waste loading has seen them employed for a variety of waste streams, whilst the volume reduction associated with vitrified waste makes vitrification a cost-effective treatment when considering long term storage [3], [4], [6], [33]. Most countries using vitrification for the treatment of HLW

have opted for glasses with a borosilicate composition. To improve processing efficiency, alkali oxides are also included in the composition, such as Na_2O , Li_2O [39]. Network intermediates such as Al_2O_3 and Fe_2O_3 may also be used, as these can improve mechanical stability and improve processing efficiency [41].

The decision to use borosilicate glasses as an immobilisation medium was made by UK, US and France in the 1970s/1980s. The US decision was based on reports from the US Department of Energy (DOE) and the commercial simplicity and cost in comparison to other options researched up to that time. The UK, French and US (Savannah River) base glass compositions are known as MW, R7T7 and DWPF respectively. Their compositions can be found in Table 3.2. The MW composition developed by the UK is a simple SiO_2 - B_2O_3 - Na_2O - Li_2O system. MW originated from a sodium borosilicate, but after it was found that a mixed alkali system required a lower total alkali content, lithium was substituted into the formulation in an equimolar amount to sodium [42]. The boron content was also investigated due to the relationship between boron content and molybdenum solubility [42]. High boron content formulations showed better molybdenum solubility and lower processing temperatures, however formulations with a high B:Si ratio exhibited poor leachability when wastes from reprocessing fuels from UK magnox reactors were incorporated [42]. Therefore, the boron concentration was optimised to maximise waste solubility whilst maintaining a satisfactory chemical durability [42]. The R7T7 and DWPF compositions were developed in a similar manner, looking at sodium borosilicate systems and modifying the formulation to meet the waste loading requirements and processing criteria [43].

Over the course of several decades, borosilicates have been studied and modified to incorporate as many problematic waste streams as possible, whilst retaining essential properties such as chemical durability [44]–[50]. In a similar timeframe, there has also been a significant amount of work done on the fundamental structures of glass, with the emergence of new theories to explain observations such as the mixed MAE and the existence of MRO in glass networks. MRO could be an important concept to further understand for waste vitrification as it has been suggested that boron could influence caesium volatility [8], [21], [51], [52].

The structures found within borosilicates have been investigated by various research groups, primarily those interesting in the use of borosilicates for nuclear waste treatment. A number of methods have been used, including Raman spectroscopy and Nuclear Magnetic Resonance (NMR) Spectroscopy. Using ^{11}B NMR, Parkinson et al. confirmed the existence of MRO in borosilicate glasses, comparing the superstructures responsible for MRO to the crystalline

mineral structures danburite and reedmergnerite, a theory suggested by Dell years earlier [8], [20]. Parkinson et al. found that with increasing network modifier content, the trigonal planar three co-ordinated BO_3 units were converted to tetrahedral 4 coordinated BO_4 and then at higher modifier contents back to BO_3 units increasing the number of NBOs in the system, as was seen in the alkali borate system [14]. Parkinson also noted that introducing intermediate trivalent oxides into the network removed the modifier oxide from the borate sites, in order to charge compensate the intermediate oxide ions resulting in less BO_4 units. In agreement with Parkinson et al., Vegiri et al. found that the addition of modifier oxides into the glass network causes neutral BO_3 units to change to BO_4^- units [53]. Vegiri also reported that the NBO containing triangular units, BO_3 , are favoured at high temperatures at the expense of BO_4^- tetrahedral units. Furthermore, both Parkinson et al. and Vegiri et al. reported that increasing the alkali content leads to a change in the alkali ion behaviour, with an increased association with silicate Q^n species rather than the borate groups. Thus at low concentrations, caesium ions increased network connectivity by charge balancing the formation of BO_4 units. However, with increasing concentrations, the caesium ions were found to migrate to sites with NBOs leading to increased depolymerisation of the glass network [53].

Parkinson et al. conducted a series of mass loss experiments that showed additions of aluminium (0.95 mol%) or lanthanum (1.68 mol%) to the MW composition increased caesium volatility by approximately 20 % in comparison to magnesium additions to MW [54]. Parkinson et al heated approximately 0.2 g of sample to 1000 °C at 10 °C/min, held the samples at this temperature and then cooled them back to RT at 10 °C/min. Parkinson et al. suggest that the increased volatility when Al and La were added could be due to the increased number of danburite like structures. Parkinson also suggests a relationship between Q_3 concentrations and volatility, with caesium volatility increasing with increasing Q_3 concentrations [54]. Work conducted by Banerjee et al. studied the change in BO_4^- units and BO_3 units when introducing additives to a borosilicate composition ($45\text{SiO}_2-30\text{B}_2\text{O}_3-17.5\text{Na}_2\text{O}-0.25\text{Cs}_2\text{O}-5\text{XO}$, where $\text{XO} = \text{B}_2\text{O}_3, \text{BaO}, \text{CaO}$ or ZnO). Within this study it was found that ZnO additions promoted caesium retention [55]. The increased retention was attributed to the formation of ZnO_4^{2-} units interacting with Cs^+ ions as shown in Figure 3.7. In the respective NMR traces, the glass with ZnO showed a decrease in the BO_3 peak intensity whilst the BO_4^- peak showed an increase in intensity. Studies conducted on borosilicate glasses not containing ZnO by Vegiri et al. and

Parkinson et al. showed that BO_4^- units are less effective at retaining caesium ions compared to trigonal NBO containing BO_3 units [8], [53], [55].

The development of different compositions has been dictated by the intended processing technology. Kim et al. developed a series of glass compositions intended for immobilising low activity waste (LAW) using In Container Vitrification (ICV) [45]. Several properties are considered important when developing a glass for ICV, including viscosity (as is the case with most vitrification methods) and electrical conductivity. Similarly, Luckscheiter and Nesovic

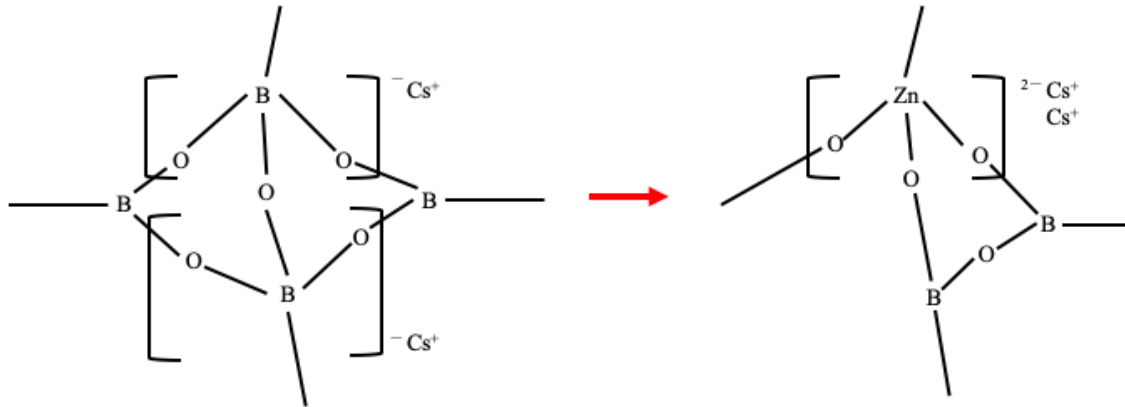


Figure 3.7: ZnO addition to a borosilicate network [42]

also identified electrical conductivity as an important property [46]. In an effort to maximise the conductivity whilst maintaining a workable viscosity, Luckscheiter and Nesovic studied glass compositions with varying ratios of alkali ions with the intention of optimising the electrical conductivity without compromising the viscosity of the melt [46]. Electrical conductivity is a key property in the ICV process as it utilises direct Joule heating. Due to the batch sizes used in ICV on a commercial scale, the glasses were tested for crystallinity by quenching and slow cooling each sample. This was to ensure the glass would not crystallise at the slow cooling rates experienced at the centre of large vitreous wastefoms used on a commercial scale. Both studies proposed similar glass compositions, with proposed melting temperatures between 1100-1400°C. Viscosity also needs to be considered for most processes to allow the glass to be poured or fed through the melt system.

In an effort to improve technetium-99 retention in American LAW glass, Jin et al. investigated the effect of sulphate in the glass composition. Rhenium was used as a surrogate for technetium. The authors produced two glasses, a modified sodium borosilicate with 0.6wt% SO_3 and a second composition with the sulphate removed. The results showed that with the removal of sulphate the rhenium retention nearly doubled with an increased retention from 32% to 63%. This result is not necessarily surprising, as it simply implies that the presence of a second

volatile component has an effect on the volatility of the first. Jin et al. note that whilst the removal of sulphate from the melts led to a significant increase in retention, it would not be applied to current operations as the removal of sulphates would not be practical [56]. However it does suggest that minimising other volatile components will be important in promoting retention of volatile radionuclides.

3.3.1 Caesium volatilisation from borate and borosilicate melts

Extensive research has been conducted investigating the relationship between glass composition, temperature and the volatility of caesium from glass melts. The literature generally agrees that there is a clear relationship between volatility and temperature, as can be seen in Figure 3.8 (reproduced from [5]).

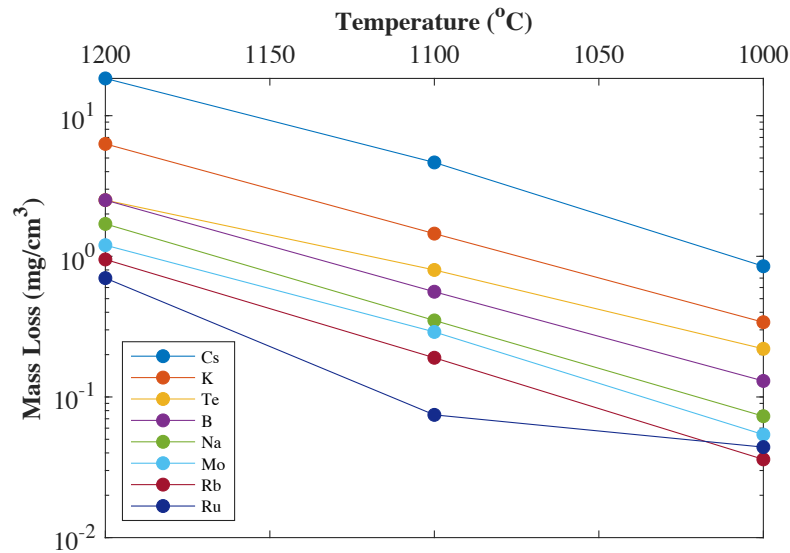


Figure 3.8: Mass loss behaviour of various volatiles at several temperatures.

Banerjee et al. reiterates the relationship between diffusion and temperature, using Equation 3.5 below to explain the caesium volatility losses found when different oxides were added to a borosilicate system [55].

$$D = D_0 \cdot \exp(-E/RT)$$

Equation 3.5

where D is the diffusion rate, D₀ is the pre-exponential term, E the activation energy, R the universal gas constant and T is temperature in K. Using this equation, Banerjee calculated diffusion rates for a series of glasses, shown in Figure 3.8. Banerjee suggested a relationship between the pre-exponential term and the caesium volatility, stating that the initial diffusion rate is the controlling factor for volatility.

Most of the literature regarding the speciation of caesium vapours has employed mass spectroscopy to identify the different species. At temperatures relevant to the work conducted in this thesis (below 1100 °C), the literature agrees that the primary volatile produced from caesium containing borosilicate glass systems is a caesium borate monomer (CsBO_2), above 1350 K, B_2O_3 vapours have also been observed [57]–[61]. The presence of caesium borate dimers and mixed alkali borate species have also been observed, however these tend to be present in far smaller concentrations than the monomer units [57]–[61]. Early work by Asano and Yasue determined that the vapour speciation above a series of sodium borosilicate glass melts in the temperature range of 915 – 1172 K, were in good agreement with the vapour speciation above NaBO_2 melts at similar temperatures [62]. Asano and Yasue observed NaBO_2 and $\text{Na}_2(\text{BO}_2)_2$ vapours over all compositions, but only observed the formation of elemental sodium over a composition where the molar concentration of Na_2O exceeded the molar concentration of B_2O_3 [62]. Further work by Asano and Yasue identified similar behaviours in caesium containing sodium borosilicate glasses, reiterating the primary volatiles to be observed being alkali metaborates, including a mixed alkali borate, $\text{NaCs}(\text{BO}_2)_2$ [57], [58]. However in these studies, no gaseous Cs was observed, which Asano and Yasue suggested was likely due to the dissociation behaviour of the two alkali borate structures, with the dissociation energy between Na and BO_2 being much lower than that of Cs and BO_2 [57], [58]. All work conducted by Asano and Yasue concluded that the main vapour species observed were alkali metaborates, with only minor amounts of diborate species observed [57], [58], [62], [63]. Similar work was also conducted by Stolyarova et al., which reaffirmed the results of Asano and Yasue, reaching the same conclusion that CsBO_2 the primary caesium volatile observed over caesium borosilicate glass melts [59], [61]. Stolyarova et al. also observed B_2O_3 vapours at temperatures above 1350 K [61]

3.4 Iron Phosphate Glasses

The term iron phosphate glasses or IPGs should in its strictest sense be used to describe glass systems containing only Fe_2O_3 and P_2O_5 . However, its use in the literature has become more of an umbrella term, often used to describe systems based around a typical iron phosphate, but that also contain multiple oxides over a range of concentrations. When considering the use of the term IPG in this section of work, it was decided that the term be used in accordance with the reference material, even in instances where the term may have been applied to a glass system that may not strictly be considered an iron phosphate.

Phosphate based glasses have been considered for nuclear waste immobilisation by a number of countries including Russia, Belgium, Germany and USA. The US were the first country to begin researching the use of phosphates for waste immobilisation [64]. However, they were quickly discouraged by the processing challenges of working with phosphate melts [65]. Similarly, Germany and Belgium both opted not to use phosphate glasses after unconvincing trials. The corrosion of the melt system was deemed to outweigh the benefits of phosphate systems. Russia is the only country to have used phosphate based glass on a large scale, using an aluminophosphate composition with a melt temperature of approximately 1000 °C [40], [64]. Despite negative preliminary studies, the idea of using phosphates is still being evaluated by a number of countries for specific wastestreams that are poorly suited to borosilicate systems. To safely vitrify these wastestreams in borosilicates, the waste would need pre-treatment to remove or separate the problematic species, or the waste content would need to be diluted to a point where all the waste was soluble [66]. For example, many of the problematic wastestreams at Hanford site in the US contain high levels of phosphates, sulphates, iron and sodium along with a high heavy metal content. Whilst poorly suited to borosilicates, these wastestreams are potentially well suited to iron phosphates as they have a much higher solubility limit for sodium.

Kim et al. suggested that the solubility of SO_3 in iron phosphate glass is considerably higher in iron phosphates compared to borosilicates, reporting a retention of approximately 45% of the initial 2.9wt% of the SO_3 batched. Kim et al. concluded that the SO_3 content in LAW would not be the limiting factor when determining the waste loading of the final waste packages for LAW in iron phosphate systems [67]. However, further work by Bingham et al. found that over a range of compositions the retention of SO_3 in iron phosphates did not exceed 1% [68]. Most recently, Day et al. presented more promising results, incorporating approximately 3.7wt% of SO_3 into the glass structure, representing a retention ratio of 85% [66]. Whilst these results

may appear to be conflicting, it is worth noting that each study used a different base glass composition and therefore these results may highlight the importance of composition on volatile retention in iron phosphate glass systems.

Table 3.3: Waste loaded glass composition used by Day et al. [66]

Oxide	Target wt.%	Oxide	Target wt.%
Al ₂ O ₃	13.21	Re ₂ O ₇	0.03
B ₂ O ₃	0.03	SiO ₂	5.58
Cl	0.04	SO ₃	4.37
Cr ₂ O ₃	2.7	Bi ₂ O ₃	1.77
Cs ₂ O	0.13	CaO	1.06
F	0.16	Fe ₂ O ₃	7.1
K ₂ O	0.78	La ₂ O ₃	0.71
Na ₂ O	20.03	ZnO	3.55
P ₂ O ₅	38.06	ZrO ₂	0.71

Day et al. investigated the retention of caesium and other volatiles in a sodium iron phosphate system (composition shown in Table 3.3), during different melting conditions and acquired some promising results. When melted at 1050 °C for 4 hours in a small crucible scale test (~300-500g) the caesium retention was reported to be 100% (based on the average ICP-AES measurements of 6 small scale test samples). However, it is possibly more impressive that the caesium retention was still 92% when the test was scaled up to an 80 kg melt with a 48 hour duration [66]. The retention rates of SO₃ and rhenium (used as a technetium surrogate) were also analysed. The SO₃ retention ranged from 98 % in the small-scale trials to 65 % in the 80 kg melts. Intriguingly, the fractional retention of rhenium remained constant regardless of melt size and duration, with both trials resulting in a 67 % retention rate.

Whilst investigating the possibility of iron phosphate glass as an immobilisation medium for CsCl and SrF₂, Mesko et al. evaluated the caesium retention using atomic absorption. They found that for caesium contents as high as 17.5 mol%, almost all of the caesium could be retained within the glass. The melt temperatures used in these experiments ranged from 1000-1200 °C, although the paper suggests that the melting temperatures could be as low as 950 °C when Cs and Sr were added as halides as opposed to oxides [69]. Mesko et al. suggest the waste

loadings of Cs_2O and SrO in iron phosphate glasses could be as high as 30 mol% and 46 mol% respectively [69], and found that when caesium was added to a series of IPGs as CsCl , the analysed caesium content for all glasses was ± 0.3 at.% of the target content [69]. This result is particularly interesting because as suggested above, caesium volatility might be influenced by the release of other volatile elements due to an entrainment effect as noted by Jin et al. with rhenium and sulphate species [56]. However, the Mesko et al. suggest that the low volatility of caesium in their study might be explained by the increased fluidity of the melt, allowing for shorter melting times and lower melt temperatures [69].

Whilst looking at the separation and treatment of caesium and strontium, Aloy et al. found after separating caesium, strontium and transplutonic elements from a larger volume of HLW, the resulting concentrates could be vitrified into aluminophosphate glass [70]. Aloy et al. found that with a 30-50 % waste loading (Cs_2O), only 0.6 % of the total caesium content was volatilised from the glass melt. The authors do not state how the caesium losses were measured or clarify if the waste load percentage and loss percentage are mol% or wt%, however the results do agree with Day et al., showing phosphate based glasses to be a promising candidate for immobilising highly volatile radionuclides [66], [70].

The inclusion of iron and phosphates in the above wastestreams reduces the amount of glass forming components needed to form a stable glass product, increasing the overall waste loading and reducing cost. Although in general, phosphate based glasses are considered to have poor chemical durability, a variety of studies have shown binary and ternary iron phosphates to have chemical durability comparable to borosilicate compositions currently used for HLW immobilisation [71]–[73]. Iron phosphates have been proven to have better chemical durability in comparison to other phosphate based glasses and it is suspected that this is due to the formation of Fe-O-P bonds in place of P-O-P bonds [73],[74]. Karabulut et al. note that the chemical durability is mainly influenced by the total iron content, with the ratio of Fe^{2+} : Fe^{3+} having no effect on the durability [75]. Research into the use of iron phosphates has shown that regardless of starting conditions, iron will exist as both Fe^{2+} and Fe^{3+} within the glass structure [67], [73], [76]–[78]. Several Mössbauer studies have investigated the coordination environment of both Fe^{2+} and Fe^{3+} and have found that Fe^{3+} is present in both tetrahedral and octahedral environments, with evidence that some of the octahedral sites maybe distorted [67], [77]. Fe^{2+} was only found in octahedral coordination environments. Investigating the distribution of Fe^{3+} between the tetrahedral and octahedral sites, Yu et al. found that for a

system where 80% of the iron was present as Fe^{3+} , 69% was in tetrahedral coordination environments and 11% in octahedral environments [77].

Both Kim et al. and Day et al. investigated the use of iron phosphates to immobilise the problematic wastestreams stored at the Hanford site (WA, USA) and both research groups proposed the use of cold crucible induction melting (CCIM) to negate concerns regarding the corrosion of the melt systems [66], [79]. Interestingly, when the Fe^{2+} content of two glasses of the same composition were compared, the glass produced using CCIM contained more Fe^{2+} compared to glass produced in a conventional electric furnace. The glass produced using CCIM contained 56% Fe^{2+} compared to only 11% Fe^{2+} in glass produced in a conventional electric furnace [79]. The authors propose that this could be due to the use of carbonates in the starting batch or due to the SiC used as a conductive material to initiate the melt. In a study by Yu et al. it was found that the starting reagents have a more significant effect on the final glass structure in comparison to borosilicates [77]. This is due to the redox states within iron phosphate melts and the evolution of by-products, such as gaseous ammonia when ammonium phosphate is used as a reagent. As the ammonia creates a reducing atmosphere, glasses made using ammonium phosphate contained more Fe^{2+} when compared to glasses made using P_2O_5 as a reagent [77]. When producing a series of sodium iron phosphates (compositions in the range $4.6\text{Na}_2\text{O}-17.7\text{Fe}_2\text{O}_3-77.7\text{P}_2\text{O}_5$ to $10.6\text{Na}_2\text{O}-34.9\text{Fe}_2\text{O}_3-54.5\text{P}_2\text{O}_5$), despite both glasses being produced using the same melting and annealing programme, the glass produced from P_2O_5 only contained 9% Fe^{2+} . In contrast the glass produced from ammonium phosphate contained 54% Fe^{2+} [77]. Glass melts conducted at higher melting temperatures create a more reducing atmosphere. This leads to a higher Fe^{2+} fraction at the expense of Fe^{3+} in octahedral coordination, however the Fe^{2+} does not replace Fe^{3+} in the tetrahedral environments [78]. In a separate study it was found that the increased in Fe^{2+} lead to increased levels of crystallisation [76].

The concentration of bridging oxygens does not change significantly with Fe^{2+} concentration indicating that Fe(II)-O-P and Fe(III)-O-P type bonds are equally important in glass structure [75]. Looking at the P-O-P:P-O- (BO:NBO) ratio in a series of iron phosphates with increasing iron content, it was found that the number of bridging oxygens was inversely proportional to the iron content. The increased iron content also had a similar relationship with the ratio of $\text{Fe}^{2+}:\text{Fe}^{3+}$. The author suggests this is due to the formation of the more stable Fe-O-P bonds [77]. Yu et al. proposed a structural model based on their results suggesting that the structure can be interpreted as tetrahedral PO_4 units joined at two corners as P-O-P bonds

to form chains. Within the chains, cross links are formed via PO₄ units, or iron oxide units. Iron groups cause depolymerisation within the P–O–P network, with the depolymerisation increasing as a function of iron content. This eventually leads to the formation of P₂O₇ groups. Yu et al. found this model to be consistent with their experimental results. Marasinghe et al. suggest that Q¹, Q² and Q³ species can all be found in a typical phosphate structure, with Q¹ species present as (P₂O₇)⁴⁻ dimers and Q² and Q³ forming longer –P–O–P– chains [80]. When iron is added into the glass network it can be present in a number of coordination environments and oxidation states. As previously discussed, structural studies have identified Fe³⁺ to be present in tetrahedral, octahedral and distorted octahedral coordination, whilst the coordination of Fe²⁺ is observed to be distorted octahedral or trigonal prismatic [73], [81]. Marasinghe et al. suggest that the distorted octahedral coordination is actually trigonally coordinated Fe²⁺ folded around the y-axis [80]. Wright et al. suggest that Fe²⁺ is present as either trigonal prismatic or distorted octahedral coordination but do not infer that the two coordinations could be linked [81]. Wright et al. conclude that the structure is “nanoheterogenous with FePO₄⁻ like regions of alternating FeO⁴⁻ and PO⁴⁺ corner sharing tetrahedra, and those having a more typical phosphate chain structure incorporating 6-fold co-ordinated Fe²⁺/Fe³⁺ network modifying cations.” [81].

The poor thermal stability of iron phosphates is one of the main issues that needs to be addressed if iron phosphates are to be considered as an immobilisation medium for nuclear waste. The thermal stability of a glass dictates its tendency to devitrify or crystallise upon cooling [82]. Glasses with high thermal stability are less likely to devitrify/crystallise when exposed to slow cooling regimes compared to glasses with poor thermal stability. Hruby et al. developed an empirical model to define thermal stability in glasses, based on the thermal events observed during thermal analysis [83]. Equation 3.6 below shows the Hruby coefficient, which can be used to assess thermal stability.

$$K_{gl} = \frac{T_r - T_g}{T_m - T_r}$$

Equation 3.6

Where T_g is the glass transition temperature, T_r is the onset of crystallisation and T_m is the onset of melting. Simpler assessments can be made that focus on the temperature difference between the glass transition temperature and the crystallisation temperatures, as seen in Li et al. [84]. The thermal stability of glasses in the thesis will be assessed using Hruby et al.’s method as seen in later sections (see Section 6.3, Table 6.1) [83].

In an effort to improve the thermal stability, several studies investigated the effect of B_2O_3 doping. Bingham et al. found that whilst adding B_2O_3 in a pro rata manner to a binary $40Fe_2O_3$ - $60P_2O_5$ iron phosphate glasses led to increased thermal stability (in comparison to the $40Fe_2O_3$ - $60P_2O_5$ base glass) [85]. Karabulut et al. found that pro-rata additions of B_2O_3 led to a decrease in thermal stability, however direct substitution of B_2O_3 for Fe_2O_3 suppressed the crystallisation of the glass product whilst having no significant effect on the chemical durability [72]. Karabulut et al. suggest that the addition of B_2O_3 leads to a decrease in the Fe^{2+} content, which as previously mentioned would explain the improved properties [72]. Donald et al. studied the effect of B_2O_3 on the thermal stability of sodium-aluminophosphates and found the doped glasses had better thermal stability, this effect was not seen when the base glass was doped with B_2O_3 and Fe_2O_3 [86]. The effect of several other dopants have also been investigated, including MoO_3 , SrO and UO_2 which all showed signs of improved thermal stability and a suppression of the tendency to crystallise [85], [87]. It is thought that additives such as molybdenum and uranium promote the oxidation of the iron to Fe^{3+} , and as previously discussed glasses with a higher Fe^{3+} content are considered more resistant to crystallisation [76], [88].

3.5 Concluding Remarks

The UK has a significant amount of high activity waste that requires immobilisation. Thermal treatment is a promising treatment route for some ILWs, however caesium volatilisation is of particular concern during such processing hence the issues surrounding thermal treatment and caesium volatility have been addressed. This literature survey has predominantly covered two glass types; sodium borosilicates and iron phosphate glasses, covering their structure, structural changes due to additive addition and caesium retention. From the literature, various influences on caesium volatility have been identified, including; additive concentration, melt conditions, and structural changes. Furthermore, the caesium bearing species expected to volatilise during vitrification have been identified.

Sodium borosilicate glasses remain an obvious candidate for nuclear waste immobilisation. However, there are several components present in ILW wastestreams that exhibit poor solubility in borosilicate systems. If borosilicate systems are to be employed for the treatment of ILW wastestreams, this must be addressed – most likely by modification of the glass composition.

Iron phosphate glasses have been reported to incorporate significant quantities of volatile components such as caesium with minimal volatile losses, along with much more desirable solubility levels of other ILW components. However, several properties must be improved, or better understood if IPGs are to be considered as a viable processing option of the UK's ILW stockpile. Of particular interest for this work is the effect of the iron oxidation state and compositional changes on volatility.

Of particular interest to this work, the retention of volatile species both glass types seems to be sensitive to the glass composition, a relationship that will be explored in later sections of this thesis.

4 Experimental Methods

4.1 Base Glass Preparation

For the iron phosphate and borosilicate glasses discussed in Chapters 6 and 7 respectively, the reagents listed in Table 4.1 were weighed out to the appropriate amounts using an electronic balance with an accuracy of ± 0.01 g. The reagents were mechanically mixed to homogenise the batch and stored under dry conditions prior to melting.

Table 4.1: Purity and supplier information for glass making reagents

Reagent	Purity	Supplier
Iron Oxide, Fe_2O_3	>98%	Alfa Aesar
Dihydrogen Ammonium Phosphate, $\text{NH}_4\text{H}_2\text{PO}_4$	>98%	Alfa Aesar
Boric Acid, H_3BO_3	>99.5%	Sigma Aldrich
Manganese Carbonate, MnCO_3	>99.9%	Alfa Aesar
Zinc Oxide, ZnO	>99%	Fisher Scientific
Calcium Carbonate, CaCO_3	>99.3%	Glassworks Services
Sodium Carbonate, Na_2CO_3	>99.1%	Glassworks Services
Silica, SiO_2	>99.5%	Glassworks Services
Caesium Carbonate, Cs_2CO_3	>99.5%	Acros Organics

For the sodium borosilicate glasses discussed in Chapter 6, a 220 mL zirconium stabilised platinum crucible was used for the base glass melts. For the iron phosphates discussed in Chapter 6, mullite crucibles were used as the large amount of ammonia produced and the aggressive melt nature of phosphate based glasses caused concerns surrounding crucible corrosion. Where mullite crucibles (approx. 330 mL) were used, crucibles were heated to within 100 °C of the melting temperature to avoid thermal shock, prior to any batch being added. All caesium free glasses discussed in Chapter 6 and Chapter 6 were melted at 1150 °C in air. Base glasses were produced in batch sizes between 150 – 300 g. The batch was transferred to the appropriate crucible in stages due to the volume limitations of the crucibles. After all batch was transferred, melts were given 1 hour batch free time before stirring was introduced for the final 2 hours. All melts were cast into a pre-heated steel mould and immediately transferred to an annealing furnace. The iron phosphates were annealed at 450 °C (as per Bingham et al. [89]) whilst the sodium borosilicate were annealed at 540 °C (as per Fisher et al. [90]). The samples were held at their annealing temperatures for 1 hour then

cooled to room temperature at a rate of 1 °C / min. Upon removal from the annealing furnace, samples were prepared for characterisation tests and caesium doped melts as described below.

4.2 Caesium Doped Glass Melts

The base glasses and caesium carbonate were dried at 120 °C for a minimum of 12 hours prior to weighing (See Appendix 11.3 for TGA data of Cs₂CO₃). Glasses were batched with the appropriate amount of caesium carbonate to achieve the correct Cs₂O wt% in the target composition. The glass and caesium carbonate were mixed, placed in a mullite crucible and then sealed into the modified HIP canister described in Section 4.12. The HIP canister was then placed into the furnace and connected to the other components of the off-gas system. The furnace was programmed to ramp to the required temperature at a rate of 5 °C min⁻¹ and dwell at temperature for 3 hours before the entire furnace system was allowed to cool naturally to RT. Once cool, the steel canister was cut open and the caesium doped glass retrieved for analysis. The canister, along with all other off-gas components was washed through with 10% HNO₃ and the resulting solution analysed to determine the caesium concentration following the procedure stated in Section 4.6.

4.3 Analytical Sample Preparation

4.3.1 As-Cast Monolith Samples

Two types of monolith samples were considered in this work, as-cast and epoxy mounted sections. A 38 mm diameter disk was poured from every base glass melt and annealed following the programme stated above.

Epoxy mounted sections were produced from caesium doped melts by sectioning the doped glass from within a mullite crucible using a Struers Secotom-50 high speed saw equipped with a diamond edged cutting disk. These sections ranged from approximately 1 cm² to 9 cm² with this area depending on the extend of the cracking of the sample.

All monolith samples were ground flat and polished following the procedure stated in Table 4.2, using a Buehler Automet-250 grinder-polisher. Samples were ground flat using diamond grinding disks or the equivalent particle size silicon carbide grinding pad. Samples were then polished using 3 and 1 μm diamond suspension fluid on Plano and cashmere polishing pads respectively. The surface finish of each sample was qualitatively inspected using an optical microscope.

4.3.2 Powder Samples

Powder samples were made from all compositions by removing a small section from the glass monolith and crushing it using a hardened steel impact pestle and mortar. The resulting powder was passed through a 75 μm aperture sieve to create approximately 3 g of powder.

Table 4.2: Grinding and polishing procedure for monolith samples

Disk Type	Particle Size (μm)	Applied Force (N)	Time (minute s)	Platen Speed (rpm)	Head Speed (rpm)
Diamond Grinding Disk	30	5	5	120	61
Diamond Grinding Disk	15	5	5	120	61
Diamond Grinding Disk	9	5	5	120	61
Plano Polishing Cloth	3	5	10	120	50
Cashmere Polishing Cloth	1	5	10	120	50

4.3.3 Pellets

Pressed pellets were produced of the iron phosphate compositions for Mössbauer spectroscopy. These samples were produced from powdered material and poly(ethylene glycol) (PEG), pressed in a 13 mm die with a 1 tonne uniaxial applied force. The required sample to PEG ratio was calculated using Demeter software to optimise the iron content of the sample, typically this ratio was in the range 1:4 (25 mg sample, 100 mg PEG) [91].

4.3.4 Off-gas Solutions

To determine the caesium concentrations found in the off-gas system described in Chapter 4, ICP-MS analysis was conducted on acid wash throughs of the off-gas line, along with the contents of the gas washing bottles. 10 % nitric acid (VWR) was used for the off-gas line wash through. Due to the adhesive nature of some caesium species (such as caesium borates), it was necessary to boil components of the off-gas system in acid to ensure that as much caesium was reclaimed as possible.

4.4 Density Measurements

The density of all samples was measured using monolith samples in a Mettler Toledo MS-DNY-43 Archimedes balance. UHQ water was used as an immersion medium and all readings were taken in triplicate. The results reported in the later chapters of this thesis are the average of these readings.

4.5 X-Ray Diffraction

4.5.1 Bruker D2 Phaser

A Bruker D2 Phaser X-ray Diffractometer, operating at 30 kV and 10 mA was used to obtain XRD patterns for all samples. XRD analysis was conducted using Cu- $K\alpha$ radiation, over a 2θ range of 10 - 70 ° with 0.02 ° step size and a step time of 1 s. For the iron phosphate samples, the diffractometer discriminator settings were modified to account for the high levels of fluorescence observed with high iron content. The lower discriminator setting was 0.19 and the upper setting was 0.27. For all other samples, the discriminator settings were left at their standard limits of 0.11 – 0.25.

4.5.2 Panalytical XPert3

The caesium doped iron phosphate samples were also analysed using a Panalytical XPert3 as phase identification using the traces from the Bruker D2 diffractometer proved unsuccessful. Samples were scanned over a 2θ range of 10 - 70 ° in 0.026 ° increments and with a step time of 1.6 s.

4.5.3 Phase Identification

Where crystalline phases were detected, they were identified using the ICDD PDF4+ database, accessed through the University of Sheffield's MSE licence through the SIEVE+ 2020 software

package. A background removal tool was used on all traces, The $K\alpha_2$ contribution was not removed and peaks were manually attributed to the traces.

4.6 Induced Coupled Plasma – Mass Spectroscopy

Caesium analysis of the off-gas solutions was performed on an iCAP RQ ICP-MS equipped with a PFA nebuliser, quartz torch and a PrepFAST 4DX autosampler. The aqueous samples were pre-treated by 1:100 dilution with 1% ultra-pure nitric acid. The instrument ran with a continuous flow of internal standard containing Sc, In and Bi at 100, 10 and 5 μgL^{-1} respectively. The concentration data collected was normalised to the average internal standard signals.

The instrument was calibrated to detect caesium in the range 0.5 to 100 μgL^{-1} with an R^2 value of 0.99969 and forced through the blank. The background equivalent concentration was 0.013 μgL^{-1} . All measurements below this value are reported as equivalent to background. The acquisitions were collected in standard mode, with a sample uptake time of 30 seconds. The autosampler method used was “1.5ml-prepfast method”; 1.5mL of sample is required to allow enough sample to pass through the two prepFAST loops and reach the detector.

4.7 XRF Spectroscopy

XRF analysis was performed using a PANalytical Zetium spectrometer. Samples were loaded into sample holders with apertures between 20 – 37 mm. All samples were analysed using the Omnium standardless programme and a wavelength dispersive (WD) analyser. All samples were analysed in triplicate (plus three scans on a custom made boron programme using a PX7 crystal for samples containing B) and the results shown in later chapters are the average values.

4.8 Mössbauer Spectroscopy

Mössbauer spectra were collected for all iron phosphate samples using a 50 mCi cobalt-57 source in a rhodium matrix and a constant acceleration spectrometer. The spectra were measured relative to an α -Fe foil standard and fitted using RECOIL analysis software [92]. 6 - 8 Lorentzian doublets were fitted to each spectrum, based on fitting procedures reported in the literature for similar compositions [73], [75], [93].

4.9 Raman Spectroscopy

4.9.1 Bulk Studies

Raman spectra on bulk glass samples were recorded with a Renishaw Invia Raman spectrometer equipped with a CCD detector, using a green line (514.5 nm) laser at 20 mW laser power and a $\times 50$ objective. A silicon calibration specimen was used to calibrate the spectrometer before each use. Each sample was scanned between 100 and 2000 cm^{-1} , with a 10 s exposure time, 10 accumulations were collected for all IPG samples and 50 accumulations were collected for the borosilicate series.

4.9.2 Gas State Raman Spectroscopy

An OceanOptics Raman spectrometer with a fibre-optic coupled probe and a 10 mW, 532 nm green laser was used to obtain gaseous Raman spectra in-situ. The probe sat in a BWTek gaseous flow cell with a fused silica viewing window. The average working distance for the probe was approximately 7.5 mm. Scans ranged between -100 and 4000 cm^{-1} , with an exposure time of 5 minutes per scan. The experimental set-up and data treatment of the gaseous Raman data are discussed in detail in Chapter 5.

4.9.3 Analysis and Data Treatment of Solid-State Raman Spectra

A background removal was applied to all spectra using the background removal tool in Renishaw's WiRE 4.0 software. A cubic spline interpolation method was chosen, with user selected nodes at approximately 100 cm^{-1} either side of the main band, the origin (200 cm^{-1}) and the end point (2000 cm^{-1}), a similar selection procedure to one employed by Le Losq et al. and Behrens et al. to maintain reproducibility and avoid the use of arbitrarily selected points [94], [95].

The dominant peaks of the treated spectra were then deconvoluted using IgorPro [96]. Gaussian peaks were used for all deconvolutions for consistency.

4.10 Scanning Electron Microscopy (SEM)

SEM imaging was conducted on all samples before and after caesium doping. All samples were carbon coated and treated with a conductive silver paint to avoid charge build up. All images were collected using a Hitachi TM3030 Plus, operating in charge reduction mode, with an accelerating voltage of 15 kV. Electron dispersive X-Ray spectroscopy (EDX) mapping was also conducted on all samples using Bruker's Quantax 70 software and the same parameters

listed for SEM above. Maps were collected for 10 minutes and selected samples are shown in later chapters.

4.11 Thermal Analysis

Thermal Analysis was performed using two machines. For the iron phosphate series, DTA was performed using a Netzsch STA 449 F3 Jupiter simultaneous thermal analyser. Samples of ~200 mg were placed into an alumina crucible and into the STA. Nitrogen was used as a purge gas and a protective gas with flowrates of 60 ml min⁻¹ and 20 ml min⁻¹ respectively. Samples were heated from room temperature to 1200 °C at a rate of 20 °C min⁻¹. For the sodium borosilicate series, a TA Instruments SDT-Q600 was used to perform DSC. Approximately 20 mg of sample was placed in a platinum pan and heated following the same thermal cycling programme detailed above, again under a nitrogen atmosphere.

4.12 Design and Modification of Off-gas System

4.12.1 Design Criteria

The design of the off-gas system formed an integral part of the initial stages of work described in this thesis. It was anticipated that the design would need to be modified to optimise its performance and to accommodate new features, such as the Raman flow cell. Therefore, when considering initial designs the following criteria were considered:

- **Cost**
- **Caesium accountability**
- **Compatibility with furnace and furnace temperatures**
- **Ease of modification**

Cost – The budget for the project did not facilitate expensive components, especially given the novel and unproven nature of the design. Additionally, to avoid cross contamination between experiments, it was expected that there would be multiple components that would be single use.

Caesium accountability – The system was intended to enable more accurate determination of caesium volatility. This was (supposed) to be achieved by creating a sealed system that would capture any volatile caesium released from the glass melt that could be washed out of the system using a suitable medium and the concentration measured using ICP-MS. This information along with the analysed composition of the glass was intended to enable a more accurate mass-balance and in theory, allow for full accountability of all the caesium, both in the glass and volatile species.

Compatibility with furnace and furnace temperatures – Due to the temperatures associated with glass melting, any design must be able to maintain structural integrity at high temperatures. Additionally, as all experimental work was to be completed in a designated furnace located in a fume cupboard, any design had to fit into both the furnace and fume cupboard.

Ease of modification – The end goal for the design was to incorporate a system capable of differentiating between difference caesium bearing volatile species, however as there was no definitive time scale as to the procurement of such system, initial designs were produced with future modifications in mind. Creating a simple to modify design also allowed for incremental changes to improve the efficiency of the system.

4.12.2 Initial Design

A literature survey was conducted with the aim of identifying possible off-gas systems (or aspects of different off-gas systems) that could be used in this work. Several laboratory scale systems were identified, with aspects of each design featuring in the first iteration of the system used in this work.

Figure 4.1 shows Kamizono et al.'s design that was employed to investigate volatility in HLW simulant studies [97]. This design clearly met the first three design criteria, however it was decided that the system would be difficult to modify to allow for any real time, in-situ measurements.

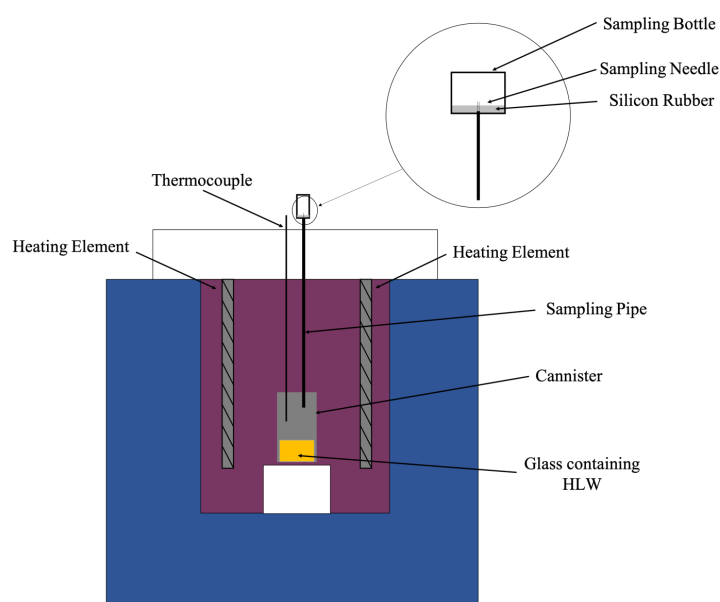


Figure 4.1: Schematic of apparatus used by Kamizono et al. [97]

Figure 4.2 (ref. [98]) and Figure 4.3 (ref. [55]) share several similar design features, including some form of gas washing system/condenser and forced airflow. Sill et al. and Banerjee et al. both employ refractory tubing to withstand the required furnace temperatures and both feature transition pieces to join the alumina components to standard laboratory glassware.

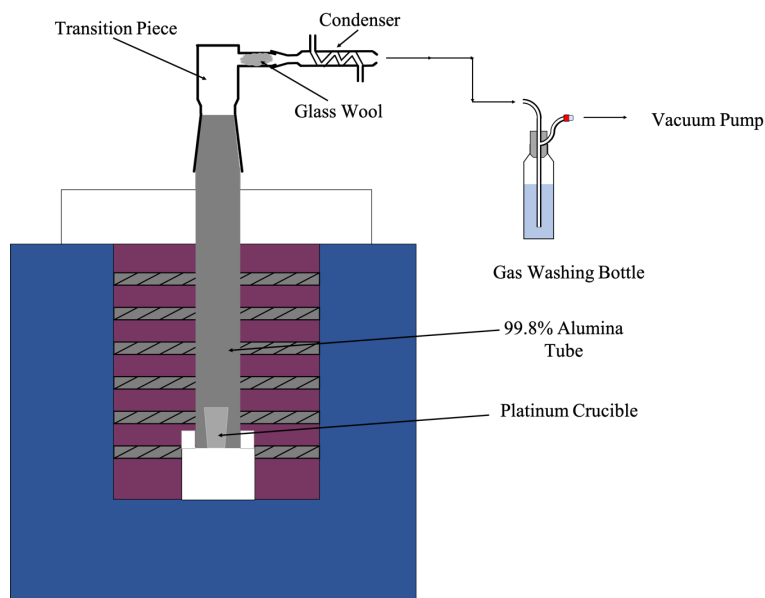


Figure 4.2: Schematic of apparatus used by Sill et al. [98]

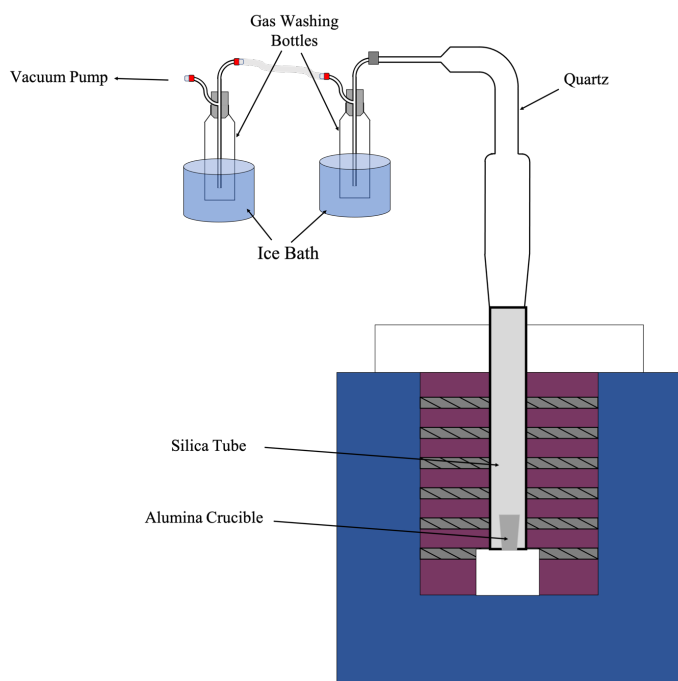


Figure 4.3: Schematic of apparatus used by Banerjee et al. [55]

A final source of inspiration for the design came from a different type of thermal treatment under consideration for nuclear waste, hot isostatic pressing (HIP). A major benefit of using design features from the HIP system was the in-house expertise and availability of equipment at the university of Sheffield. Figure 4.4 shows a schematic of a standard HIP canister, along with the proposed modification. Figure 4.5 shows how the modified HIP canister would be integrated into an off-gas system and the first prototype of the laboratory scale off-gas system used.

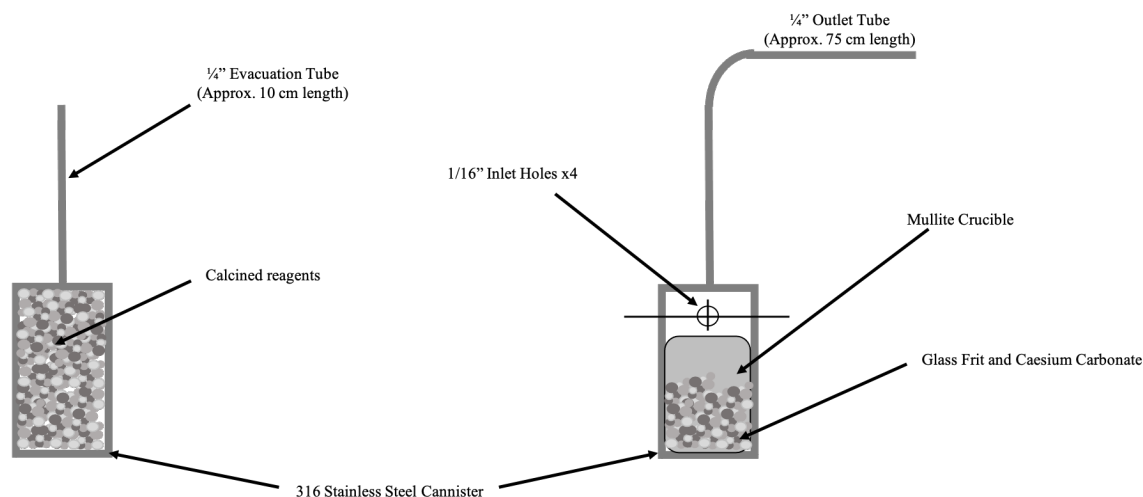


Figure 4.4: Left - Standard HIP Canister, Right - Modified HIP canister

The first iteration of the off-gas design incorporates the welded stainless steel canister of the HIP can system, ensuring good traceability of the caesium volatiles and relatively low cost, as these canisters were produced in-house and replaced after each experiment. The steel outlet tube was connected to borosilicate glass gas washing bottles using a Swagelok compression fitting. Gas washing bottle 1 contained 150 mL of 10% HNO_3 . Nitric acid was selected from Banerjee et al.'s system and the concentration is also the same as that used in Banerjee et al.'s experiments [55]. Gas washing bottle 2 contained a small amount of calcium hydroxide to protect the vacuum pump by neutralising any acidic vapours produced. The final component (not shown in Figure 4.5) is a vacuum pump, employed to encourage volatiles through the system.

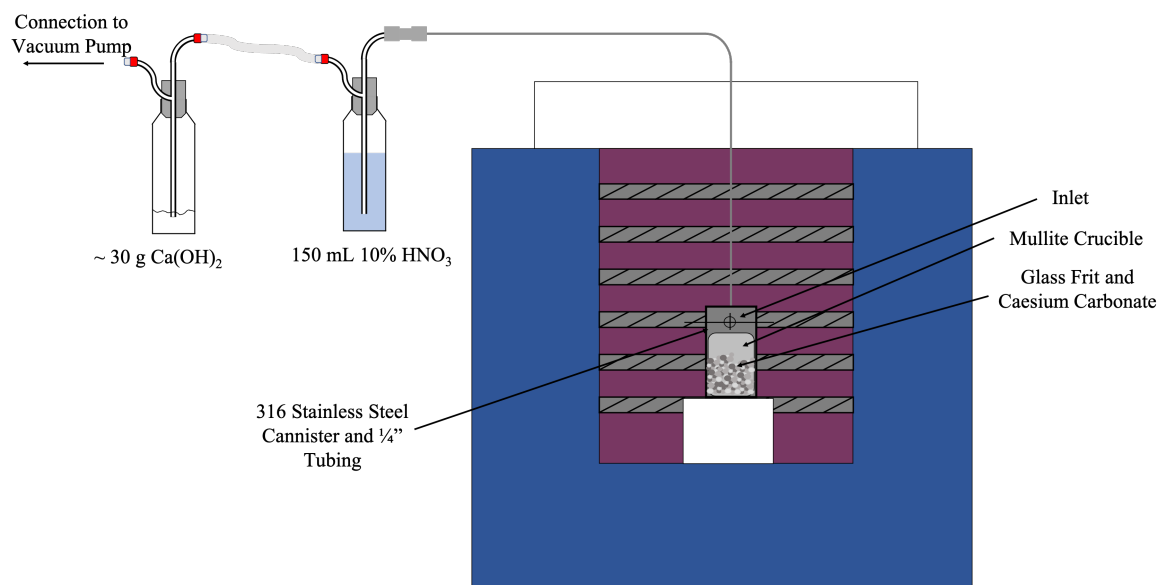


Figure 4.5: First Iteration of Off-Gas Design

4.12.3 Second Iteration of Off-Gas Design

Initial trials conducted using the first design showed significant scaling of the stainless steel (as shown in Figure 4.7), causing contamination of the glass melt in the canister and the system wash through. The stainless steel used in the first trial was stainless steel 316, in the second iteration of the design, this was replaced with stainless steel 310, as the 310 grade has better scaling resistance at high temperatures. Additionally, the vacuum pump was removed and forced airflow was produced by a nitrogen purge system, this also meant the addition of inlet tube to the main canister and the replacement of $\text{Ca}(\text{OH})_2$ in gas washing bottle 2 for 10% HNO_3 , Figure 4.6 shows the second iteration of the off-gas design. A drawback of the modifications made was a reduction of the caesium volatiles seen in the gas washing bottle solutions as can be seen in Figure 4.10 and Table 4.3.

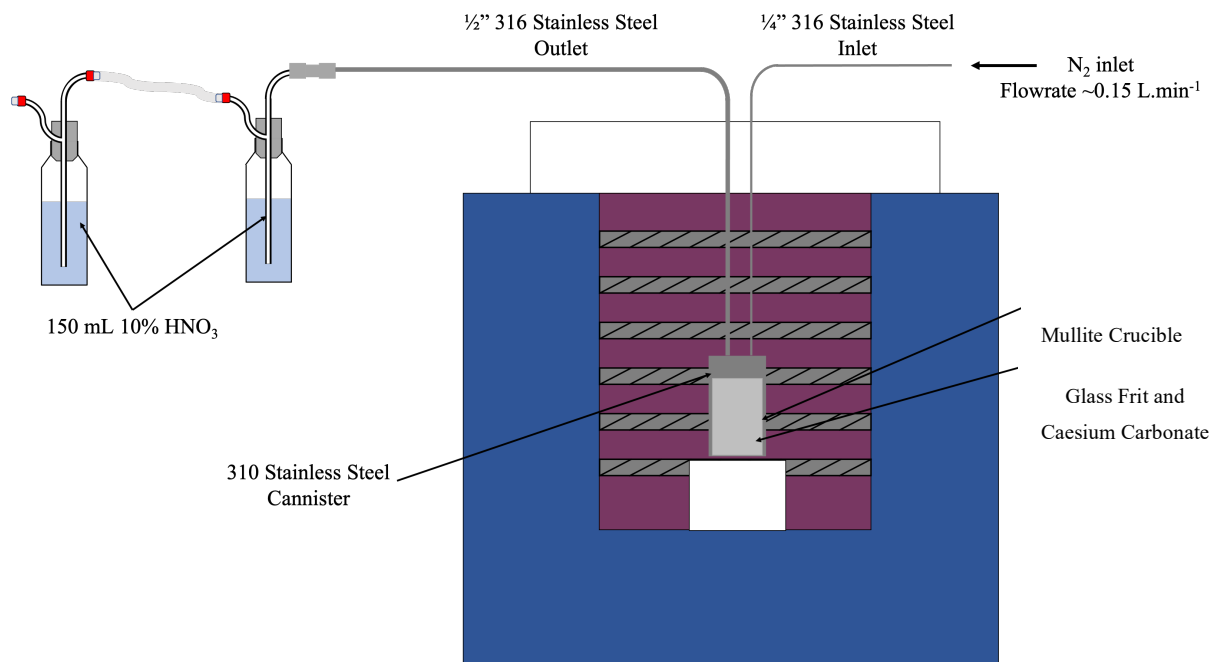


Figure 4.6: Second iteration of off-gas design



Figure 4.7: Scaling observed in 316 stainless steel canisters.
Left: Inside surface of the lid, right: external scaling

Third Iteration of Off-Gas Design

It was thought that in the second design, the caesium was either plating out in the stainless steel section of the off-gas system, before the gas washing bottles, or being entrained by the nitrogen carrier gas through the entire system. Figure 4.8 shows the third iteration of the design, incorporating insulation the stainless steel tubing, and a water coolant system around gas washing bottle 1.

The modifications made to the third iteration of the off-gas system did not improve the caesium retention, as can be seen in Figure 4.10 and Table 4.3. As there was no improvement to the caesium retention, the modifications were removed.

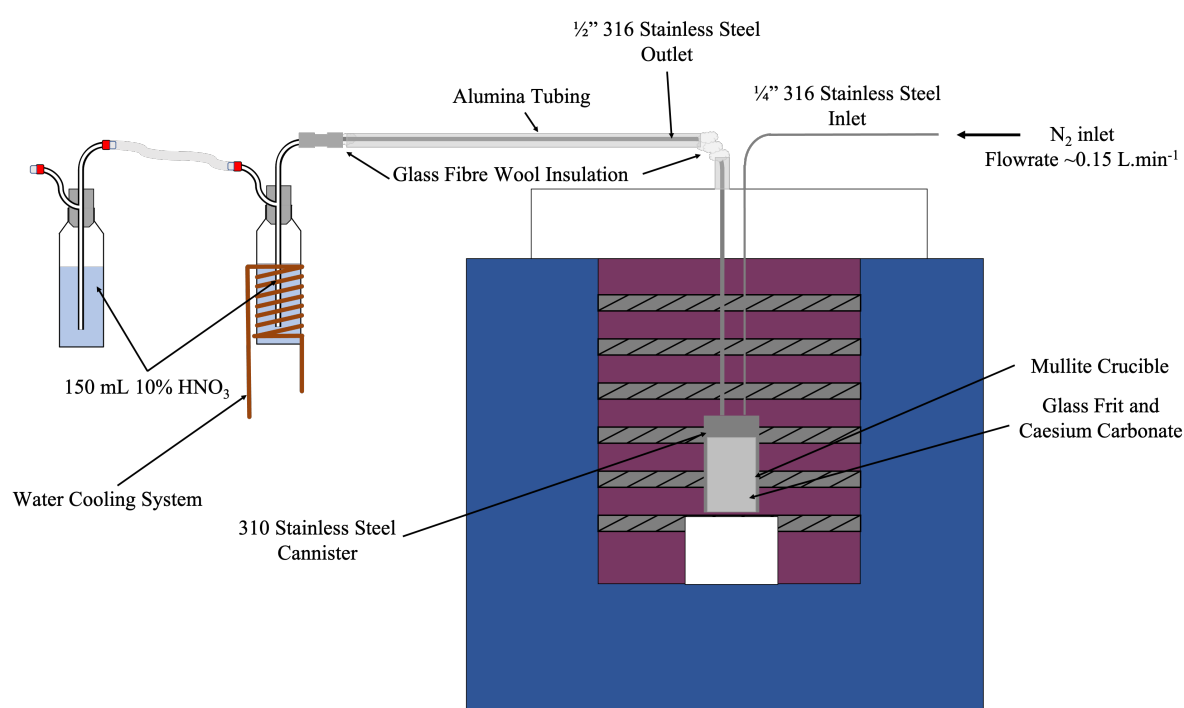


Figure 4.8: Third iteration of off-gas system

4.12.4 Final Design Used in This Work

The final modifications to the off-gas system coincided with the arrival of a fibre-coupled Raman spectrometer. Due to the time limitations of the project, it was decided that no further modifications would be made to the system to ensure the results collected using the Raman spectrometer were comparable across all experiments. Figure 4.9 shows the final design of the off-gas system, the Raman spectrometer was connected to the system using a flow cell. Further details of the Raman spectrometer can be found in Section 5.6.

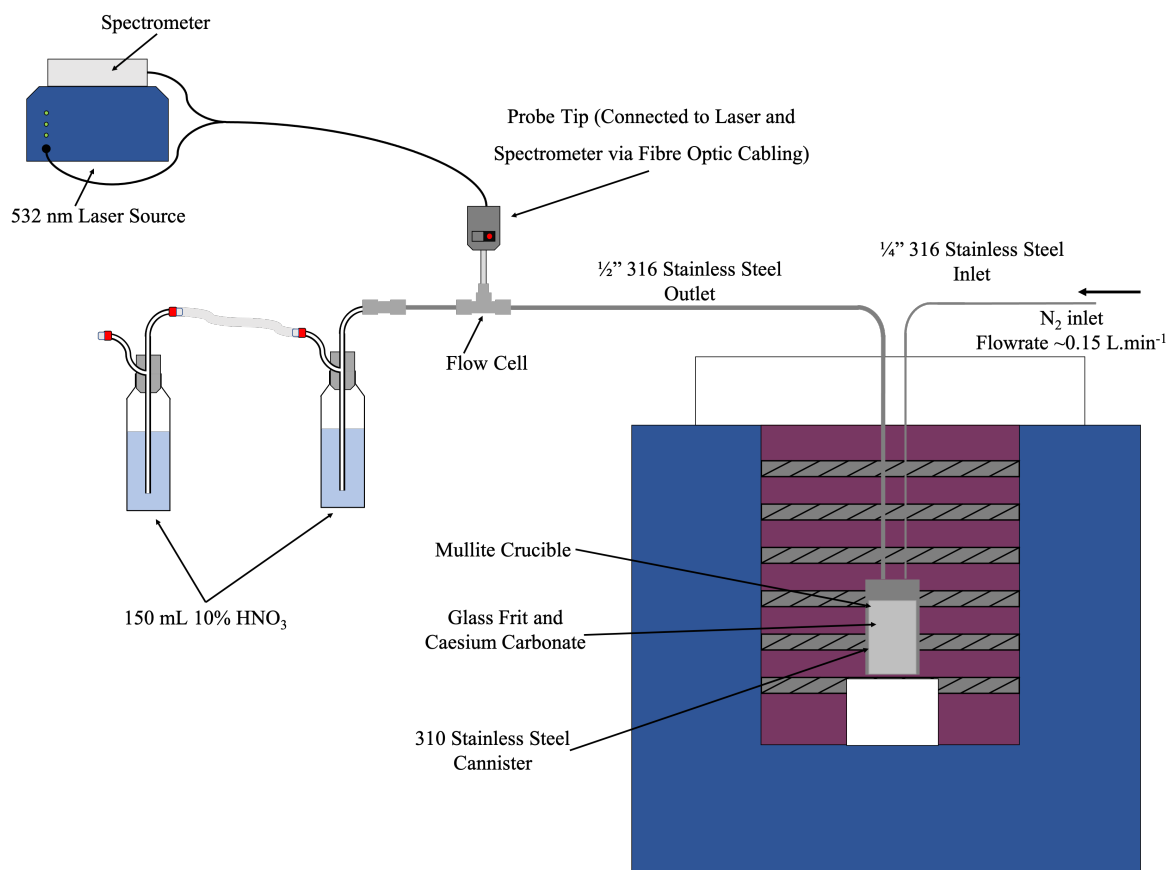


Figure 4.9: Final design for off-gas system with in-situ Raman spectrometer

The flow cell has a maximum operating temperature of 150 °C and the Raman probe has a maximum operating temperature of 80 °C. Therefore, to ensure the gases passing through the flow cell did not exceed 150 °C, the alumina and glass fibre wool insulation were removed. As it was presumed that the gases would now be at a lower temperature as they reached the gas washing bottles, the cooling system was deemed surplus to requirements and removed.

Figure 4.10 shows the measured and expected caesium concentrations in several samples. The expected values were calculated by subtracting the caesium concentration measured in the glass from the initial caesium concentration. Table 4.3 gives a brief description of the experimental conditions, including the off-gas design iteration and wash through procedures employed to improve the caesium accountability.

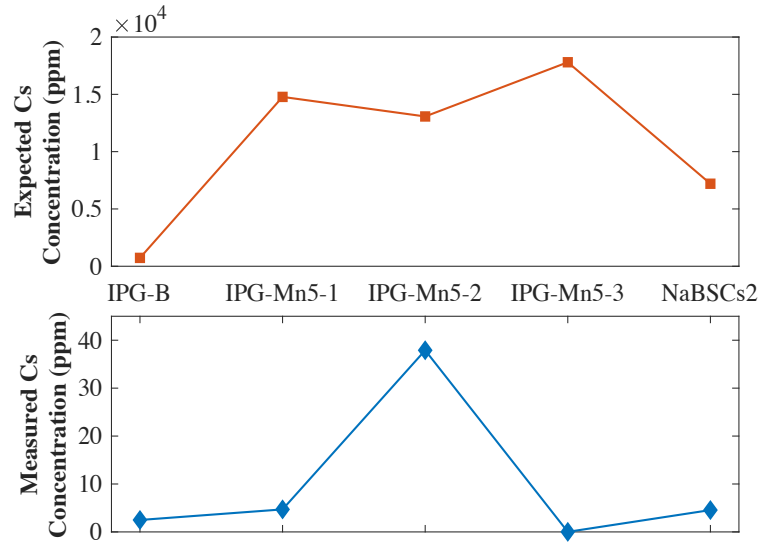


Figure 4.10: Caesium concentrations in off-gas wash through solutions (top=expected Cs concentrations, bottom = measured Cs concentrations) see Table 4.3 for experiment details

Table 4.3: Off-gas wash through procedures to accompany Figure 3.10

Sample ID	Design Iteration	Off-gas wash through procedures
IPG-B	1	All components (up to 2 nd gas washing bottle) rinsed with 10% HNO ₃
IPG-Mn5-1	2	All components (up to 2 nd gas washing bottle) rinsed with 10% HNO ₃
IPG-Mn5-2	3	All components (up to 2 nd gas washing bottle) rinsed with 10% HNO ₃
IPG-Mn5-3	3	All steel components placed into a beaker of 10% HNO ₃ that was then placed on a hot plate and held at ~90 °C for 6 hours.
NaBSZn20Ca80Cs2	4	All steel components placed into a beaker of 10% HNO ₃ and then scrubbed using a wire brush attachment and a

Dremel tool to remove any scale formed on the inside surfaces.

Comparing the final design of the off-gas system against the initial design criteria, it can be said that most of the criteria are satisfied. The system has been proven to be easily modified, as shown by the several iterations of the design described above. The system is compatible with the furnace system and the cost of the off-gas system was low. However, as can be seen from Figure 4.10, the system is not capable of achieving 100% caesium accountability, although this is something that could be improved on with further modifications. Due to the time constraints of this project, a decision was made to delay any further modifications to produce comparable results across all of the experiments where the Raman system was employed. ICP-MS analysis of the off-gas solutions produced from the experiments conducted in Sections 6 and 7 are not discussed due to the large discrepancies between measured and expected caesium concentrations. Some suggested modifications to the system to ensure all design criteria are met are given in Section 9.2 Suggestions for Further Work.

5 Raman Spectroscopy

5.1 Basic Theory

Vibrational spectroscopies such as Raman spectroscopy provide important insights into a material's structure. Importantly for the current work, Raman spectroscopy can be applied across all physical states and wide range of temperatures. Vibrational spectroscopies use a source of electromagnetic radiation with a known energy that can be described using the following [99], [100]:

$$E_p = hc\bar{\nu}$$

Equation 5.1

where E_p is the energy of an individual photon, h is Planck's constant ($6.63 \times 10^{-34} \text{ m}^2 \text{ kg s}^{-1}$), c is the speed of light ($3.00 \times 10^8 \text{ ms}^{-1}$) and $\bar{\nu}$ is the wavenumber, commonly measured in cm^{-1} . If a sample is placed in the path of the electromagnetic radiation, the two will interact. In order to discuss the different mechanisms used for different types of vibrational spectroscopy, the energy of the sample must first be defined. The energy of a molecule can be considered as the sum of the translational, electronic, vibrational and rotational components.

$$E_{total} = E_{electronic} + E_{translational} + E_{vibrational} + E_{rotational}$$

Equation 5.2

Photons and molecules can interact, leading to the photon energy being transmitted, absorbed or scattered. For Raman spectroscopy, the event involves two photons, an incident photon and a scattered photon. An inelastic collision occurs between the incident photon and the molecule, resulting in a change in the molecule's energy, in particular the vibrational and rotational components. To obey the law of conservation, the energy of the resulting scattered photon must have a different energy to the incident photon, allowing for the molecule's change in energy. This relationship between the photons' energies and the molecule's energy can be seen in Equation 4.3 below, where $\bar{\nu}_i$ is the wavenumber of the incident photon and $\bar{\nu}_s$ is the wavenumber of the scattered photon.

$$\Delta E_{molecule} = hc\bar{\nu}_i - hc\bar{\nu}_s$$

Equation 5.3

From Equation 4.3, two regions are formed according to Stokes' law, the anti-Stokes region and the Stokes region. The anti-Stokes region corresponds to $\Delta E_{molecule}$ being negative and the Stokes region corresponds to a positive value of $\Delta E_{molecule}$.

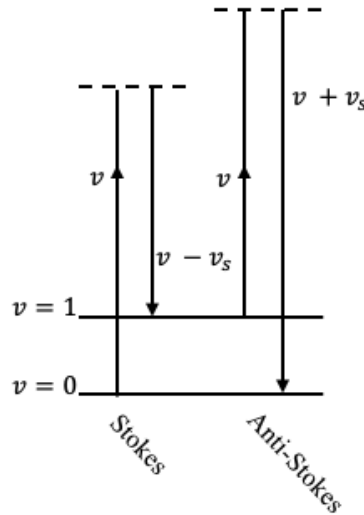


Figure 5.1 - Energy levels for Raman shift. Reproduced from [101]

Figure 5.1 shows the two events that lead to Stokes and anti-Stokes lines. Here ν represents the frequency (measured in s^{-1} or Hz), which is inversely proportional to the wavenumber, $\bar{\nu}$. In Figure 5.1, $\nu = 0$ represents the ground state of the molecule, $\nu = 1$ represents a higher, stable energy level and the dashed lines represent virtual high energy states that the molecule would temporarily occupy before returning to a lower, stable energy state.

For a material to be Raman active, it must be able to be polarised by the electromagnetic field it is subjected to. The force of the electric field will create a dipole moment (μ) within the molecule due to the opposing interactions with protons and electrons. This deforms the electron cloud, which can create a change in the polarizability, α such that:

$$\mu = \alpha E$$

Equation 5.4

where E is the strength of electric field. However, the polarizability of a molecule is not constant as E can vary over time.

$$E = E_0 \sin 2\pi\nu t$$

Equation 5.5

where E_0 is the maximum value of the strength of the electric field (constant), ν is the frequency and t is time.

Substituting Equation 5.5 into Equation 5.4 gives:

$$\mu = \alpha E_0 \sin 2\pi\nu t$$

Equation 5.6

For small displacements of the electron cloud, the polarizability can be expressed as a Taylor series:

$$\alpha = \alpha_0 + \frac{\partial\alpha}{\partial Q} Q + \dots$$

Equation 5.7

where α_0 is the polarizability at equilibrium, Q is the normal coordinate and $\partial\alpha/\partial Q$ is the change in the polarizability with respect to the normal coordinate, Q . The normal coordinate, Q , is a term used to account for small displacements and vibrations within the system, each of which have their own set of Cartesian coordinates. Each molecule will have a set of displacement coordinates that measure a molecule's displacement from a set origin, and a set of internal coordinates that describe the change in shape of a molecule. For simplicity, this can be described by Q , which varies periodically:

$$Q = Q_0 \sin 2\pi\nu_v t$$

Equation 5.8

where ν_v is the frequency of normal coordinate vibrations and Q_0 is the maximum displacement.

Combining the above equations, taking the first derivative term of the expansion only, and using the double angle formulae to express the resulting product term as a sum of 2 cos terms gives the following expression:

$$\mu = \alpha_0 E_0 \sin 2\pi\nu t + \frac{\partial\alpha}{\partial Q} \left(\frac{Q_0 E_0}{2} \right) [\cos 2\pi(\nu - \nu_v)t - \cos 2\pi(\nu + \nu_v)t]$$

Equation 5.9

Equation 5.9 highlights the three component frequencies, ν_v , $\nu - \nu_v$ and $\nu + \nu_v$. With $\nu - \nu_v$ and $\nu + \nu_v$, corresponding to $\Delta\nu = \pm 1$ seen in Figure 5.1. Importantly, it can also be seen that if $\partial\alpha/\partial Q = 0$, there has been no change in the sample's polarizability and therefore is not Raman active. A more detailed examination of the physics of Raman spectroscopy can be found in Colthup's *'Introduction to Infrared and Raman spectroscopy'* [101].

5.2 Temperature corrections

As Raman spectroscopy concerns the energy states of the subject material, temperature must be considered. This is particularly relevant in the current work where spectra were being obtained in-situ at temperature in an off-gas flow. In both crystalline and amorphous materials, research has been conducted to deduce the effect of temperature on the spectral response observed. Where temperature effects have been observed, correction factors have been formulated and applied to allow for direct comparison of spectra recorded under different temperatures. The Long equation has been used to aid comparison of spectra taken at different temperatures or with different incident excitation wavelengths [102].

$$I = I_{obs} \cdot \left\{ \bar{\nu}_0^3 \cdot \bar{\nu} \frac{[1 - \exp(-\frac{hc\bar{\nu}}{kT})]}{(\bar{\nu}_0 - \bar{\nu})^4} \right\} \quad \text{Equation 4.4}$$

where k = Boltzmann constant (1.38065×10^{-23} JK⁻¹), I = intensity and I_{obs} = observed intensity.

Equation 5.4 is based on early studies of glasses where Haas observed a temperature dependence in vitreous silica at low wavenumbers (less than 300 cm⁻¹) [103]. Above this, the effect was determined to be negligible [102]. The equation was originally intended to correct for ‘thermal effects’, however it was later determined that these intensity contributions could be attributed to the boson peak. It is important to note that Long’s correction was formulated before the acceptance of the boson peak as a real feature in glass spectra. Therefore, applying this correction will remove boson peaks where present through the term: $[1 - \exp(-hc\bar{\nu}/kT)]$. The term $[\bar{\nu}_0^3 \cdot \bar{\nu}/(\bar{\nu}_0 - \bar{\nu})^4]$ is used to remove intensity contributions from Rayleigh scattering. Therefore this correction has not been used in the current work.

Daniel et al. used a simple subtraction method to remove thermal emission contributions from high temperature spectra in aluminosilicate systems [104]. This was achieved by taking measurements without laser excitation (but otherwise under the same conditions) in addition to each sample measurement. The thermal emission contribution could then be subtracted from the sample spectra to give an enhanced signal to noise ratio. However above temperatures of 1800 K, additional background intensities were observed, which the authors attributed to absorption of the incident laser through (Si⁺ – O⁻ – Si) groups or (T – O – O⁻) peroxy groups present in the high temperature liquids. To account for the additional background intensities due to laser heating, the authors used Planck’s law and Wien’s law to approximate the intensity of the blackbody emissions. Using the temperature value of the furnace (from thermocouple

readings), T_m and a corrected temperature, T_c , they obtained the following equation to estimate the background intensities due to the additional thermal emissions.

$$\frac{I_{corr}^{blackbody}}{I_{obs}^{blackbody}} = e^{\frac{hv}{k}(\frac{1}{T_m} - \frac{1}{T_c})}$$

Equation 5.10

Using Equation 5.10 Daniel et al. corrected the high temperature spectra accounting for the initial thermal emissions and the additional thermal emissions from the absorbed incident laser light. It was estimated that the corrected temperatures were approximately 20 K higher than the nominal furnace values. As Equation 5.10 is frequency dependent, the spectra collected had to be corrected for each laser wavelength.

Due to the difficulty of applying Equation 5.10 and the need for accurate temperature measurements to feed into the formulation, no corrections were attempted for the work described here. However, as all experiments were conducted under the same conditions, individual spectra can be considered comparable, therefore negating the need for a correction factor.

5.3 Raman Spectroscopy and glasses

Whilst NMR spectroscopy is the more quantitative technique, Raman spectroscopy is often more readily available and still offers an invaluable insight into structures with short and medium range order. Raman spectroscopy can also probe the connectivity of the glass network, aiding the fundamental understanding of how the structure of a glass is arranged in 3D space and how that affects a particular composition's properties.

As discussed in Section 3.1, the structure of silicate, borosilicate and phosphate glasses differ, and these differences can be observed using Raman spectroscopy. As can be seen in Table 5.1, the key vibrational modes observed in borosilicate glasses can be assigned to silicate and borate units. Alkali or network modifier additions to these systems influence the intensity ratios between these peaks, as they are responsible for changes in the network connectivity. The addition of alumina to these systems also has an influence on the boron environment in the glass, as alkali will preferentially associate with AlO_4^- tetrahedra [105]. MRO units such as danburite like structures are listed in Table 5.1 as these have been shown to exist in borosilicate systems [8], [106], [107].

Table 5.1: Table of major Raman modes considered for borosilicate glasses

Peak (cm ⁻¹)	Assigned Structural Group	Reference
435, 495, 1150	Q ⁴	[105], [106]
540, 1000 – 1090	Q ³	[105], [106], [108], [109]
590, 850, 950	Q ²	[105], [106], [108], [109]
970, 1150	Q ⁴ (B)	[106]
530	Si – O – Si symmetrical stretching	[108]
630	Ring type metaborate groups	[105], [108]
630 – 635	Danburite, [B ₂ Si ₂ O ₈] ²⁻	[8], [106], [107]
675 – 850	Borate and boroxol ring modes	[105], [107], [108], [110]
920	Stretching of borate tetrahedra	[110]
1140	Si – O – B	[110]
1300 – 1500	Trigonal borate units	[107], [108], [110]

In iron phosphate glasses, phosphate tetrahedra are the main structural unit, with the dominant feature observed in the Raman spectra being a broad band centred at approximately 1100 cm⁻¹. This band incorporates Q₀, Q₁ and Q₂ phosphate units as can be seen in Table 5.2.

Table 5.2: Table of major Raman modes considered for iron phosphate glasses

Peak (cm ⁻¹)	Assigned Structural Group	Reference
355	Bending of PO ₄ units with Fe acting as a modifier	[111]–[114]
610	(–P–O–P–) _{symm} stretching in Q ² units	[113], [114]
745	(–P–O–P–) _{symm} stretching in Q ¹ (P ₂ O ₇) ⁴⁻ units	[80], [111]–[113]
945	Q ⁰ (PO ₄) ³⁻ _{asymm} stretching	[80], [111]–[113]
1080	Q ¹ (P ₂ O ₇) ⁴⁻ _{asymm} stretching, Q ¹ (PO ₃) _{symm} stretching	
1280	Q ² (PO ₃) ⁻ _{asymm} stretching, (P=O) stretching	[111], [113], [114]

symm = symmetrical, asymm = asymmetrical

5.4 Vibrational Modes of Cs Containing Compounds

After an extensive review of the literature, no reports were found relating to Raman spectroscopy conducted on caesium species in the gas phase. The existence of these species has been inferred based on other spectroscopic techniques such as MS and infra-red (IR spectroscopy) [115]. However, there are references in the literature to Raman spectroscopy of caesium oxides and hydroxides conducted on samples in solid state which could give an insight into the expected modes in the gas phase. Reports in the literature suggest the existence of CsO, Cs₂O, Cs₂O₂, CsOH and Cs₂(OH)₂, CsBO₂, Cs₂BO₂ and mixed alkali borates [53], [63], [116]–[121].

As work conducted using other techniques suggest that caesium borates will be present in the volatile species, a literature survey was conducted to identify the Raman response of caesium borate glasses. Alkali borates are a well studied family of glasses, with several research groups investigating their structure. Osipov and Osipova looked at binary caesium borate glasses, xCs₂O–(100 – x)B₂O₃, with x ranging from 0 – 40 mol% [122]. These samples were studied over a temperature range of 20 – 1170 °C. At lower Cs₂O concentrations, the dominant peaks found in the Raman spectra were assigned to various borate ring breathing and stretching modes. At high Cs₂O concentrations, Osipov and Osipova suggest BO₂⁻ anions and BO₃²⁻ pyroborate units are formed at the expense of BO₄⁻ units and BO₃⁻ metaborate triangles. This is evidenced by a decrease in intensity at 750 cm⁻¹ (BO₄⁻ units) and 610 cm⁻¹, 1500 cm⁻¹ (BO₃⁻) whilst increased intensities were observed at 1055 cm⁻¹ and 1240 cm⁻¹. They also noted that an increased number of pyroborate and anion units were observed at higher temperatures. This

result could prove important when speculating on the expected gas phase response of CsBO₂. Compiled in Table 5.3 are the reported Raman peaks found in the literature, predominantly in solid phase or from direct observation of caesium borate glass melts using high temperature Raman spectroscopy. This table is not extensive, however it does highlight the key vibrational modes of caesium bearing species identified in the literature. Included in Table 5.3 are borate vibrational modes identified in caesium borate samples.

Table 5.3: Caesium vibrational modes in solid and liquid state Raman spectroscopy

Wavenumber (cm⁻¹)	Species	References	State
103, 457	Cs ₂ O	[123], [124]	Solid
742, 1468.5, 2176.8	Cs ₂ O ₂	[123], [125]	Solid
1134	CsO ₂	[123], [125]	Solid
455,610,752,772,805,1050,1240,1490	Cs ₂ O-B ₂ O ₃	[122]	Liquid
642	Metaborate	[126]	Solid
747	Dipentaborate	[126], [127]	Solid
792	Boroxol	[126], [127]	Solid
625, 770, 900	Pentaborate	[127], [128]	Solid
1045	Cs ₂ CO ₃	[123]	Solid

5.5 Raman Spectroscopy and Gases

The spectra observed from gas Raman spectroscopy typically consists of well-resolved peaks. Due to minimal interaction between molecules in the gas phase, the vibrational response is predominantly influenced by the molecular symmetry and can be categorised into the following groups: linear, spherical, symmetric top and asymmetric top [100]. Samples can be measured either using a containment vessel (in which case a subtraction tool is needed to remove contributions from the container material) or in-line measurements. For in-line measurements, the gaseous sample is measured as it passes through a flow cell. Flow cells vary in design, from simple single-pass systems, to more complex and expensive multi-pass designs. The main difference between single and multi-pass systems is the effective path length of the laser source used in the Raman system. Multi-pass systems employ a series of mirrors (or mirrored surfaces) that can significantly increase the effective pathlength by reflecting the laser light through the sample gas numerous times before returning to the detector of the spectrometer. This process

increases the number of interactions between the sample gas and the laser source, which can enhance the weak gaseous signals produced by as much as 300 % . However, in the current work only a single pass flow cell was available.

5.6 Current Experimental Apparatus

The spectrometer used in the experimental work described in subsequent chapters is an OceanOptics QEPro modular spectrometer, coupled with a 532nm 10mW green laser source and utilises a fibre coupled probe. The spectrometer has a thermoelectric cooler (TEC) and is kept at a constant temperature of 20 °C throughout operation.

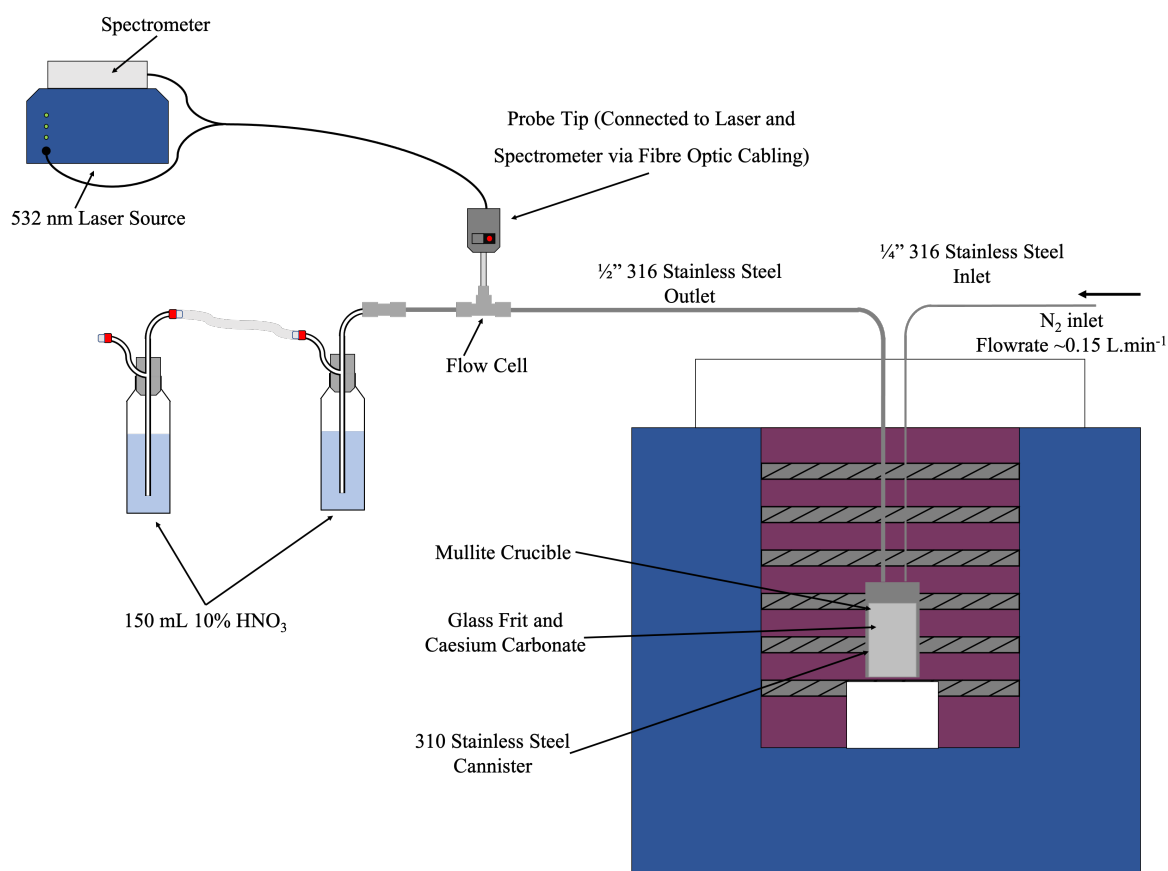


Figure 5.2: Schematic of experimental apparatus used for in-situ Raman spectroscopy experiments

As can be seen in Figure 5.2, the probe is connected to the laboratory off-gas system using a single pass flow cell with a fused silica viewing window. The working distance of the system is approximately 7.5 mm (measured from the end of the probe to centre of the flow cell diameter.)

Raman spectra were collected throughout the duration of glass melting experiments, giving insight into volatiles formed on the temperature ramp from ambient temperature to melt temperatures. The system was set to record continuously from -100 to 4500 cm^{-1} with an

acquisition time of 5 minutes per scan and a laser power of 10 mW. Using the software provided by OceanOptics, a ‘dark scan’ was performed before each experiment. This procedure was designed to remove any interference due to the fibre coupling by performing a measurement with the laser shutter at the probe tip closed. The measurement from this scan was then automatically subtracted from subsequent measurements.

5.7 Data Treatment

In the absence of the manufacturer’s recommended light source calibrator, a single phase cerium oxide sample was used to calibrate the spectra presented in this thesis. The Raman spectra of the ceria sample had been previously measured using a fully calibrated Renishaw inVia spectrometer. The wavenumber corresponding to the main peak found in the spectra was used as a calibration point and the Raman shift values of all subsequent spectra were adjusted accordingly. Figure 5.3 below shows the data collected on the QEPro spectrometer compared with the data collected on the Renishaw inVia spectrometer for a cerium oxide sample.

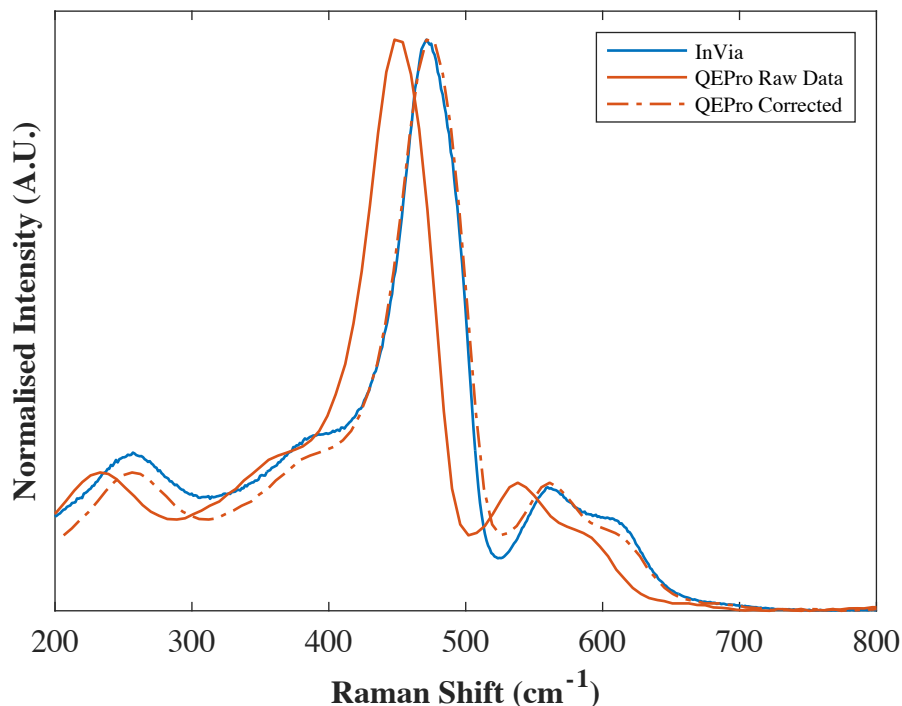


Figure 5.3: A comparison of CeO_2 Raman spectra collected on the Renishaw InVia spectrometer (solid blue line) and the spectra collected using the QEPro spectrometer (solid red orange line=raw data, dot-dash line= corrected data)

As the data collected during glass melts produced thousands of data points per experiment, MATLAB was employed as a tool to handle the large quantity of data. A script was produced

to collate the individual .txt files produced for each scan of the experiment into a more usable tabulated format (The script can be found in Appendix A).

5.8 Initial Caesium Oxide and Caesium Borate Trials

A series of experiments were conducted using the in-situ Raman spectroscopy apparatus described above to investigate the gaseous Raman response of caesium oxide and the caesium borate compounds identified in the literature (See Table 5.3). The aim of these experiments was to acquire Raman spectra for caesium oxide, caesium borate and a sodium caesium borate under the same experimental conditions as the caesium doped glass melts were performed under. Following a similar procedure described in Section 4.2, caesium carbonate was sealed into a stainless steel canister and heated from RT to 1000 °C at a rate of 5 °C / min, held at this temperature for 1 hour and allowed to return to room temperature, The main expected volatile from this experiment was Cs₂O following the decomposition of Cs₂CO₃ to Cs₂O and CO₂ (decomposition temperature is stated as 610 °C as per [132], thermal analysis indicates a decomposition event at 760 °C, see Figure 11.2 in Appendix C). The measured Raman spectra were summed and normalised (with respect to the maximum intensity of the spectra), with the normalised data presented in Figure 5.4. Figure 5.4 also shows the data for the CsBO₂ and NaCs(BO₂)₂ trials described below. Table 5.4 details the peaks detected in each experiment.

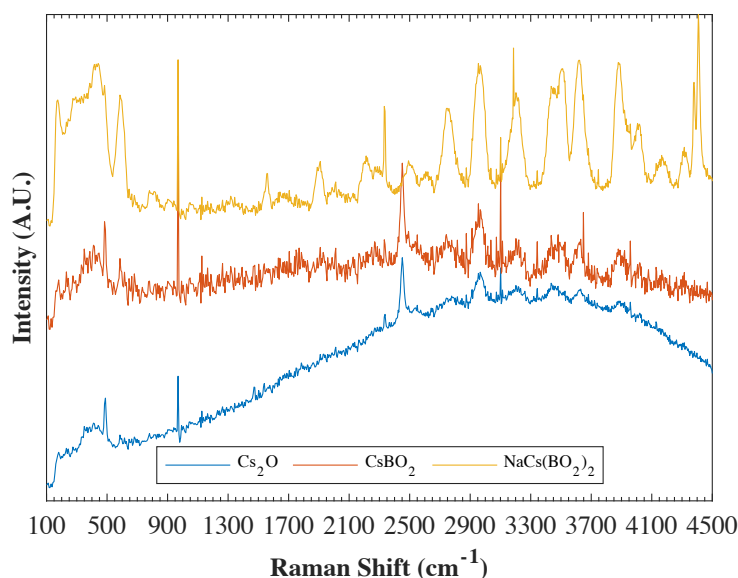


Figure 5.4: Off-gas Raman spectra of Cs₂O, CsBO₂ and NaCs(BO₂)₂ samples

The CsBO₂ sample was produced by mixing the appropriate amounts of caesium carbonate and boric acid and melting them in a platinum crucible at 1000 °C for 20 minutes, using a similar methodology to the literature [133], [134]. The melt was agitated after 10 minutes and returned to the furnace. The melt was then rapidly quenched between two steel plates, crushed and sealed into a stainless steel canister. The canister was placed into the Raman off-gas system and heated to 1000 °C at a rate of 5 °C / min. It was held at this temperature for 1 hour and allowed to return to room temperature. As discussed in Section 3.3.1, the primary volatile observed over caesium borate glass melts is a caesium borate monomer, therefore it is expected that it should also be present over the CsBO₂ melt discussed here [57]–[61]. A mixed alkali borate (NaCs(BO₂)₂) sample was produced using the same method as the CsBO₂ sample and the off-gas Raman spectra collected under the same conditions. Similarly to the CsBO₂ system, based on the literature data [57],[58], (NaCs(BO₂)₂) was expected to be observed.

A comparison of the literature values in Table 5.3 and the measured values in Table 5.4 suggest that measurements from liquid and solid state samples do not correlate with gaseous samples. There are no peaks reported in the literature beyond 2200 cm⁻¹, whereas this study investigated wavenumbers up to 4500 cm⁻¹, with the majority of features observed between 2200 and 4500 cm⁻¹. There is minimal correlation between the lower wavenumber features measured in this study and those reported in the literature. As reported in Section 3.3.1, the literature strongly suggests the vapours formed from these experiments are likely to be caesium and mixed alkali borates as intended [57] –[63]. The similarity between the spectra of the Cs₂O sample and the CsBO₂ sample suggests that only vibrational modes related to caesium modes are detected in the off-gas Raman spectra. This observation was not expected based on the literature surrounding Raman spectra collected in the solid and liquid state presented in Table 5.3, which suggest vibrational modes related to borate groups. Further work is needed to confirm the exact speciation and relative amounts of the species formed as discussed in Section 9.2. The results presented in Table 5.4, in addition to literature values, were used during the interpretation of all glass melts discussed in the following chapters and the standard spectra presented here will be referred to as the intended vapour species of each of the above experiments (Cs₂O, CsBO₂ and NaCs(BO₂)₂).

Table 5.4: Peaks identified in off-gas Raman trials

Sample ID	Major Peaks (cm⁻¹)
Cs₂O	489, 969, 2332, 2451, 2966, 3101, 3343, 3451, 3623, 3892, 3958
CsBO₂	483, 585, 969, 2451, 2746, 2954, 3101, 3202, 3343, 3435, 3481, 3630, 3648, 3889, 3958
NaCs(BO₂)₂	174, 435, 483, 591, 785, 969, 1560, 1909, 2212, 2337, 2496, 2759, 2954, 3101, 3186, 3343, 3451, 3511, 3623, 3747, 3882, 4006, 4175, 4306, 4376, 4408

6 Iron Phosphate Glasses

6.1 Introduction

This chapter describes the volatility of caesium in a series of iron phosphate glasses. A series of base glasses were prepared with the nominal molar composition $xM_yO_z(40 - x)Fe_2O_3 - 60P_2O_5$ ($M_yO_z = B_2O_3, MnO, ZnO$ with $0 \% \leq x \leq 10 \%$ in 2.5 mol% increments). Samples are named in the form IPG-XY where $X = B, Mn$ or Zn and $Y =$ the mole percent of the respective additive. All samples were remelted with a target of 2wt.% Cs_2O (98 wt.% glass frit, 2 wt.% Cs_2O). Caesium doped samples are named in the format: IPG-XY-2Cs.

The three additives selected for this work were all selected for different reasons. B_2O_3 was chosen to explore the relationship between caesium volatility and B_2O_3 concentrations, as it has been demonstrated that caesium can volatilise from glass melts as caesium borate species [53], [126]. As there is a link between crystallisation tendencies and Fe^{2+} concentrations in IPGs, MnO was added in an effort to suppress crystallisation by creating a redox couple between Fe and Mn ions [76]. Finally, it has been demonstrated that ZnO has a positive influence on caesium retention in borosilicate systems and therefore the final series includes ZnO to investigate if this influence is applicable in IPG systems [55].

All samples were characterised before and after caesium doping using XRD, DTA, XRF, SEM, Mössbauer spectroscopy and Raman spectroscopy. The following results have been separated according to the additive used and the results for IPG-Base and IPG-Base-2Cs are included as part of the IPG-B series for the majority of the techniques described below.

6.2 XRD

Figure 6.1- Figure 6.4 show that all of the base glasses produced are X-Ray amorphous, as can be observed by characteristic diffuse scattering. The traces for the caesium doped glasses can be seen in Figure 6.5 - Figure 6.7.

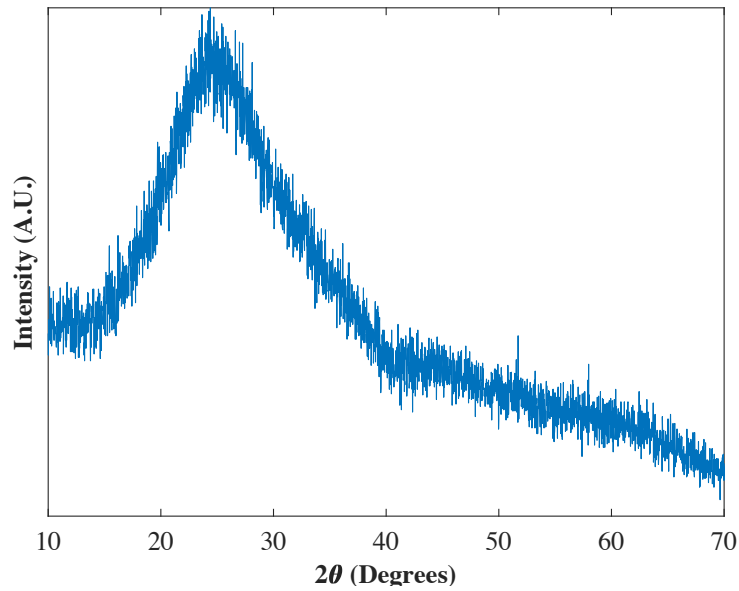


Figure 6.1: XRD of IPG-Base Glass

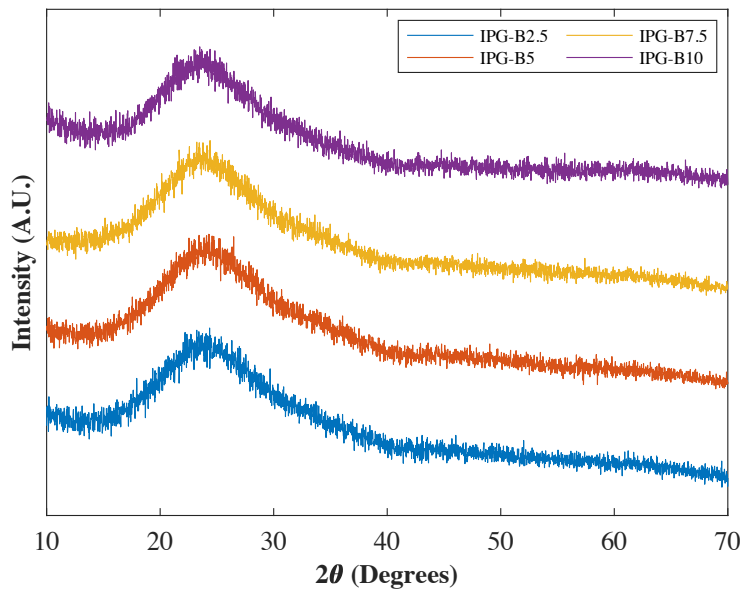


Figure 6.2: XRD of IPG-B Series

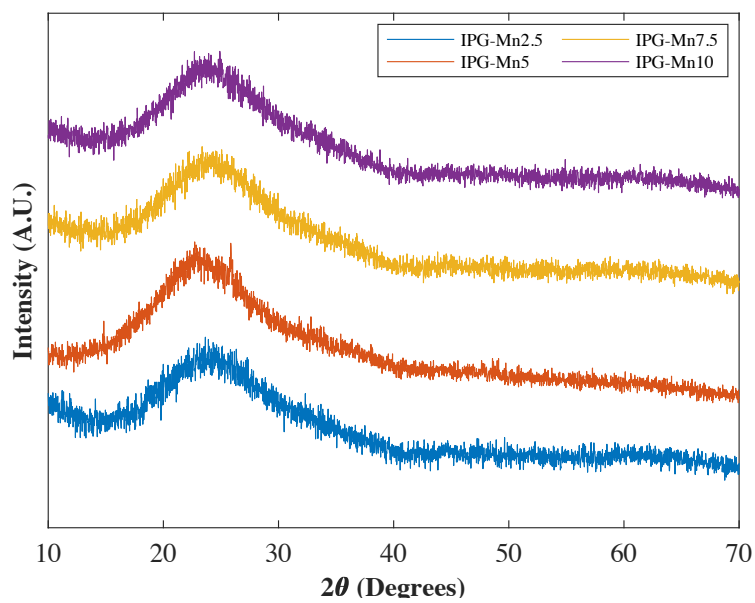


Figure 6.3: XRD of IPG-Mn Series

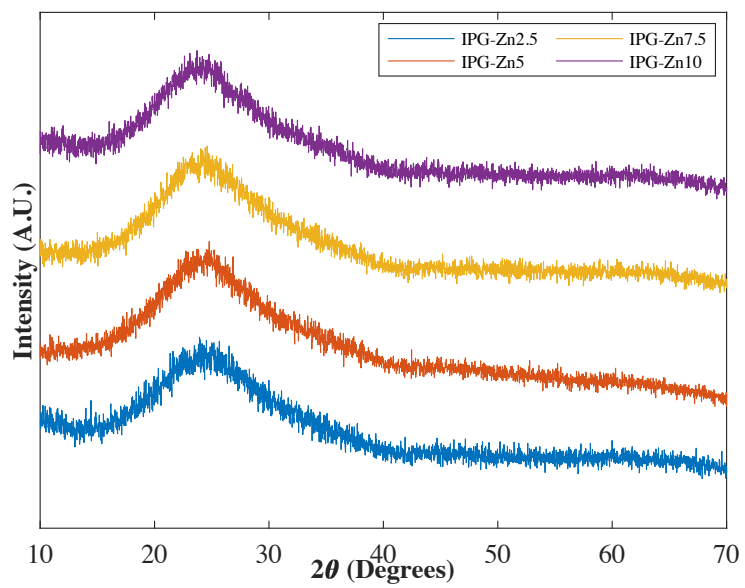


Figure 6.4: XRD of IPG-Zn Series

Figure 6.5 shows the XRD traces for the IPG-Base-2Cs sample and the IPG-B-2Cs series. The IPG-Base sample crystallised after the caesium doped remelt, forming an iron phosphate crystalline phase ($\text{Fe}_2\text{Fe}(\text{P}_2\text{O}_7)_2$ PDF 80-2315), the same phase was attributed to the IPG-B2.5-2Cs sample, however at 5 and 7.5 mol% B_2O_3 , two phases were identified, an iron phosphate phase (FePO_4 PDF30-0659) and a boron iron phosphate phase ($\text{B}_{0.57}\text{Fe}_{0.43}\text{PO}_4$ PDF 50-0210). At 10 mol% B_2O_3 , a boron phosphate phase was found to have formed (BPO_4 PDF 74-1169). 7.5 and 10 mol% additions of both MnO and ZnO suppress crystallisation during the caesium doped melts, as can be seen in Figure 6.6 and Figure 6.7. IPG-Mn-2.5-2Cs formed the same iron phosphate crystalline phase observed at low B_2O_3 concentrations ($\text{Fe}_2\text{Fe}(\text{P}_2\text{O}_7)_2$ PDF 80-2315), however a different iron phosphate phase was found in IPG-Mn5-2Cs, $\text{Fe}_2\text{Fe}_5(\text{P}_2\text{O}_7)_4$ (PDF 77-0851). Similarly, $\text{Fe}_2\text{Fe}_5(\text{P}_2\text{O}_7)_4$ formation was observed in the IPG-Zn2.5-2Cs and IPG-Zn5-2Cs samples. It can be seen in Figure 6.5 - Figure 6.7 that some peaks have not been assigned to crystalline phases, in these instances, no match was found when comparing the samples to known crystalline phases in the relevant databases.

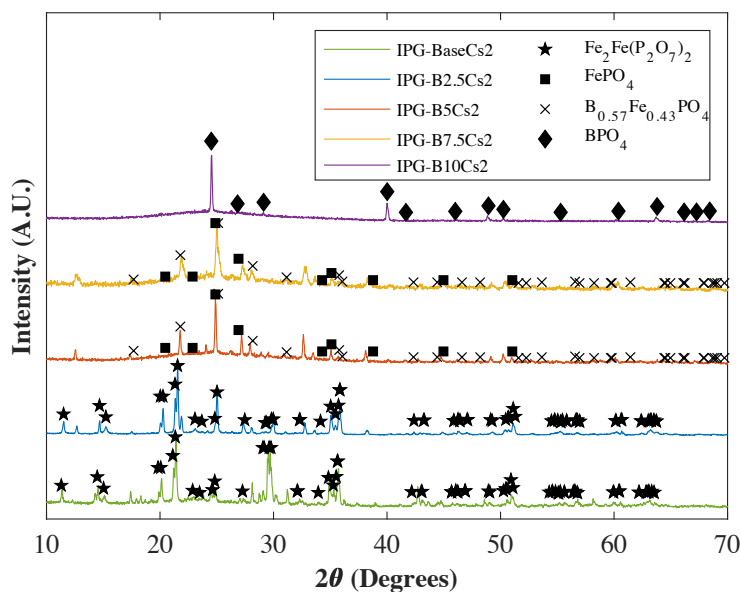


Figure 6.5: XRD of IPG-Base-2Cs and IPG-B-2Cs Series

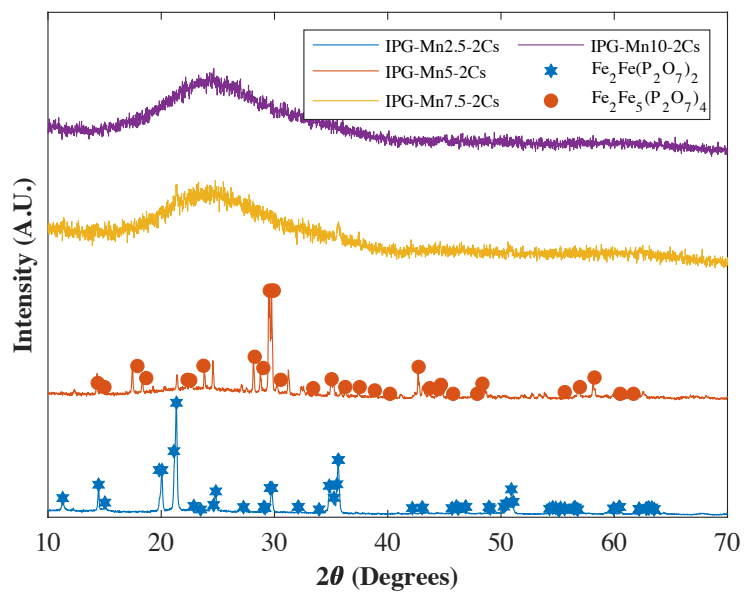


Figure 6.6: XRD of IPG-Mn-2Cs series

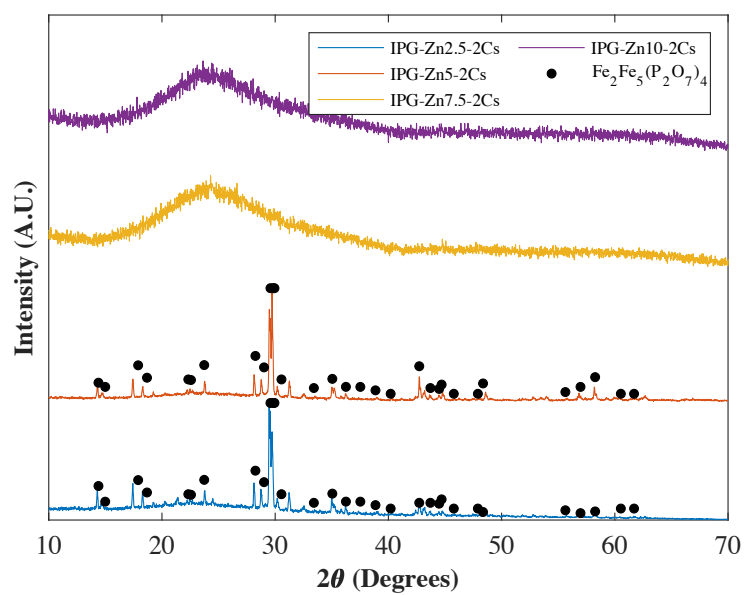


Figure 6.7: XRD of IPG-Zn-2Cs series

6.3 Thermal Analysis

Thermal cycling of the samples was intended to remove thermal history. However, cycling the samples induced phase separation which was observed as two distinct glass transition events on the second heating cycle. Several thermal events were also absent from the second heating cycle that were present in the first and that are reported for similar compositions in the literature [72], [73], [85]. These events could also help to describe the behaviour of the different glass series when remelted with caesium carbonate. Therefore, the DTA traces shown below are the data from the first heating cycle. All glass transformation and crystallisation event temperatures for all base glasses can be found in Table 6.1. Figure 6.8 shows the DTA trace of the IPG-Base glass, where multiple crystallisation and melting events can be observed between 630 °C and 930°C.

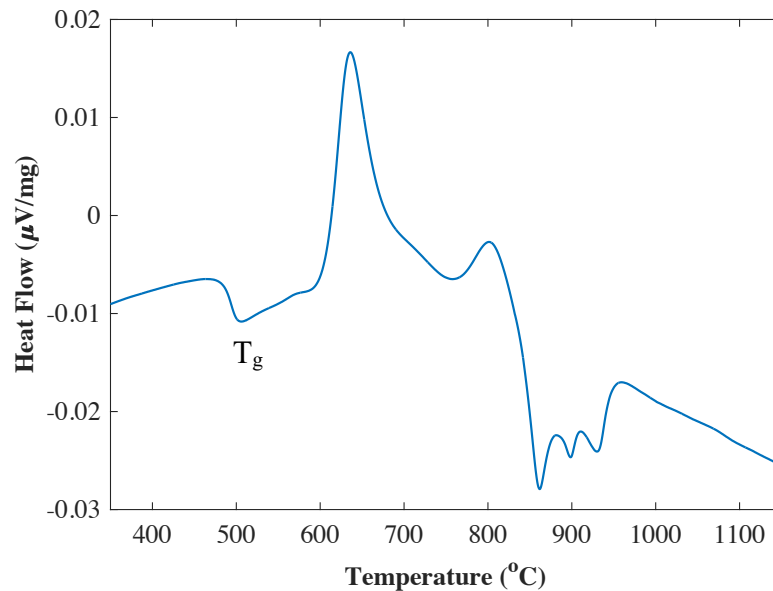


Figure 6.8: DTA trace of IPG-Base

Figure 6.9 - Figure 6.11 shows the DTA traces for the IPG-B, IPG-Mn and IPG-Zn series. An increase in T_g is observed with increasing B_2O_3 and MnO concentrations, with all glasses in the IPG-B and IPG-Mn series having a higher T_g than IPG-Base. All glasses in the IPG-B series show poor thermal stability (determined by the difference between T_g and the first crystallisation event), however the thermal stability improves slightly with increasing B_2O_3 concentrations. Both the IPG-Mn and IPG-Zn series show improved thermal stability in comparison to IPG-Base, with stability increasing with MnO and ZnO concentrations.

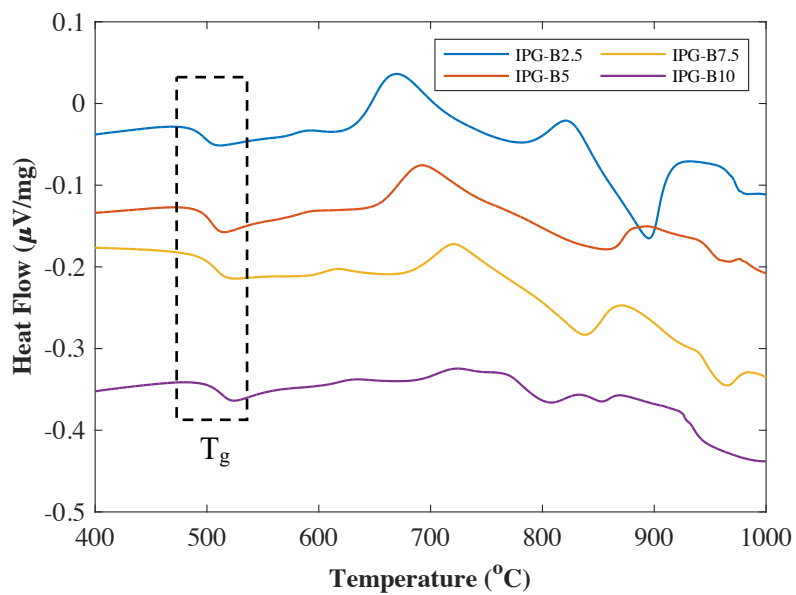


Figure 6.9: DTA traces of IPG-B Series

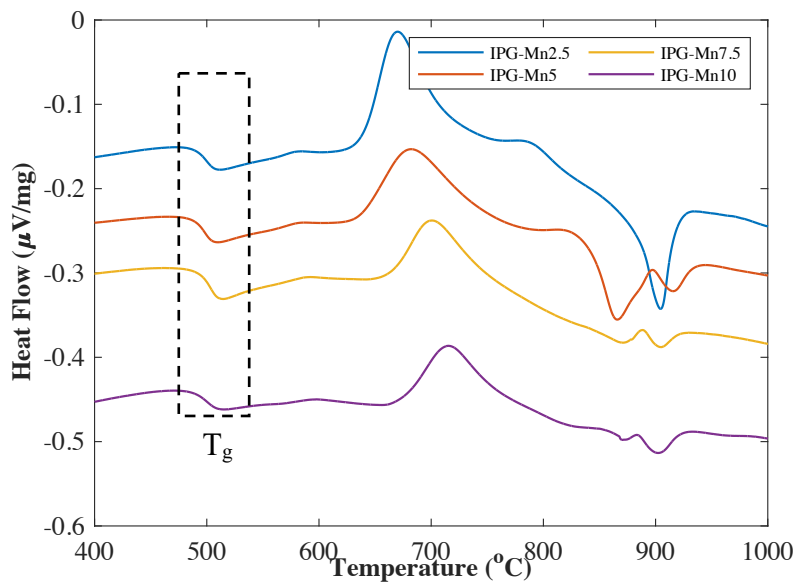


Figure 6.10: DTA traces of IPG-Mn Series

Finally, in the IPG-Zn series, the thermal features are suppressed with increasing ZnO content, with the 7.5 and 10 mol% traces appearing to have good thermal stability.

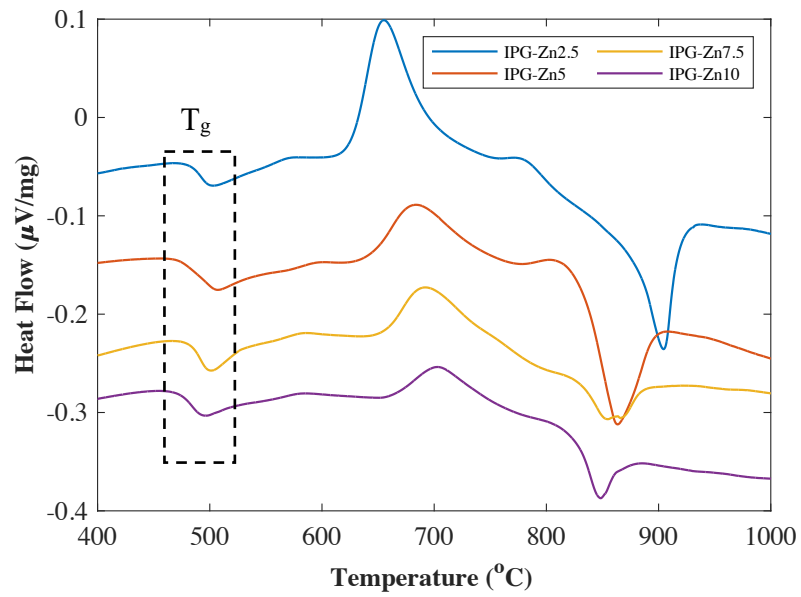


Figure 6.11: DTA traces of IPG-Zn Series

Table 6.1: Thermal event information for all IPG base glasses

Sample ID	$T_g (\pm 2)$	$T_x (\pm 2)$	$T_m (\pm 2)$	K_{gl}
	°C			
Base	506	636, 802, 910	862, 899, 930	0.56
B2.5	512	590, 671, 821	896, 980	0.25
B5	514	596, 690, 978	859, 964	0.31
B7.5	519	615, 720, 870	834, 965	0.3
B10	522	630, 722, 833	806, 854	0.61
Mn2.5	507	671, 785	905	0.70
Mn5	506	680, 775, 898	866, 916	0.94
Mn7.5	511	701, 888	870, 905	1.12
Mn10	512	714, 884	871, 903	1.29
Zn2.5	502	655, 777	905	0.61
Zn5	505	683, 807	863	0.99
Zn7.5	501	691, 828	853, 866	1.17
Zn10	493	702	848	1.43

6.4 Raman Spectroscopy

Raman spectroscopy was completed on all samples both pre and post caesium doping, in accordance with the procedure outlined in Chapter 4.9.1. Figure 6.12, Figure 6.13, Figure 6.15 and Figure 6.17 show the spectra of the undoped samples. Figure 6.14, Figure 6.16, and Figure 6.18 are residual difference plots, comparing the spectra of the IPG-B, IPG-Mn and IPG-Zn series to the IPG-Base spectra. For all the spectra used in these figures, each dataset was normalised to the maximum within that dataset. The residual difference plots show the difference in intensity between each composition and the IPG-Base composition (normalised intensity of IPG-Base subtracted from the normalised intensity of each composition).

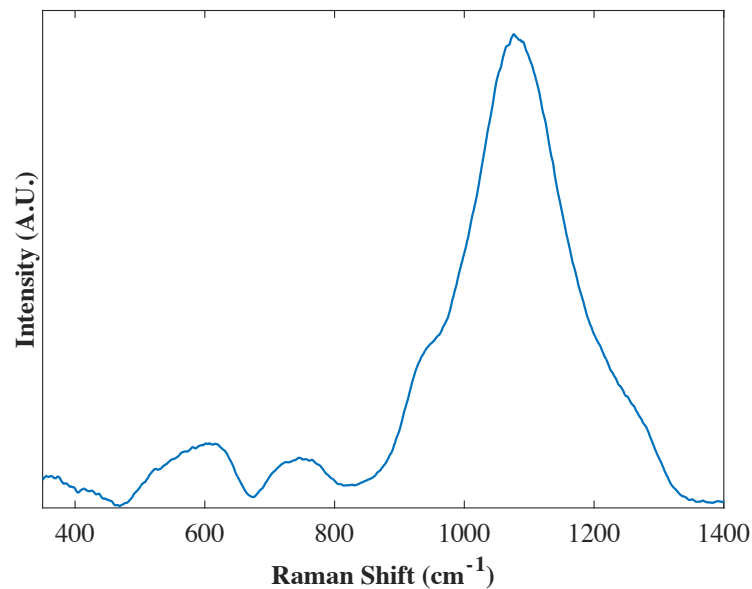


Figure 6.12: Raman spectra of IPG-Base Glass

As can be seen in Figure 6.13 and Figure 6.14, there is an increased Raman shift of the main band in each spectrum with increasing B_2O_3 content. Additionally, a shoulder is formed at approximately 1300 cm^{-1} that increases in intensity with increasing B_2O_3 content. These changes correspond to the conversion of Q^1 to Q^2 species as can be seen in Figure 6.26 in Section 6.5.

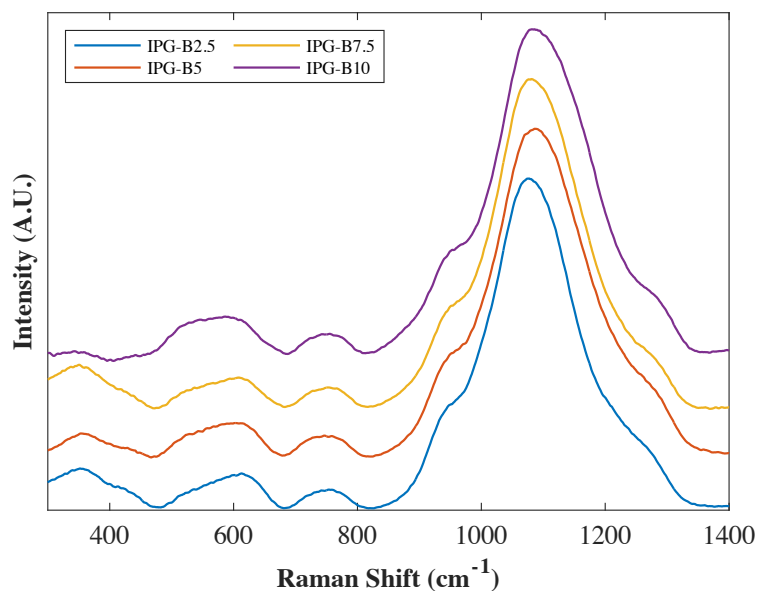


Figure 6.13: Raman spectra of IPG-B Series

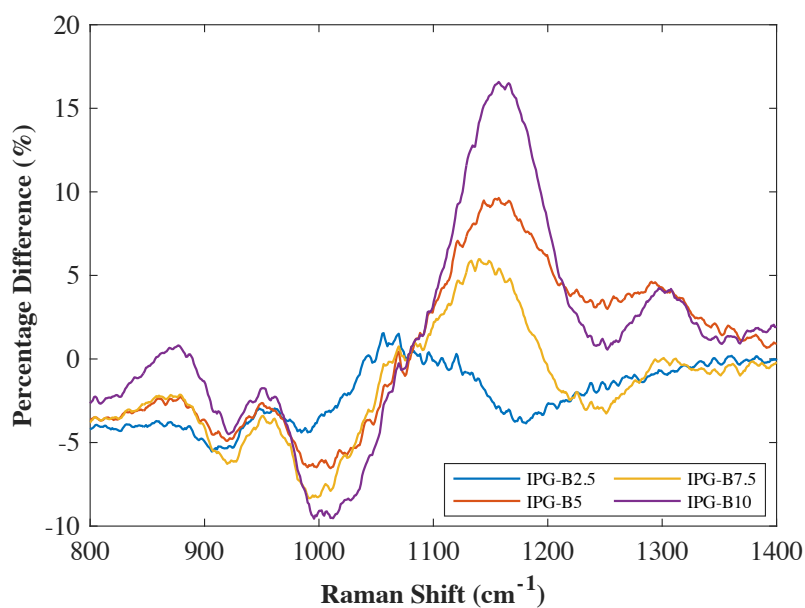


Figure 6.14: Residual difference between IPG-Base and IPG-B series

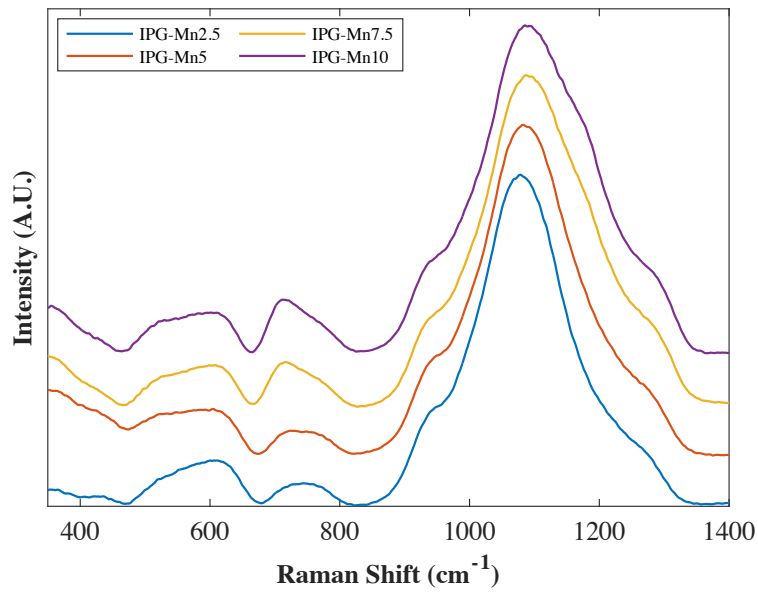


Figure 6.15: Raman spectra of IPG-Mn Series

The increasing concentration of MnO in the glass prompts a similar change in the Raman spectra to B₂O₃ additions, with an increase in the wavenumber of the main band position and a growth in the shoulder of the main band at approximately 1300 cm⁻¹. The effect of additive concentration is less incremental in comparison to the IPG-B series, with the spectra of the IPG-Mn7.5 and IPG-Mn10 samples looking almost identical.

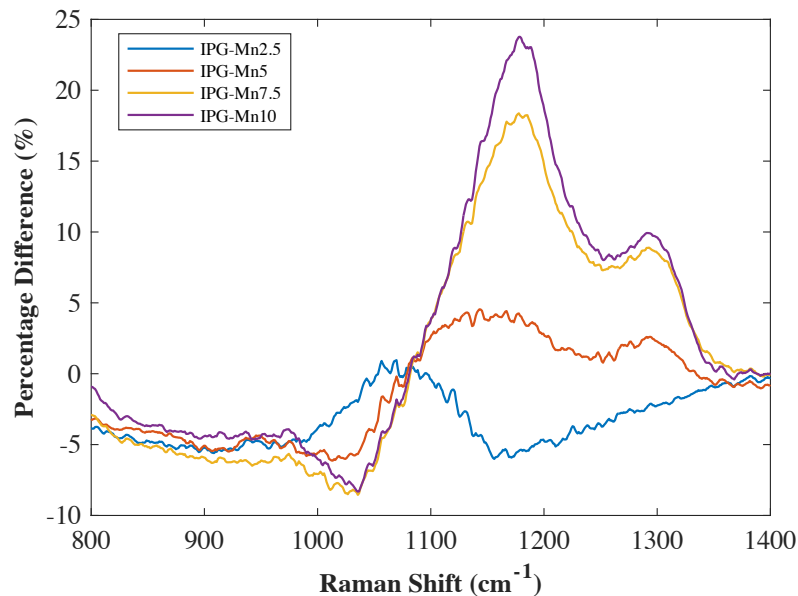


Figure 6.16: Residual difference between IPG-Base and IPG-Mn series

Finally, the IPG-Zn series shows very similar trends to the IPG-Mn series, with only a small shift to a higher wavenumber for the main band position and a high level of similarity between the 7.5 and 10 mol% samples.

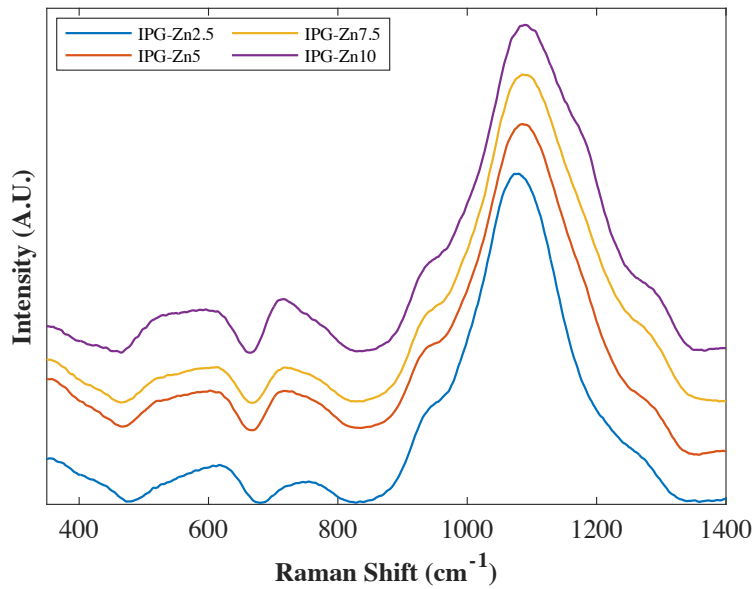


Figure 6.17: Raman spectra of IPG-Zn Series

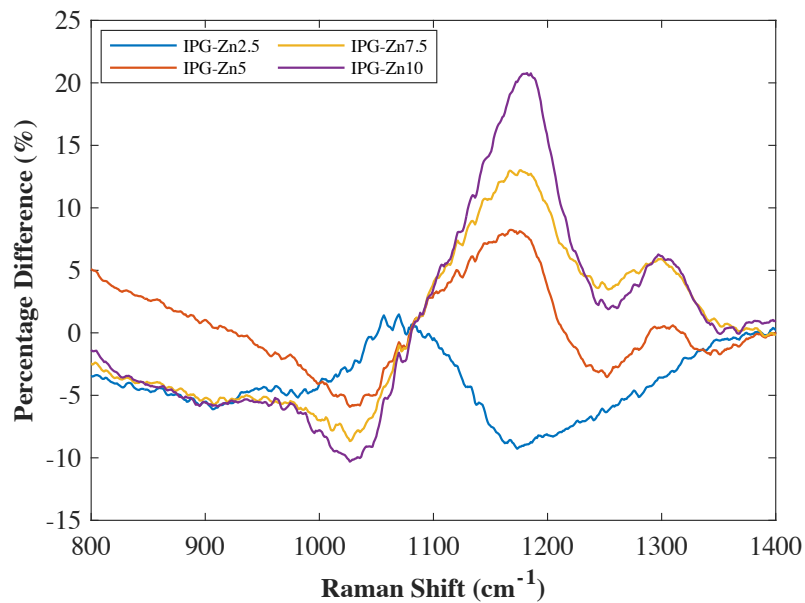


Figure 6.18: Residual difference between IPG-Base and IPG-Zn series

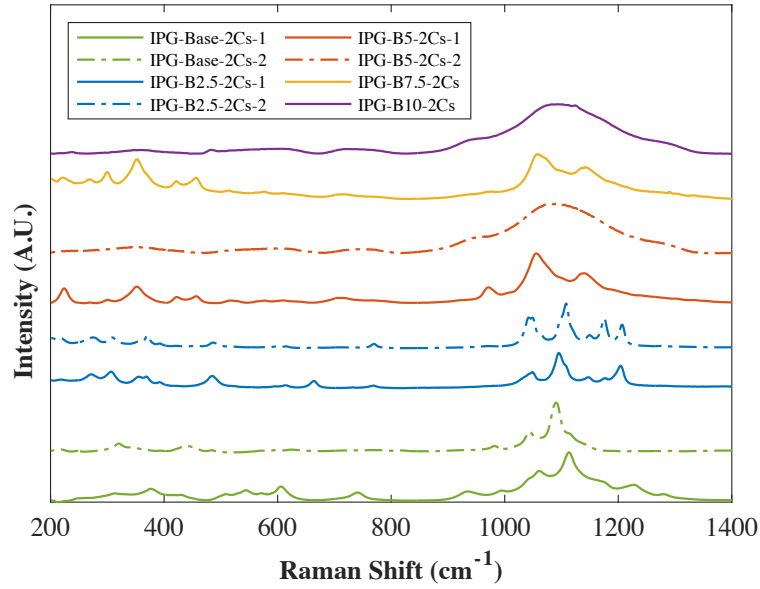


Figure 6.19: Raman spectra of IPG-Base-2Cs and IPG-B-2Cs series

Figure 6.19 - Figure 6.21 show the Raman spectra of the caesium doped glasses. In some samples, multiple phases were observed (represented as different line types in the same colour), and their corresponding Raman spectra are denoted by their sample ID and a difference in line type (solid and dashed lines of same colour represent two regions of same sample). In agreement with the XRD results shown in section 6.2, the Raman spectra for IPG-Base-2Cs, IPG-B2.5-2Cs and IPG-Mn-2Cs all appear to have the same response. IPG-Mn7.5-2Cs, IPG-Mn10-2Cs, IPG-Zn7.5-2Cs and IPG-Zn10-2Cs show almost identical responses to their corresponding base glasses as can be seen in Figure 6.22 and Figure 6.23.

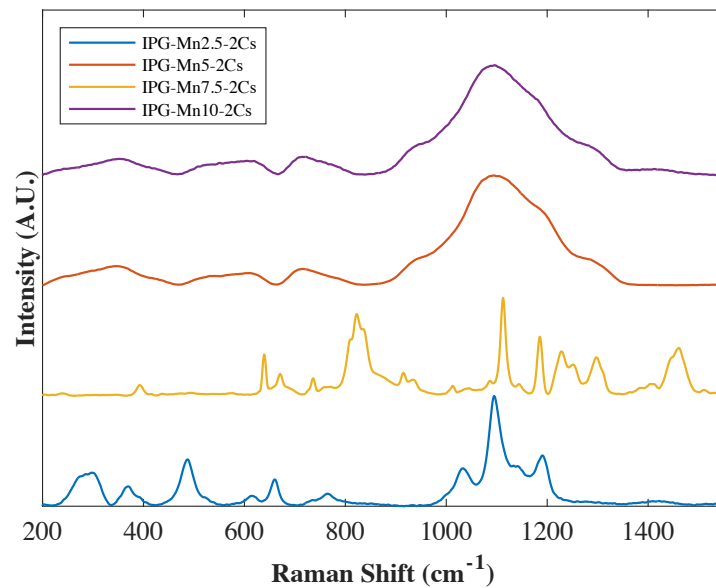


Figure 6.20: Raman spectra of IPG-Mn-2Cs series

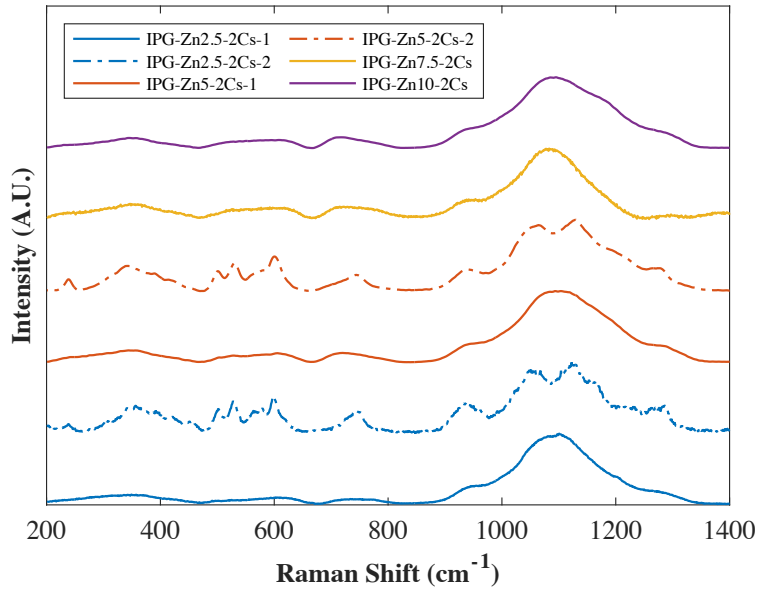


Figure 6.21: Raman spectra of IPG-Zn-2Cs series

Figure 6.24 shows the residual difference of the spectra plotted in Figure 6.22 and Figure 6.23, showing the similarity between the 7.5 and 10 mol% samples in the Mn and Zn series. In Figure 6.24 show the difference spectra for IPG-Mn7.5 and IPG-Mn7.5-2Cs, IPG-Mn10 and IPG-Mn10-2Cs, IPG-Zn7.5 and IPG-Zn7.5-2Cs and IPG-Zn10 and IPG-Zn10-2Cs. It can be seen that the spectra are in good agreement, indicating only minor structural changes after the caesium doped remelt. The IPG-Zn7.5 samples shows the biggest deviation due to the absence of the shoulder to the right of the main band.

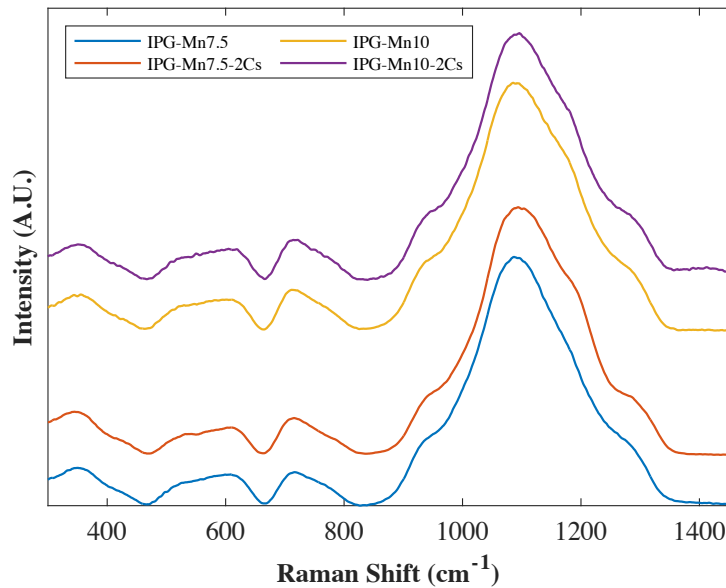


Figure 6.22: A comparison of the Raman spectra of IPG-Mn7.5 and IPG-Mn10 before and after caesium doping

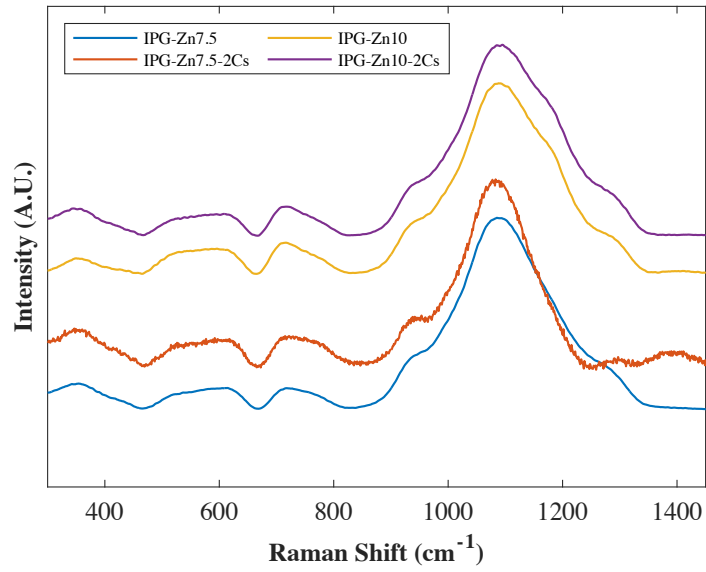


Figure 6.23: A comparison of the Raman spectra of IPG-Zn7.5 and IPG-Zn10 before and after caesium doping

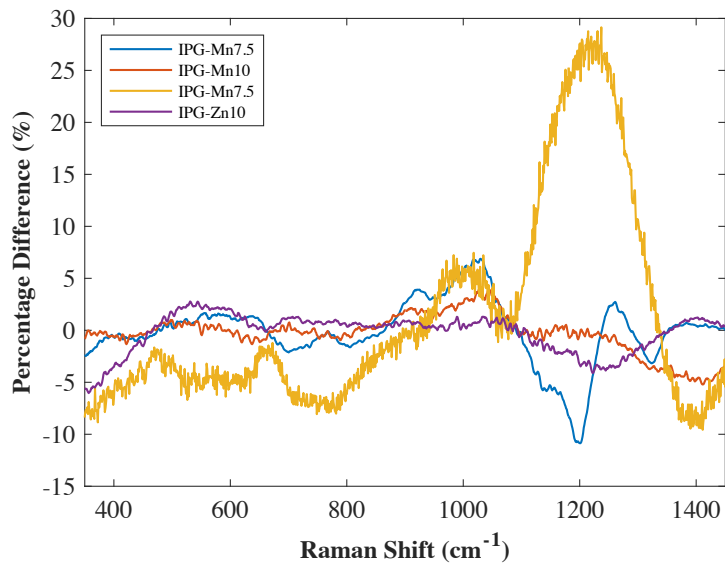


Figure 6.24: Residual Difference in Raman spectra of IPG-Mn7.5, IPG-Mn10, IPG-Zn7.5 and IPG-Zn10, before and after caesium additions

6.6 Deconvolution of the main Raman band

The main Raman band seen in all of the base glass spectra is situated between ~ 800 and 1400 cm^{-1} . Three Gaussians were used to approximate the Q-speciation within the glass networks. Pseudo-Voigt peaks were also tried however the residual difference (difference between data and fit) was significantly higher than the difference seen with the Gaussian fit and therefore Gaussians were used in all fittings. A dominant peak at ~ 1150 cm^{-1} was attributed to Q^1 species, with Q^0 and Q^2 peaks at 950 and 1200 cm^{-1} respectively. Q^1 is the dominant species in all samples, however with increasing additive concentrations, the proportion of Q^1 decreases at the expense of Q^0 and Q^2 units. The exception to this trend can be seen in the IPG-Zn10 sample, where the proportion of Q^0 increases significantly. Figure 6.26 shows the Q-speciation of all the base glasses determined from the deconvolution of the Raman spectra, an example of which is shown in Figure 6.25.

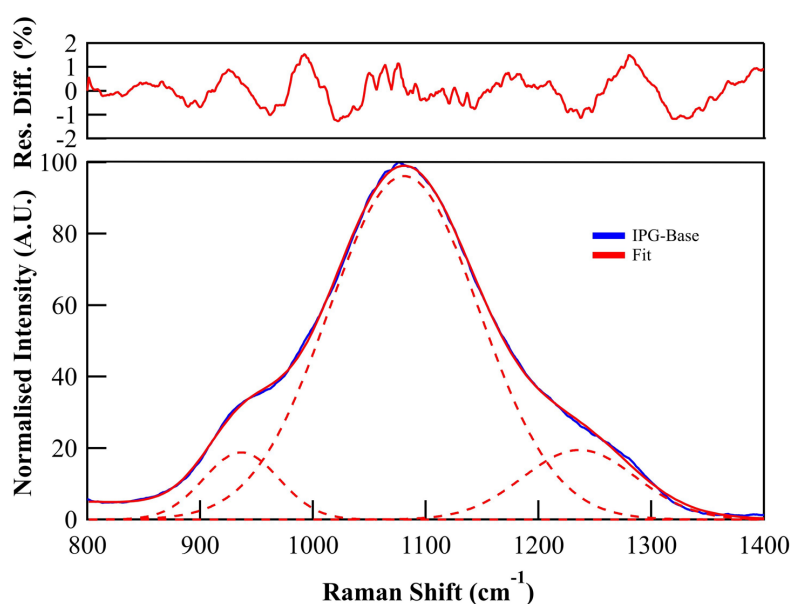


Figure 6.25: Example of the deconvolution of the Raman spectra of an iron phosphate glass

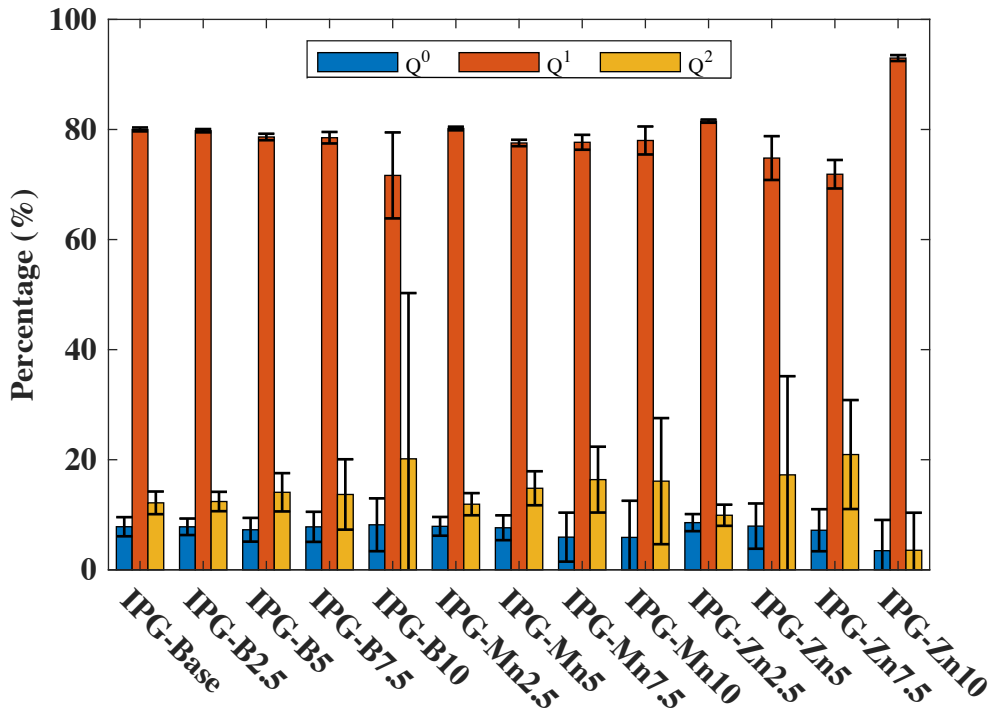


Figure 6.26: Q-speciation across all base glasses

6.7 Mössbauer Spectroscopy

Mössbauer spectroscopy was conducted following the procedure outlined in Section 4.8. These results were then interpreted using an adapted method of Bingham et al., where 8 Gaussians were fitted to each spectra, with four Gaussians assigned to each iron oxidation state [85]. Initial isomer shift (CS), quadrupole splitting (QS) and line width (LW) values were assigned using data from Bingham et al. and these values remained consistent with Bingham et. al's data after the fitting process was completed [85]. Figure 6.27 and Figure 6.28 show the Mössbauer spectra of all samples analysed in this section, along with an example fit for both a base and caesium doped sample. Table 6.2 shows the average CS, QS and LW values of each of the glasses with 5 mol% additive (both before and after the caesium doped melt), along with the estimated $\text{Fe}^{2+}/\Sigma\text{Fe}$ ratio, following the method of Dyer et al., which have been corrected to account for the recoil free fraction using the ratio $f(\text{Fe}^{3+})/(\text{Fe}^{2+}) \approx 1.30$ in line with similar compositions studied by Bingham et al. [135], [136].

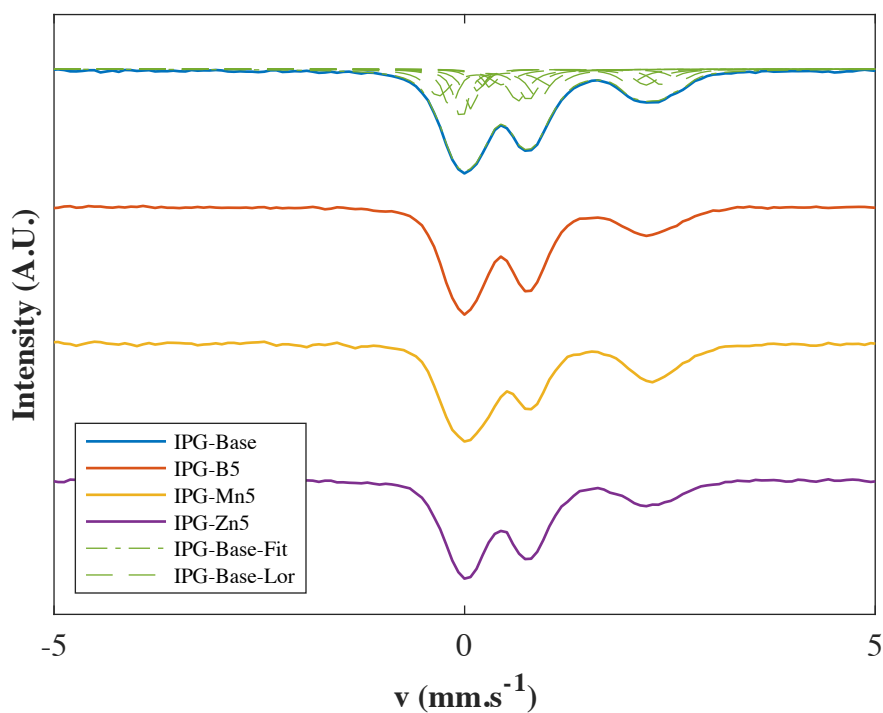


Figure 6.27: Mössbauer spectra of selected base samples and an example fit with the Lorentzian components

Literature reports suggest that the $\text{Fe}^{2+}/\Sigma\text{Fe}$ ratio can range between 15% - 50%, which is in agreement with the results presented in Table 6.2 [87]. It was expected that the crystallisation seen in the caesium doped samples may be due to the increased presence of Fe^{2+} after being re-melted under a nitrogen atmosphere. However, as can be seen from Table 6.2 the difference in the amount of Fe^{2+} in the doped and corresponding undoped samples does not support this.

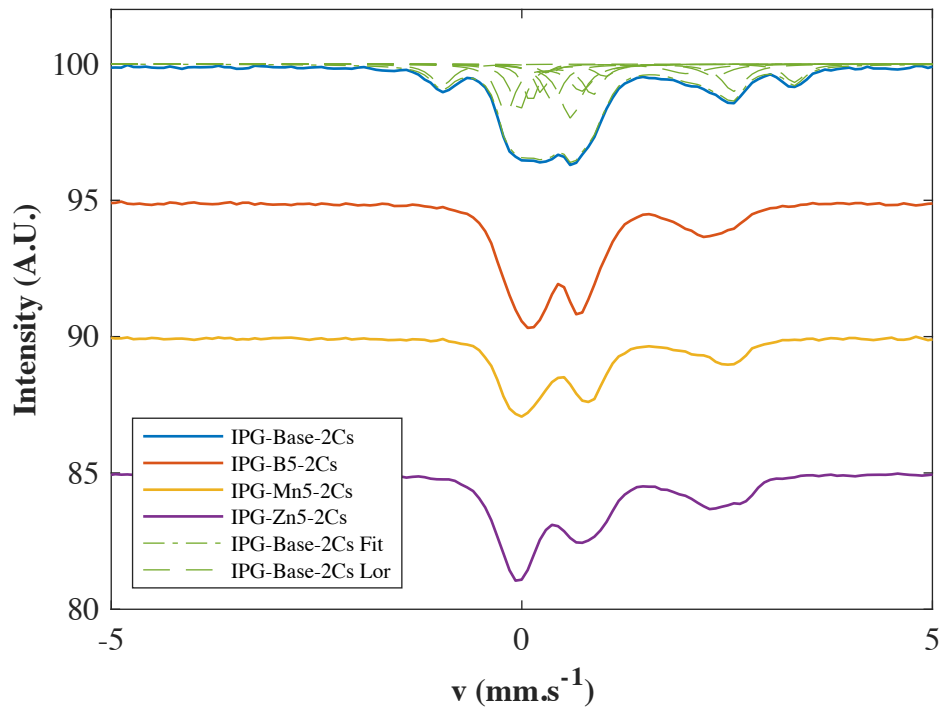


Figure 6.28: Mössbauer spectra of selected caesium doped and an example fit with the Lorentzian components

Figure 6.29 and Figure 6.30 show the quadrupole shift against the isomer shift. It can be seen that the data points for all samples analysed are distributed into two regions, the upper right quadrant and the lower left quadrant. These two regions are associated with Fe^{2+} ions and Fe^{3+} ions respectively as determined by Dyar et al [135]. Fe^{3+} sites have a QS of less than 1.5 mm.s^{-1} and a CS of less than 0.5 mm.s^{-1} . The QS of Fe^{2+} sites range from ~ 2 to 3.5 mm.s^{-1} whilst the CS ranges from $0.9 - 1.4 \text{ mm.s}^{-1}$.

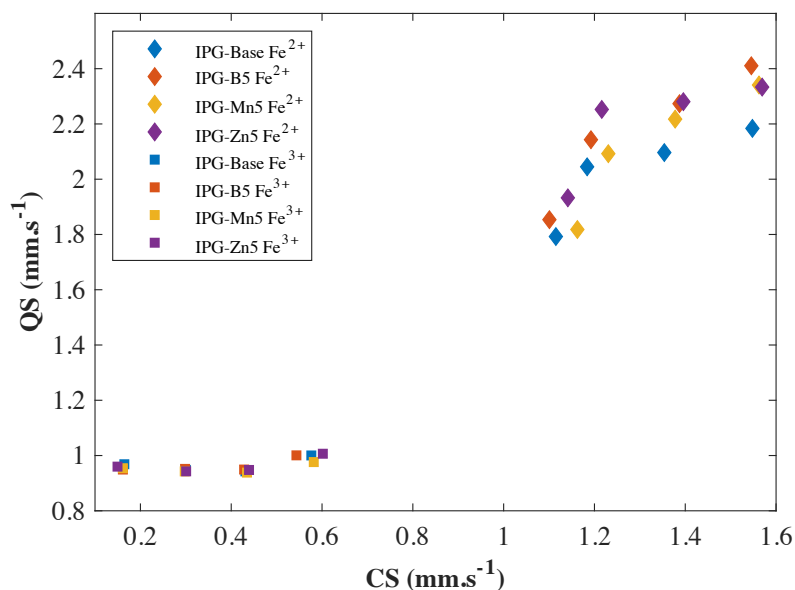


Figure 6.29: Quadrupole splitting against isomer shift values for selected base samples

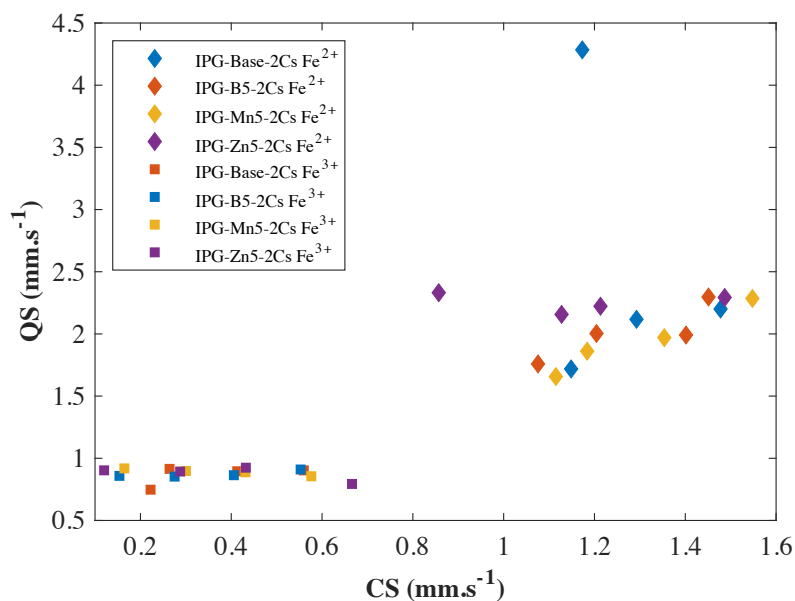


Figure 6.30: Quadrupole splitting against isomer shift values for selected caesium doped samples

Table 6.2: Mössbauer spectroscopy parameters for selected samples

	IPG-Base	IPG-Base-2Cs	IPG-B5	IPG-B5-2Cs	IPG-Mn5	IPG-Mn5-2Cs	IPG-Zn5	IPG-Zn5-2Cs
Fe²⁺/ΣFe %	44	53	45	44	52	41	46	44
Cs (Fe²⁺) mm.s⁻¹	1.3	1.27	1.31	1.28	1.33	1.28	1.33	1.17
QS(Fe²⁺) mm.s⁻¹	2.02	2.58	2.17	2.01	2.12	1.94	2.20	2.25
LW(Fe²⁺) mm.s⁻¹	0.17	0.21	0.18	0.18	0.19	0.18	0.16	0.17
CS(Fe³⁺) mm.s⁻¹	0.37	0.36	0.36	0.35	0.37	0.34	0.37	0.38
QS(Fe³⁺) mm.s⁻¹	0.96	0.87	0.96	0.87	0.95	0.88	0.96	0.88
LW(Fe³⁺) mm.s⁻¹	0.16	0.16	0.15	0.14	0.13	0.14	0.14	0.13

All CS, QS, and LW values shown are averages of the 8 Lorentzian components have an associated error of ± 0.02 , Fe²⁺/ΣFe values have an associated error of ± 1 %

6.8 Compositional Data, Density Measurements and Caesium Retention

Compositional data was obtained using XRF. For the boron series, samples were sent to AMG Superalloys for external analysis. Table 6.3 shows the compositional data for the IPG-Base glass and the IPG-B series. Table 6.4 shows the compositional information for the IPG-Mn series and Table 6.5 shows the compositional information for the IPG-Zn series. Overall, the measured composition of the base glasses matched closely to the target compositions, however, there is an appreciable amount of crucible material (Al_2O_3 and SiO_2) present in all compositions, indicative of the corrosive nature of the melts. The density of each sample was determined using an Archimedes balance and the results are shown at the bottom of each table. It was observed that the density change in the IPG-B series when caesium was added is negligible, whereas there is a significant density increase in the IPG-Mn and IPG-Zn series when caesium is introduced. Composition does not seem to have a direct influence on caesium volatility, as can be seen in Figure 6.31, showing the caesium retention against additive concentration.

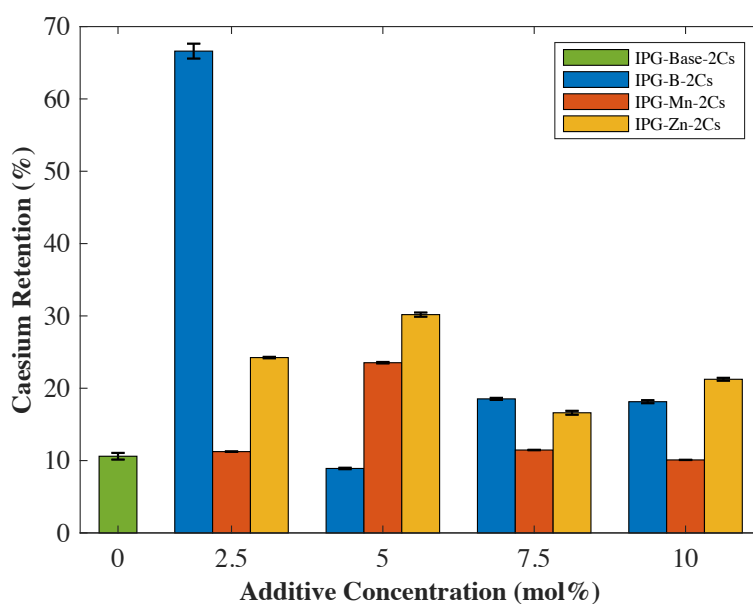


Figure 6.31: Caesium retention vs. additive concentration

Table 6.3: Compositional Data for IPG-Base and IPG-B Series

Sample ID	Target Composition (Measured Composition)						Cs Retention %	Density (s.d) g.cm ⁻³
	mol%							
	Fe ₂ O ₃	P ₂ O ₅	B ₂ O ₃	Al ₂ O ₃	SiO ₂	Cs ₂ O		
Base	40	60	-	-	-	-	-	2.967
	(41.25)	(54.97)		(1.5)	(2.28)			(0.105)
B2.5	37.5	60	2.5	-	-	-	-	2.979
	(36.13)	(57.85)	(2.67)	(0.8)	(2.54)			(0.038)
B5	35	60	5	-	-	-	-	2.987
	(33.67)	(58.62)	(5.14)	(0.74)	(1.84)			(0.003)
B7.5	32.5	60	7.5	-	-	-	-	2.935
	(31.40)	(58.52)	(7.95)	(0.70)	(1.43)			(0.004)
B10	30	60	10	-	-	-	-	2.917
	(29.53)	(58.93)	(10.03)	(0.55)	(0.97)			(0.003)
Base-2Cs	40.8	54.37	-	1.48	2.3	1.05	10.47	2.865
	(39.71)	(57.72)		(1.06)	(1.39)	(0.11)		(0.027)
B2.5-2Cs	35.71	57.16	2.64	0.96	2.5	1.03	66.61	2.903
	(38.89)	(55.59)	(2.8)	(0.67)	(1.37)	(0.69)		(0.014)
B5-2Cs	33.29	57.93	5.08	0.87	1.82	1.02	8.91	2.981
	(35.76)	(56.37)	(5.71)	(0.67)	(1.40)	(0.09)		(0.009)
B7.5-2Cs	31.04	57.83	7.87	0.84	1.42	1.01	18.53	2.785
	(33.29)	(56.56)	(7.88)	(0.62)	(1.45)	(0.19)		(0.005)
B10-2Cs	29.20	58.27	9.92	0.65	0.97	1.00	18.14	2.963
	(32.28)	(54.84)	(10.69)	(0.61)	(1.41)	(0.18)		(0.008)

Table 6.4: Compositional Data for IPG-Mn Series

Sample ID	Target Composition (Measured Composition) mol%						Cs Retention %	Density (s.d) g.cm ⁻³
	Fe ₂ O ₃	P ₂ O ₅	MnO	Al ₂ O ₃	SiO ₂	Cs ₂ O		
Mn2.5	37.5 (40.19)	60 (54.78)	2.5 (2.59)	- (0.79)	- (1.65)	-	-	2.643 (0.050)
Mn5	35 (35.92)	60 (56.98)	5 (3.37)	- (1.58)	- (2.14)	-	-	2.678 (0.048)
Mn7.5	32.5 (32.84)	60 (58.67)	7.5 (6.04)	- (0.76)	- (1.68)	-	-	2.57 (0.057)
Mn10	30 (30.66)	60 (58.16)	10 (8.08)	- (1.19)	- (1.92)	-	-	2.836 (0.181)
Mn2.5-2Cs	39.76 (37.95)	54.21 (57.34)	2.56 (2.03)	0.78 (0.81)	1.64 (1.76)	1.04 (0.12)	11.24	2.949 (0.015)
Mn5-2Cs	35.56 (35.92)	56.4 (56.45)	3.34 (4.1)	1.54 (1.06)	2.13 (2.23)	1.03 (0.24)	23.53	3.039 (0.032)
Mn7.5-2Cs	32.51 (37.95)	58.08 (57.34)	5.98 (2.03)	0.75 (0.81)	1.66 (1.76)	1.02 (0.12)	11.46	3.04 (0.021)
Mn10-2Cs	30.25 (31.38)	57.58 (56.82)	8 (8.53)	1.18 (1.02)	1.9 (2.15)	1 (0.1)	10.09	3.005 (0.013)

Table 6.5: Compositional Data for IPG-Zn Series

Sample ID	Target Composition (Measured Composition)						Cs Retention %	Density (s.d) g.m^{-3}
	mol%							
	Fe_2O_3	P_2O_5	ZnO	Al_2O_3	SiO_2	Cs_2O		
Zn2.5	37.5 (40.36)	60 (54.31)	2.5 (2.66)	- (0.94)	- (1.73)	-	-	2.76 (0.009)
Zn5	35 (35.88)	60 (57.69)	5 (4.81)	- (0.59)	- (1.03)	-	-	2.647 (0.013)
Zn7.5	32.5 (34.94)	60 (54.48)	7.5 (8.25)	- (0.92)	- (1.42)	-	-	2.647 (0.103)
Zn10	30 (32.27)	60 (54.58)	10 (10.86)	- (0.74)	- (1.53)	-	-	2.589 (0.030)
Zn2.5-2Cs	39.9 (36.58)	53.7 (57.81)	2.63 (1.51)	0.93 (1.51)	1.71 (3.83)	1.13 (0.27)	23.89	2.983 (0.015)
Zn5-2Cs	35.51 (35.60)	57.1 (56.44)	4.76 (4.91)	0.59 (0.84)	1.02 (1.90)	1.04 (0.31)	30.18	3.019 (0.026)
Zn7.5-2Cs	34.58 (42.88)	53.92 (45.45)	8.17 (9.46)	0.91 (1.36)	1.41 (1.36)	1.02 (0.17)	16.61	3.043 (0.007)
Zn10-2Cs	31.95 (30.24)	54.04 (57.64)	10.76 (9.52)	0.73 (0.71)	1.52 (1.67)	1 (0.21)	21.24	3.036 (0.003)

6.9 SEM

SEM was used to investigate crystallisation within the samples. SEM-EDX was used to determine the homogeneity of the base glasses, with the results (not shown) suggesting all glasses were single phase. Figure 6.32 and Figure 6.35 show examples of crystalline features observed in the caesium doped samples, with a common crystalline pattern typical of all the caesium doped glasses that crystallised. A needle like crystalline feature can be observed spanning with width of a void in Figure 6.32.

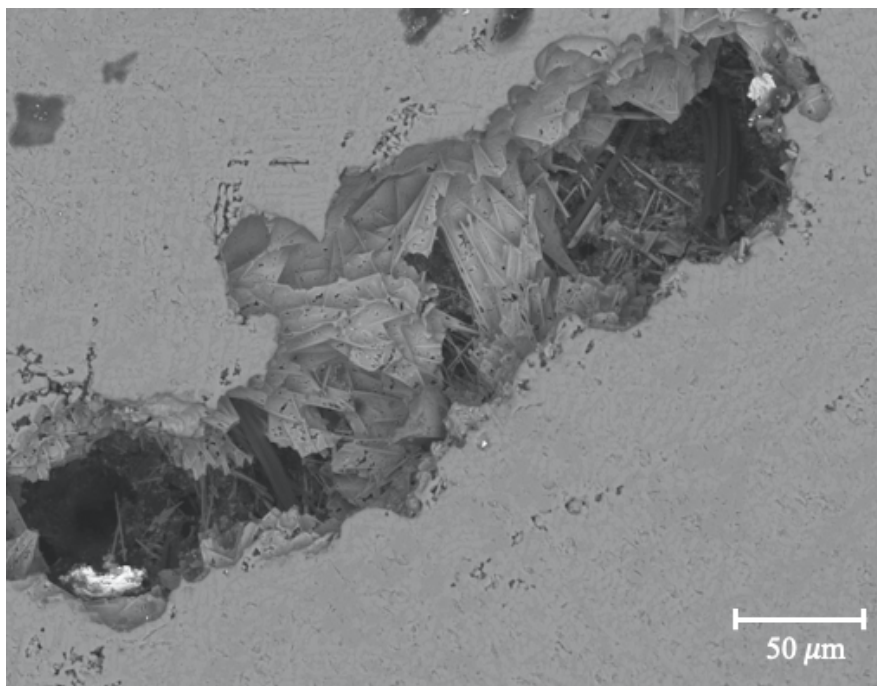


Figure 6.32: Entrenched crystalline phase observed in IPG-B2.5-2Cs sample

BSE image, x500 magnification

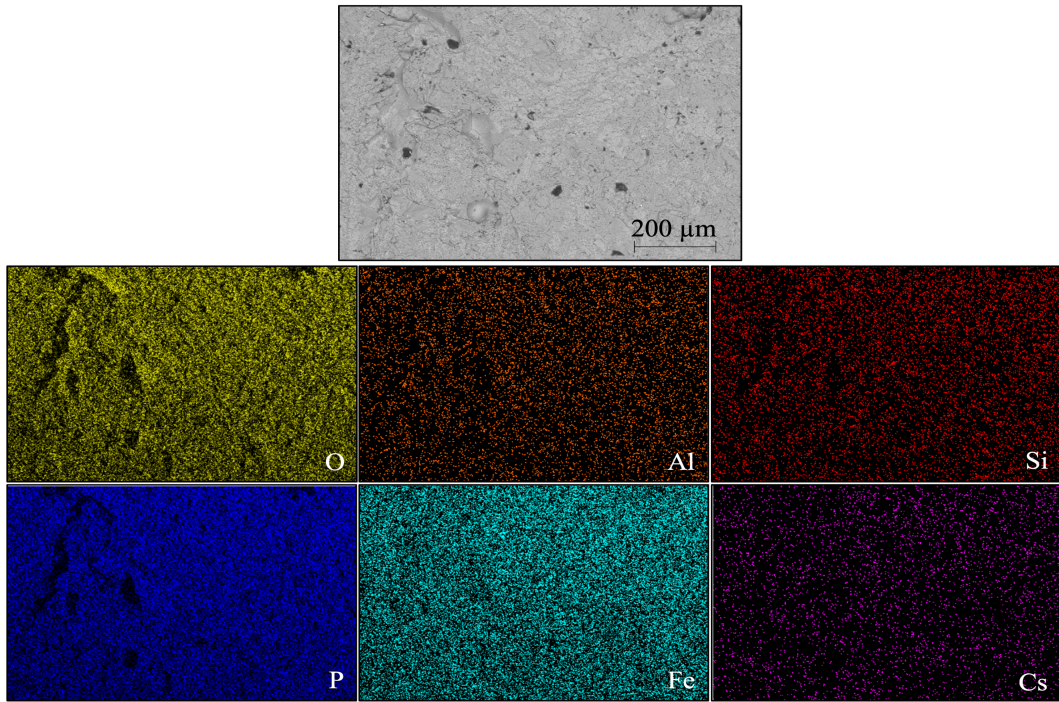


Figure 6.33: SEM-EDX elemental mapping of IPG-Base-2Cs sample

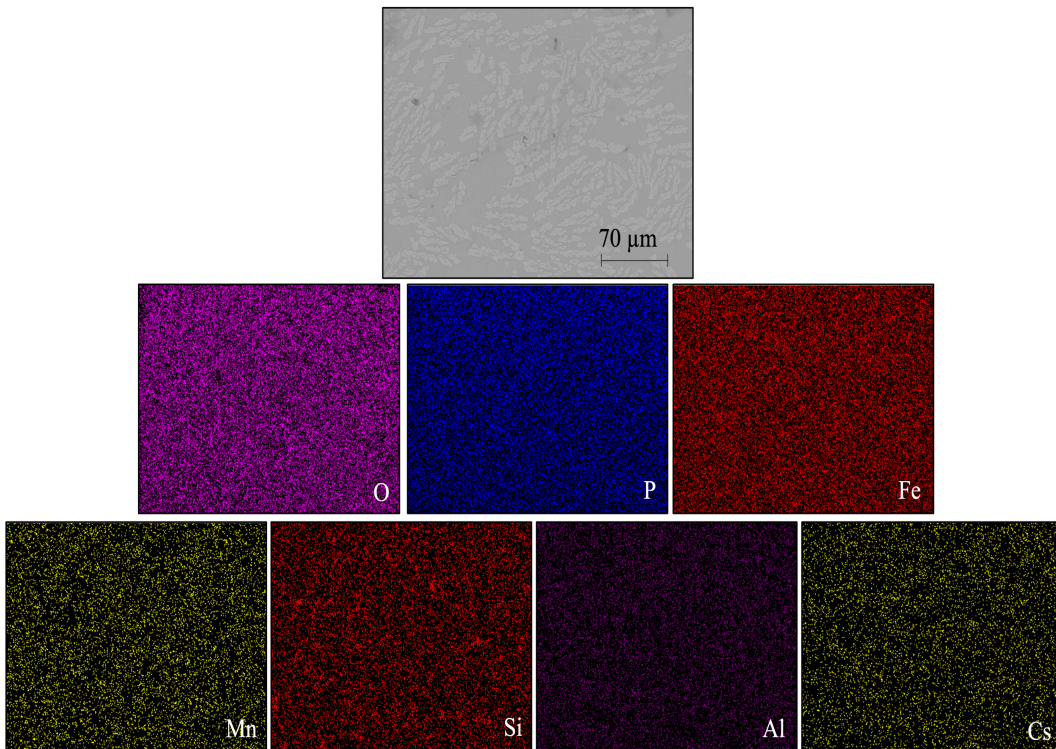
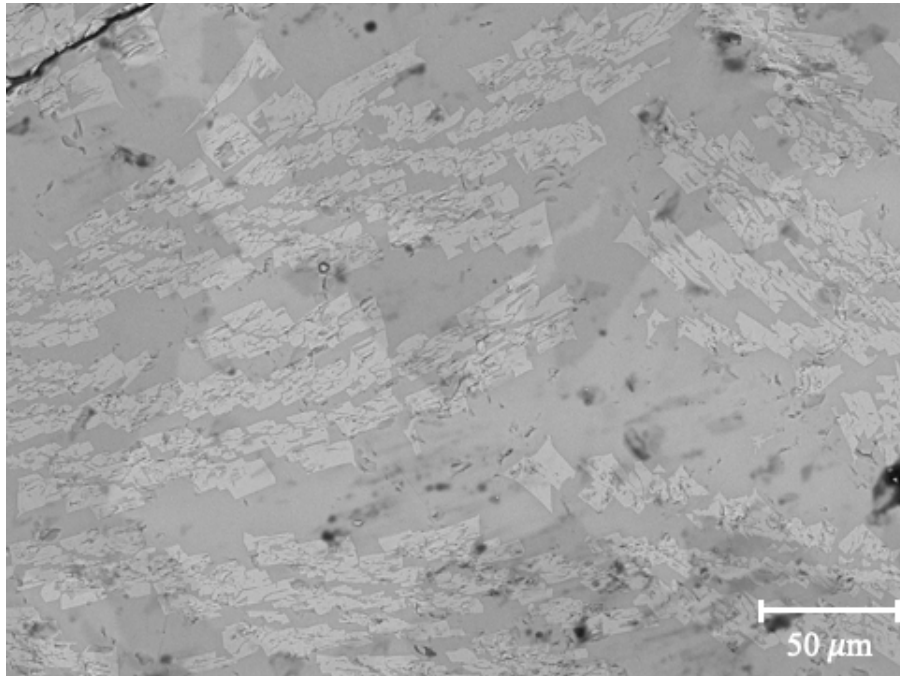


Figure 6.34: SEM-EDX elemental mapping of IPG-Mn5-2Cs sample

Figure 6.33 and Figure 6.34 show elemental maps acquired using SEM-EDX of selected crystalline samples. There are no obvious indications of any element favouring a particular phase in either, an observation that is consistent with all the samples presented.



*Figure 6.35: Crystalline phase observed in IPG-Zn_{2.5}-2Cs sample
BSE image, x500 magnification*

6.10 Discussion

After the caesium doped remelt, the IPG-Base glass crystallised to form $\text{Fe}_2^{3+}\text{Fe}^{2+}(\text{P}_2\text{O}_7)_2$ as can be seen in Figure 6.5. SEM imaging of the IPG-Base-2Cs samples clearly shows a crystalline phase embedded in the remaining glass phase, an observation that can be seen in all samples that crystallised after the caesium doped remelt (see Section 6.9). Furthermore, SEM-EDX analysis does not show any preferential segregation to either the glass or crystalline phase by any element indicating that the composition of the crystalline phase is extremely similar to the glass phase. Thermal analysis of the base glass showed two crystallisation events between 600 – 900 °C, which have been assigned as $\text{Fe}_3(\text{P}_2\text{O}_7)_2$ and $\text{Fe}_4(\text{P}_2\text{O}_7)_3$ by Marasinghe et al. and are in good agreement with the phase assignment of the XRD patterns seen in Section 6.2 [73]. Mössbauer spectroscopy of the IPG-Base and the IPG-Base-2Cs samples show that the fraction of Fe^{2+} increases from 44 % to 53 % when caesium is added (see Table 6.2). Yu et al. noted that the concentration of Fe^{2+} in IPGs is sensitive to the reagents used to produce the glass. In particular, ammonium dihydrogen phosphate (DAP), which was used as a reagent in this study, creates a reducing environment, reducing Fe^{3+} ions to Fe^{2+} ions [77]. Furthermore, glasses with a higher proportion of Fe^{2+} have been shown to be more susceptible to crystallisation, particularly when the fraction of Fe^{2+} is more than 40% [73], [76]. The use of DAP could explain the high proportion of Fe^{2+} in the IPG-Base sample (Fe^{2+} concentrations are typically around 20 % [76]). Mössbauer results of caesium doped iron phosphate studied by Karabulut et al. show that Cs_2O increases the proportion of Fe^{2+} in the glass. Karabulut et al. showed that Fe^{2+} concentrations increased from 19 % in the $40\text{Fe}_2\text{O}_3\text{-}60\text{P}_2\text{O}_5$ base glass to between 32 and 34 % when 5 - 15.6 mol% of Cs_2O was added. Karabulut produced the glasses with the Fe^{2+} concentrations stated above at 1250 °C (with a 2 hour melt duration) and with temperature having a reducing effect, this may explain the disparity between the Fe^{2+} concentrations of Karabulut et al. and the results presented in Section 6.7, where the glasses were melted at 1150 °C for 3 hours, then a further 3 hours at 950 °C following a caesium addition [75]. Caesium retention in base glass was approximately 10 %, considerably lower than literature values [66], [137].

The characterisation of the IPG-Base glass and IPG-B series show good agreement with that of Bingham et. al in terms of T_g , density and Mössbauer parameters (despite some differences in overall Fe^{2+} concentrations) [85], [111]. DTA obtained by Bingham et al. on compositions closely resembling IPG-B5 ($37\text{Fe}_2\text{O}_3\text{-}58\text{P}_2\text{O}_5\text{-}5\text{B}_2\text{O}_3$) and IPG-B10 ($36\text{Fe}_2\text{O}_3\text{-}54\text{P}_2\text{O}_5\text{-}10\text{B}_2\text{O}_3$) show crystallisation events between ~750 – 900 °C. Karabulut et al. also conducted thermal

analysis on a glass with the same target composition as IPG-B10 and found similar crystallisation events to those seen by Bingham et al. [72]. These events are also seen in the DTA presented in Section 6.3. Bingham et al. state that the increased basicity of the glass due to B_2O_3 influences the iron redox environment, promoting the formation of Fe^{2+} [72]. Therefore, the crystallisation observed in the IPG-B-2Cs series could be due to several factors, including boron and caesium promoting Fe^{2+} formation, which as previously discussed is one of the main influences on the stability of these glass types [73], [76].

XRD of the caesium doped samples showed that all of the IPG-B series crystallised after the caesium doped remelts, with the crystal phase produced varying with the boron concentration (see Section 6.2). IPG-B2.5-2Cs crystallised to form the same crystal phase identified in the IPG-Base-2Cs sample, $Fe_3(P_2O_7)_2$. At 5 and 7.5 mol% B_2O_3 , an iron phosphate phase ($FePO_4$) and a boron iron phosphate phase ($B_{0.57}Fe_{0.43}PO_4$) were identified. Finally, IPG-B10-2Cs formed a borophosphate phase BPO_4 suggesting B_2O_3 is potentially playing a larger role in network formation at higher concentrations. The formation of BPO_4 could be indicative of B–O–P bonding as predicted by Hoppe [27]. Raman spectroscopy of the IPG-B series showed the same trend seen in the Mn and Zn series, with a decrease in Q^1 species and an increase in Q^0 and Q^2 with increasing additive concentration, which again indicates a rearrangement of the phosphate network. Kim et al. also observed increasing depolymerisation with increasing B_2O_3 concentrations when studying sodium borophosphate series ($xB_2O_3-(60-x)P_2O_5-40Na_2O$, where $x = 10 - 40$ mol%), attributing the depolymerisation to the incorporation of BO_4 and BO_3 structural units [138]. Kim et al. note that the BPO_4 structure is composed of PO_4 and BO_4 tetrahedra and suggest that a network is formed between these units via B–O–P bonds.

The IPG-Mn and IPG-Zn series show several similarities both before and after the caesium doped remelt. From thermal analysis, both additives reduce the glass transition temperature in comparison to IPG-Base as can be seen in Table 6.1, however zinc appears to have a greater influence than manganese, with the T_g of IPG-Zn10 sample reduced by 13 °C in comparison to the base glass. Structurally, the Q-speciation trends in both series are closely matched and the effect of additive concentration is the same, with increasing additive concentration promoting the formation of Q^2 species, as can be seen in Figure 6.26. The exception to this trend is the IPG-Zn10 sample, where Q^0 and Q^2 levels are significantly lower than the rest of the IPG-Zn series. Iron phosphate compositions are noted in the literature to contain a highly depolymerised phosphate network, shown here by the high Q^1 fractions in all compositions [73], [139], [140]. A comparison of the Raman spectra of the base and caesium doped samples

shows no evidence of significant structural changes after the caesium doped remelt, as evidenced by the comparison of the spectra in Figure 6.22 and Figure 6.23 and the residual difference between the spectra shown in Figure 6.24. However, it was observed that all glasses in the IPG-Mn and IPG-Zn series show a significant increase in density after the caesium doped remelt, with the manganese series increasing from around 2.6 g.cm^{-3} to around 3 g.cm^{-3} after the remelt as can be seen in Table 6.4. The IPG-Zn series sees a similar increase as can be seen in Table 6.5. The density values of the base glasses were low compared to literature values, whilst the increased density of the caesium doped samples are in closer agreement with the literature values [141]. Samples that do not show a significant increase (in some cases there is a decrease) of SiO_2 and Al_2O_3 after the caesium doped remelt see a larger increase in density on average, compared to samples that clearly continue to attack the crucible material. The decrease in density observed in the IPG-Zn series is also explained by Reis et al [141]. Whilst studying zinc doped IPGs, Reis et al. suggest that the substitution of Fe ions with Zn ions decreased the number of cross linkages in the network, lowering the density [141]. Both the MnO and ZnO 2.5 mol% and 5 mol% samples crystallised after the caesium doped remelts, all forming similar iron phosphate phases ($\text{Fe}_3(\text{P}_2\text{O}_7)_2$ and $\text{Fe}_7(\text{P}_2\text{O}_7)_4$). The 7.5 mol% and 10 mol% samples all remained amorphous in the IPG-Mn and IPG-Zn series. Both the IPG-Mn and IPG-Zn series show increasing thermal stability with increasing additive concentration, with the first crystallisation event moving to higher temperatures and T_g remaining around 501 - 512 °C. Additionally, the corresponding melting events move to lower temperatures, which helps to explain why these systems remained amorphous at increasing additive concentrations. Mössbauer spectroscopy revealed that the IPG-Mn5 sample had a 9% increase in Fe^{3+} as the caesium doped remelt, whilst the IPG-Zn5 sample showed a slight decrease in Fe^{3+} as seen in Section 6.7. Therefore, it is not as immediately clear if caesium additions have caused the crystallisation through Fe^{2+} formation, as was the case in the IPG-B series. Despite the similarity in structure, the IPG-Zn series outperformed the IPG-Mn (and IPG-B) series in terms of caesium retention, with all IPG-Zn samples improving caesium retention by at least 50% in comparison to IPG-Base-2Cs.

Comparing all of the caesium retention rates of all the glasses investigated, there is no clear trend linking glass composition to caesium retention as can be seen in Figure 6.31. It can be said that ZnO additions suppress caesium volatility, with all IPG-Zn retention rates at least doubling that of IPG-Base-2Cs. The caesium retentions of the IPG-B and IPG-Mn series glasses fluctuate but in general they do not perform any better than IPG-Base-2Cs. All caesium

retention rates presented here are far lower than those reported in the literature for similar glass types [66], [137]. However, the thermal conditions experienced by the samples in this work most likely exaggerate the volatility as the samples remain at temperatures high enough to promote caesium volatility for extended periods of time (approximately 6-7 hours at temperatures above 600 °C). Furthermore, there is a possibility that the nitrogen gas used to purge the system throughout the experiment may have increased the melt turbulence and therefore increased volatility [142]. Finally, it has been demonstrated in earlier sections of this thesis (Section 3.4) that there is not always good agreement between literature sources when it comes to the measurement of volatile species in glass production, such as the large variations in SO₃ retention rates reported by Kim et al. (45%), Bingham et al. (1%), and Day et al. (85%), although the available data are impacted by variables such as glass composition [66]–[68].

6.11 Conclusions

A series of iron phosphate glasses with B₂O₃, MnO and ZnO additions were melted at 950 °C for 3 hours with a target of 2 wt.% Cs₂O. Caesium volatility was much higher than reports in the literature suggest for these glass types, typically ranging between 70 and 90% [66], [137], which could be melt turbulence caused by nitrogen gas flow or the experimental run time. All glasses with less than 7.5 mol% additive crystallised during the caesium doped remelt. It was initially hypothesised that this was due to the reducing environment of the remelt, however Mössbauer spectroscopy determined that there was no correlation between the iron valance and crystallisation tendency. It is therefore more likely that these glasses exhibit poor thermal stability and would be susceptible to crystallisation under a slow cooling regime, regardless of atmosphere. Raman spectroscopy identified structural similarities between the IPG-Mn and IPG-Zn 7.5 and 10 mol% glasses both before and after caesium doping, showing that the structure of these glasses remain virtually unchanged after the caesium doped remelt. The IPG-B series displayed interesting crystallisation behaviour, forming iron phosphate phases at lower B₂O₃ concentrations, an iron borophosphate phase at 5 and 7.5 mol% B₂O₃ and a borophosphate phase in IPG-B10-2Cs.

7 Sodium Borosilicate Glasses

7.1 Introduction

A series of borosilicate glasses were made following the procedure in Section 4.1. The composition of these glasses are based on the UK's HLW CaZn composition. For this work, the Li_2O content of the CaZn composition was replaced with Na_2O on an equimolar basis to simplify the compositional analysis. Each composition was re-melted 3 times with target Cs_2O concentrations of 2, 5 and 10 wt.% and then reanalysed to observe the caesium loss and any changes to the chemical or physical properties. The total fraction of CaO and ZnO was fixed at 12.5 mol%, with the ratio of Zn:Ca going from 100:0, 80:20, 60:40, 40:60 to 20:80. The nomenclature employed for this glass series is as follows NaBSZnXCaYCsZ , where X, Y represent the Zn:Ca ratio and Z is the target wt.% of Cs_2O . All compositions at a particular caesium loading may be referred to as NaBS-CsX , where X represents the target Cs_2O content. Similarly to Chapter 6, the results presented below are separated by the characterisation technique used and then separated into caesium doped glasses and base glasses.

7.2 XRD

Figure 7.1 - Figure 7.4 show the XRD traces for all of the borosilicate glasses. It can be observed from these results that all the glasses in the series remain amorphous during the caesium doped remelts, regardless of the batched caesium concentration. The small feature observable at approximately $45^\circ 2\theta$ is attributed α -Fe, caused by contamination during sample preparation.

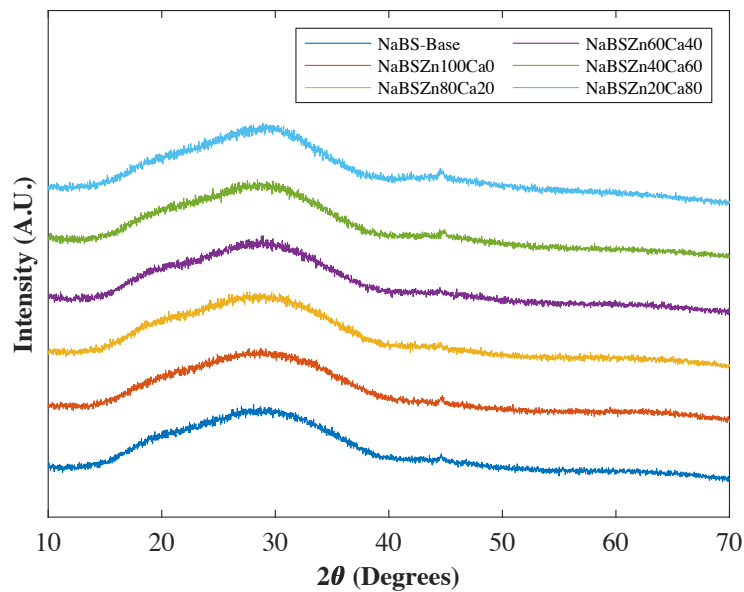


Figure 7.1: XRD patterns of base glass samples

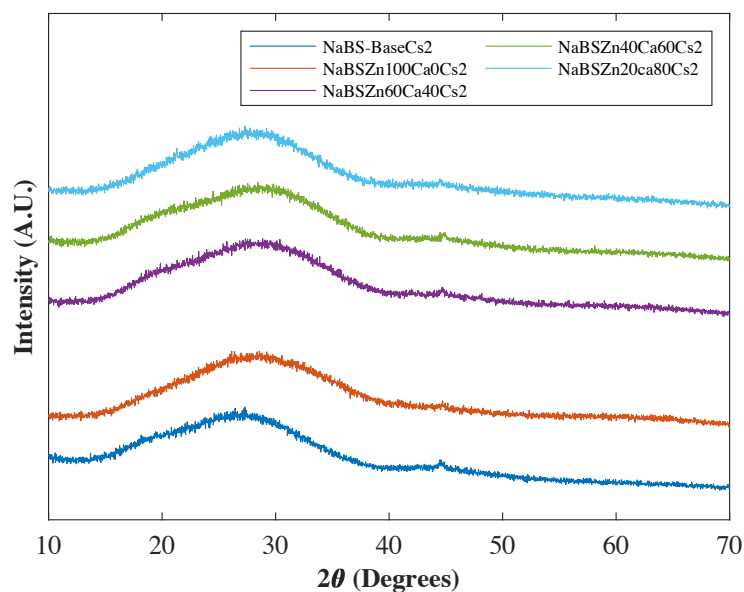


Figure 7.2: XRD patterns of NaBS-Cs2 series

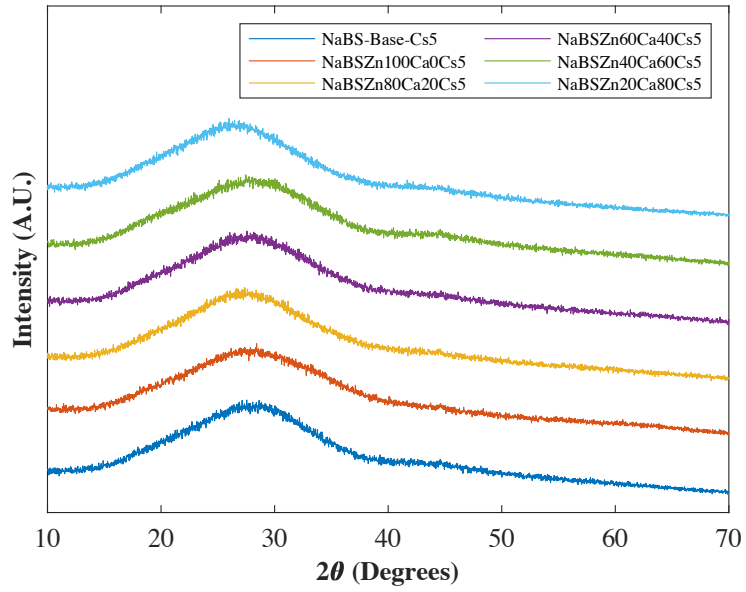


Figure 7.3: XRD patterns of NaBS-Cs5 series

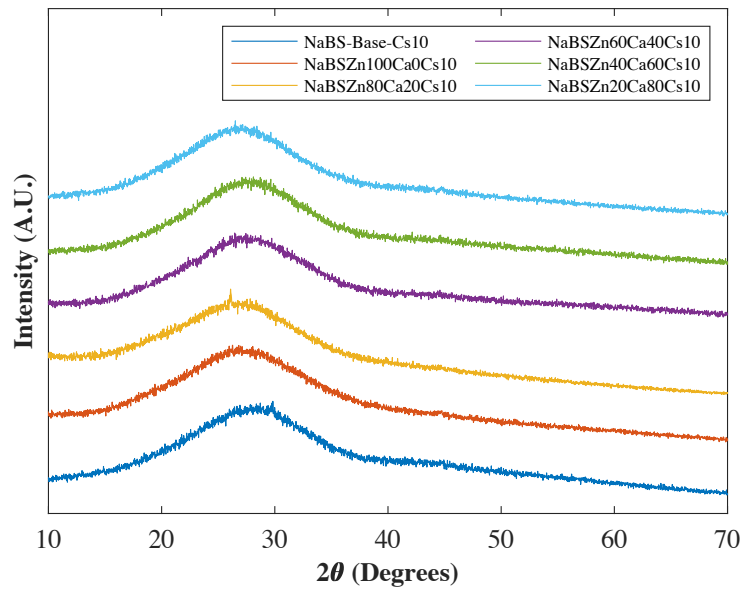


Figure 7.4: XRD patterns of NaBS-Cs10 series

7.3 Thermal Analysis

Thermal cycling of the samples removed any thermal history, the traces shown in Figure 7.5 are the data points from the second heating of the samples. The glass transition temperature of each composition was determined by taking the first derivative of the heat flow data and identifying the points of inflection as can be seen in Figure 7.6.

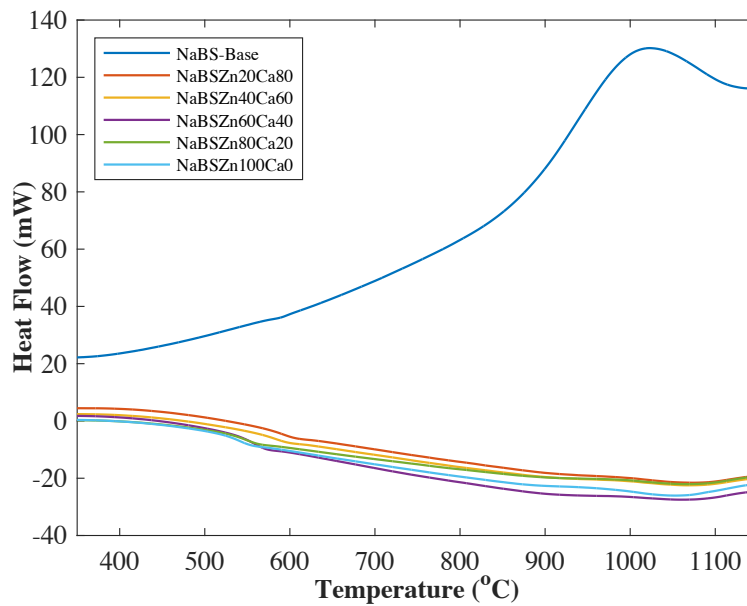


Figure 7.5: DSC traces of NaBS series

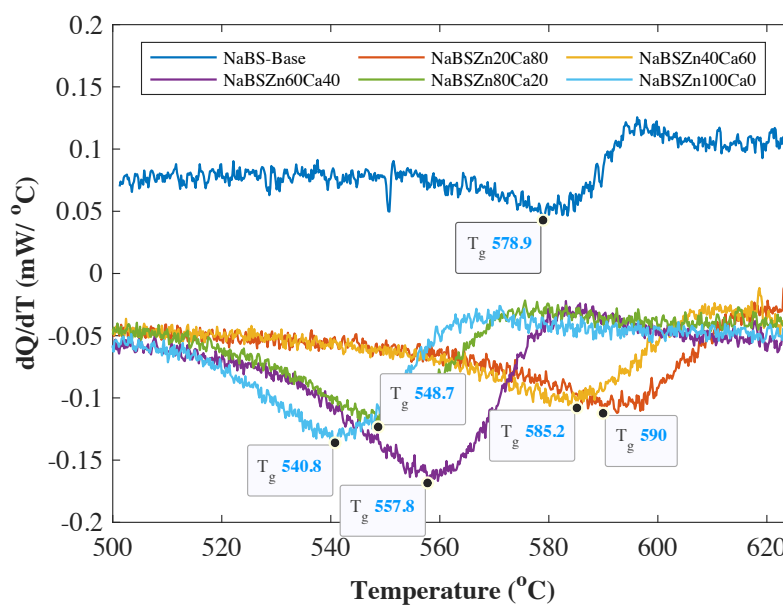


Figure 7.6: First derivative of NaBS heat flow data to determine T_g

The transition temperatures seen in Figure 7.6 and Figure 7.7 are in good agreement with literature values for similar glass compositions [143], [144]. Figure 7.7 shows how the T_g varies with composition, with the initial CaO and ZnO additions causing an increase in T_g at high CaO concentrations, then a sharp reduction in T_g as the ZnO concentration increases.

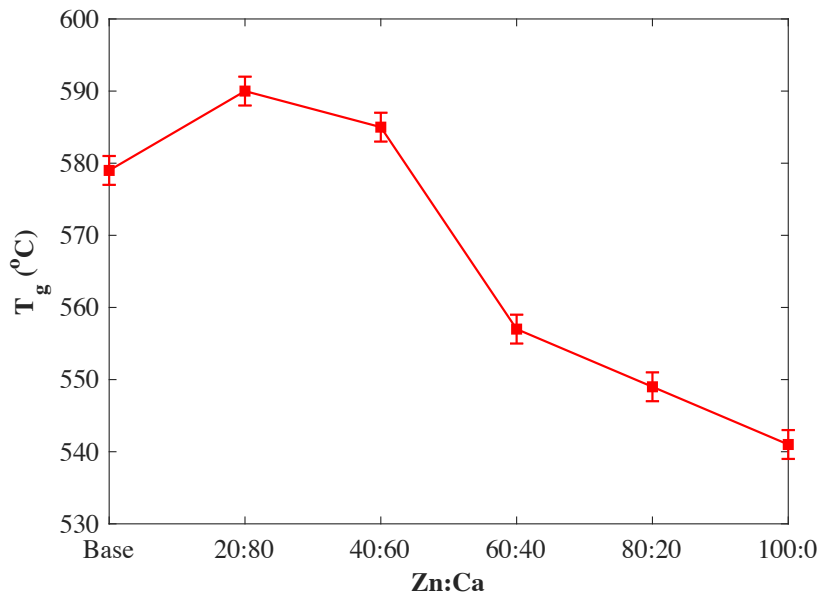


Figure 7.7: T_g variation with ZnO concentration

7.4 Raman Spectroscopy of the bulk glasses

Figure 7.8 - Figure 7.11 show the Raman spectra of all glasses in this series at each Cs_2O waste loading. The main silica band centred at approximately 1060 cm^{-1} is asymmetric, with a notable difference in shape between the NaBS-Base composition and the glasses containing CaO and ZnO. The position of the main silica band can be observed to shift to higher wavenumber with increasing ZnO concentrations. Reedmergnerite (NaBSi_3O_8) and danburite ($\text{CaB}_2(\text{SiO}_4)_2$) like MRO structures are attributed to the peaks at $\sim 500\text{ cm}^{-1}$ and $\sim 625\text{ cm}^{-1}$ respectively. The small shoulder at $\sim 780\text{ cm}^{-1}$ is attributed to BO_4 groups [8].

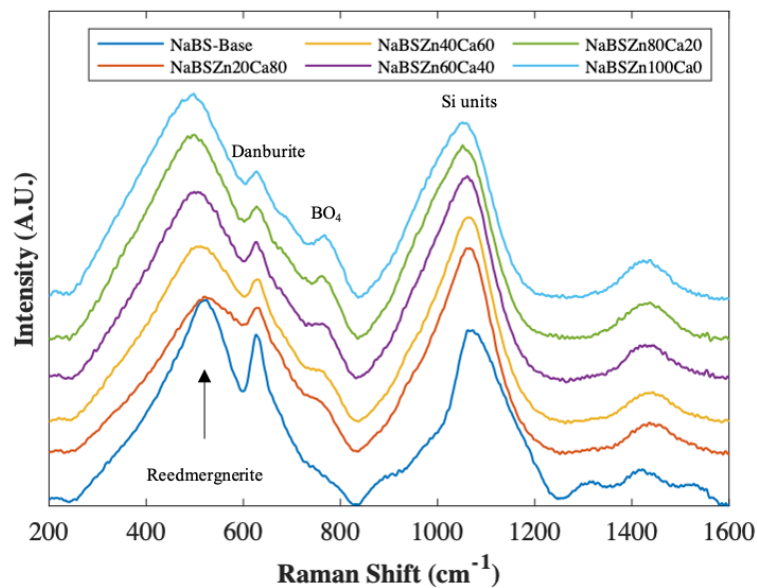


Figure 7.8: Raman Spectra of NaBS base glasses

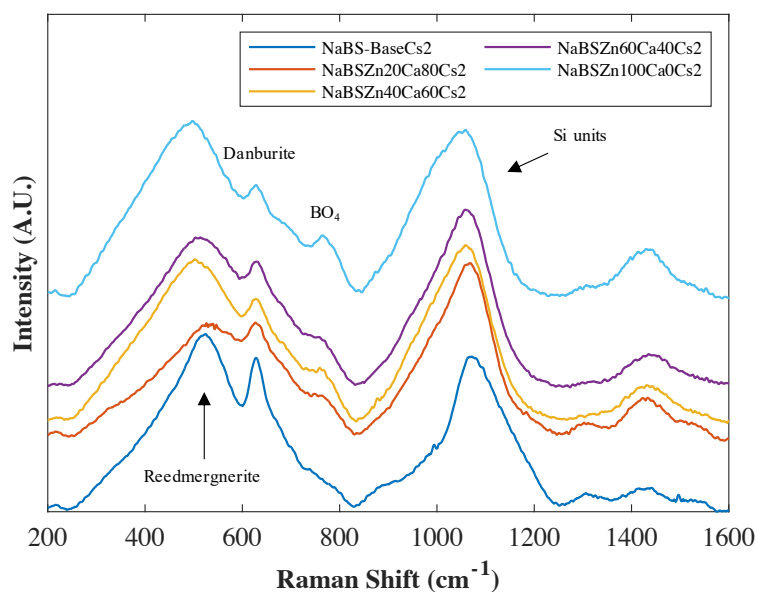


Figure 7.9: Raman Spectra of NaBS-2Cs Series

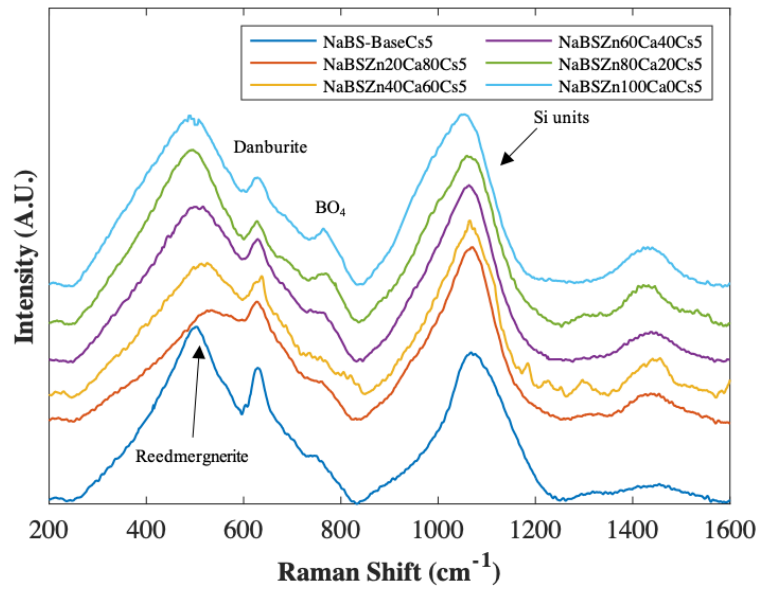


Figure 7.10: Raman Spectra of NaBS-5Cs Series

Figure 7.10 and Figure 7.11 show that even with significant Cs_2O additions, the structural features observed remain similar to the base glasses. The change in shape of the MRO contributions at $\sim 500 \text{ cm}^{-1}$ and $\sim 625 \text{ cm}^{-1}$ can be seen to vary in line with CaO content rather than Cs_2O content.

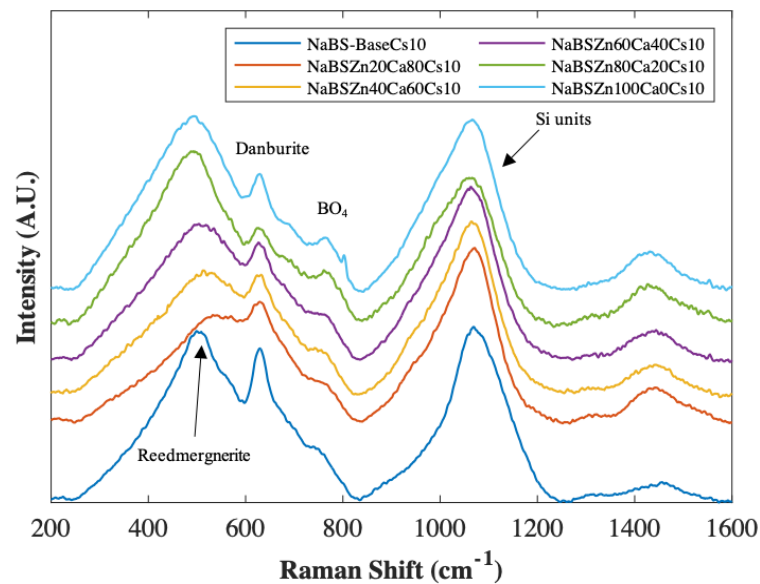


Figure 7.11: Raman Spectra of NaBS-Cs10 Series

Figure 7.12 - Figure 7.15 show the difference in area in the region associated with MRO structures ($200 - 800 \text{ cm}^{-1}$). It can be observed in Figure 7.12 that increased CaO concentrations lead to a decrease in the reedmergnerite peak seen at approximately 500 cm^{-1} in comparison to the NaBS-Base composition. Increasing ZnO content increases the reedmergnerite peak back to a similar intensity seen in the NaBS-Base composition and also sees the emergence of a small peak at approximately 780 cm^{-1} attributed to BO_4 units. In contrast to the trend seen with ZnO concentrations and the reedmergnerite peak, the danburite peak decreases in intensity with increasing ZnO concentrations.

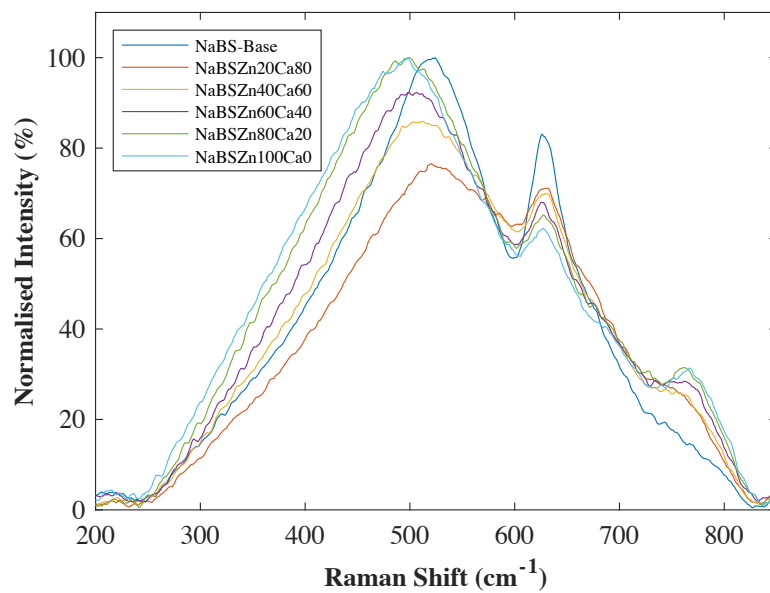


Figure 7.12: A comparison of the MRO region ($200 - 800 \text{ cm}^{-1}$) in the NaBS base glasses

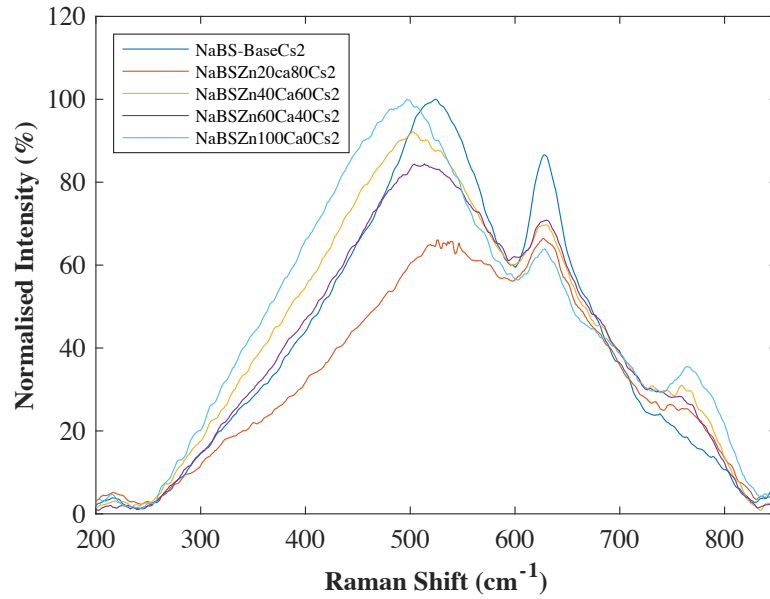


Figure 7.13: A comparison of the MRO region ($200 - 800 \text{ cm}^{-1}$) in the NaBS-Cs2 glasses

Figure 7.13 and Figure 7.14 are comparisons of the MRO region in the NaBS-Cs2 and NaBS-Cs5 series. The same trends observed for the base glasses in Figure 7.12 are also observed in both the NaBS-Cs2 and NaBS-Cs5 series.

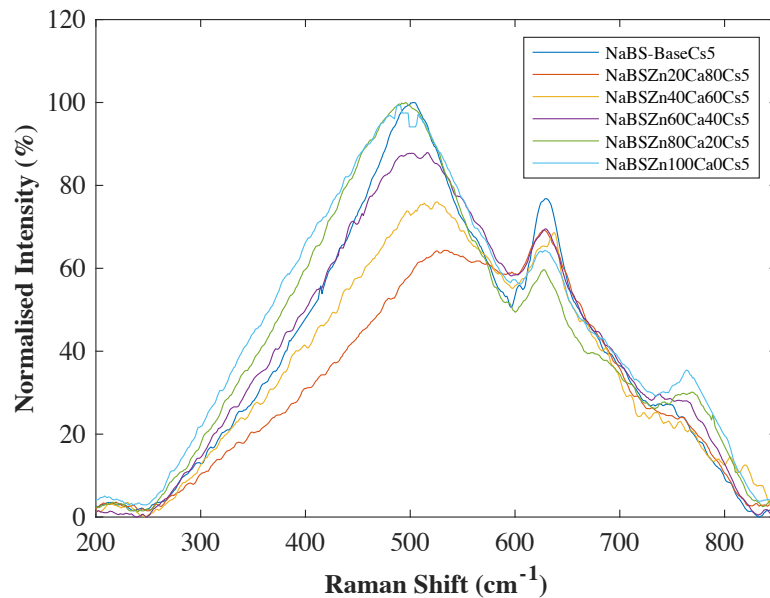


Figure 7.14: A comparison of the MRO region ($200 - 800 \text{ cm}^{-1}$) in the NaBS-Cs5 glasses

Figure 7.15 shows the MRO region comparison for the NaBS-Cs10 series. Again, the trends observed match the base glasses, showing that the extra alkali (Cs_2O) content does not affect the MRO content in NaBS glasses.

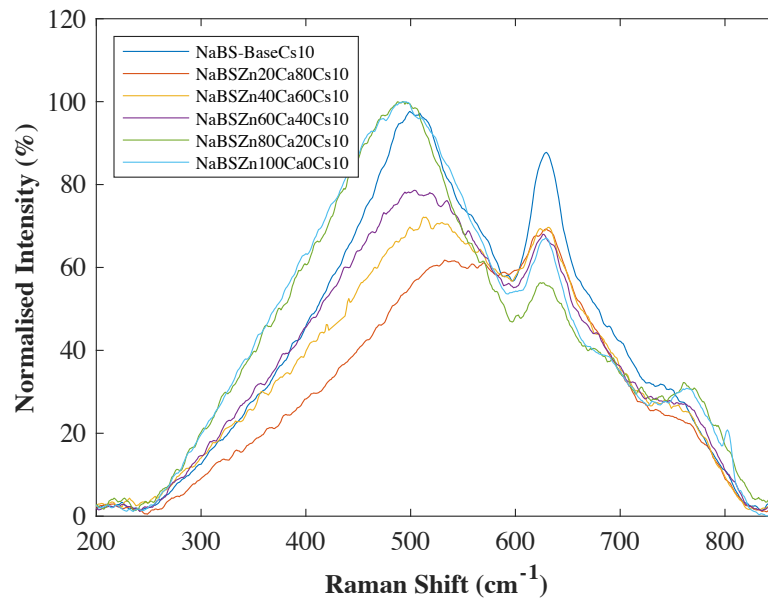


Figure 7.15: A comparison of the MRO region ($200 - 800 \text{ cm}^{-1}$) in the NaBS-Cs10 glasses

7.5 Deconvolution of the main Raman band

The main Raman band seen in all of the base glass spectra is situated between ~ 850 and 1250 cm^{-1} . Four Gaussians were used to approximate the Q-speciation within this region, as per the literature assigned values seen in Table 5.1. A dominant peak at ~ 1060 cm^{-1} was attributed to Q^3 units, with a Q^2 contribution around 925 cm^{-1} and silica units associated with boron $Q^4(\text{B})$ at 970 cm^{-1} and 1150 cm^{-1} . Figure 7.16 shows a typical fit acquired following the procedure described in Section 4.9.3. Figure 7.17 – Figure 7.20 show the results of the deconvolution for all glasses (excluding the erroneous NaBSZn80Ca20Cs2 sample). Q^3 is observed to be the dominant structural group in all glasses in this section. The $Q^4(\text{B})$ contribution at ~ 1150 cm^{-1} is seen to decrease with increasing ZnO content, however the $Q^4(\text{B})$ contribution at ~ 970 cm^{-1} is seen to generally increase with ZnO concentrations. The Q^2 contribution at ~ 925 cm^{-1} fluctuates with composition but remains low in all samples analysed.

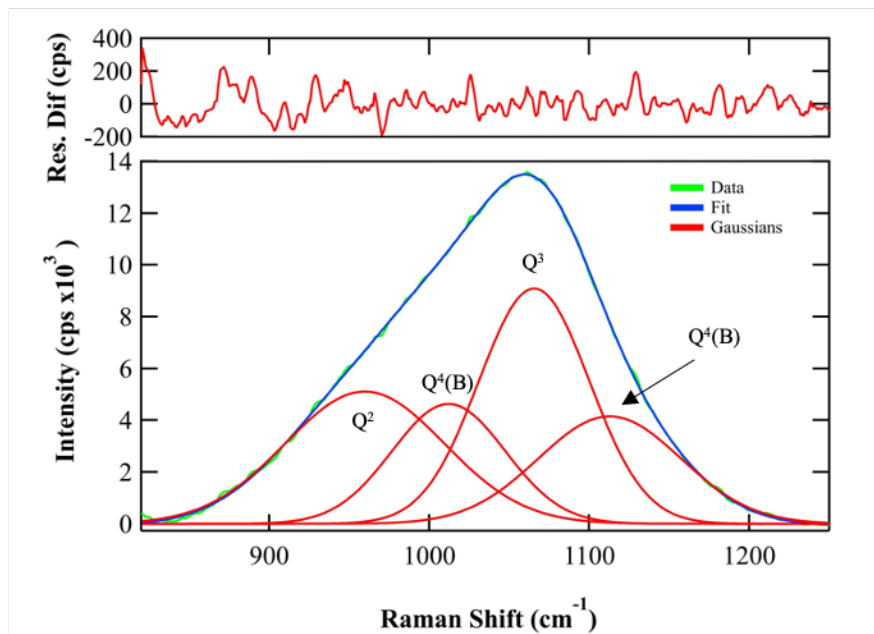


Figure 7.16: An example of a typical deconvolution of NaBS series glass

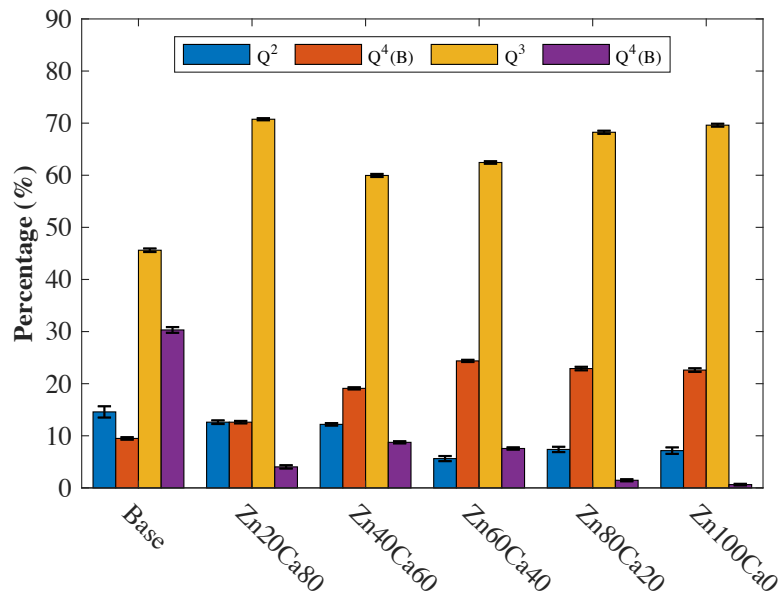


Figure 7.17: Q-speciation of NaBS base glasses

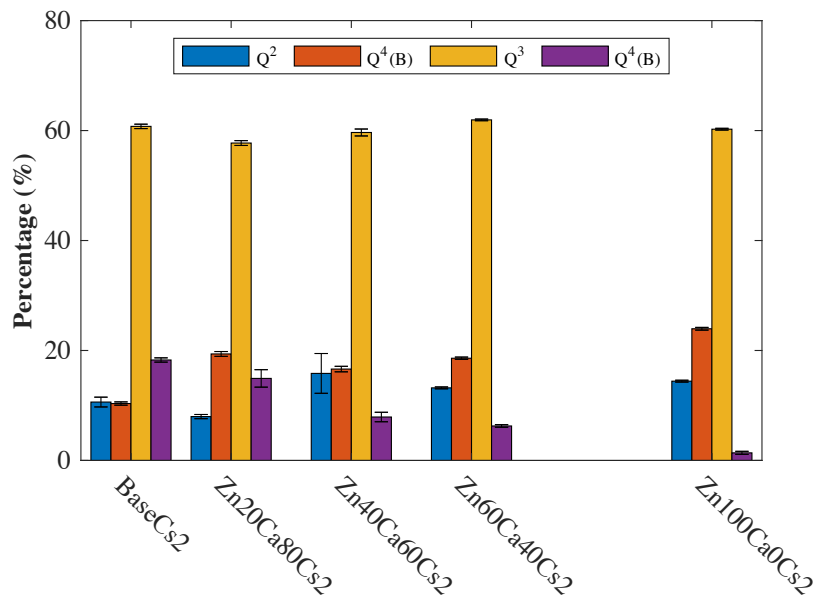


Figure 7.18: Q-speciation of NaBS-Cs₂ glasses

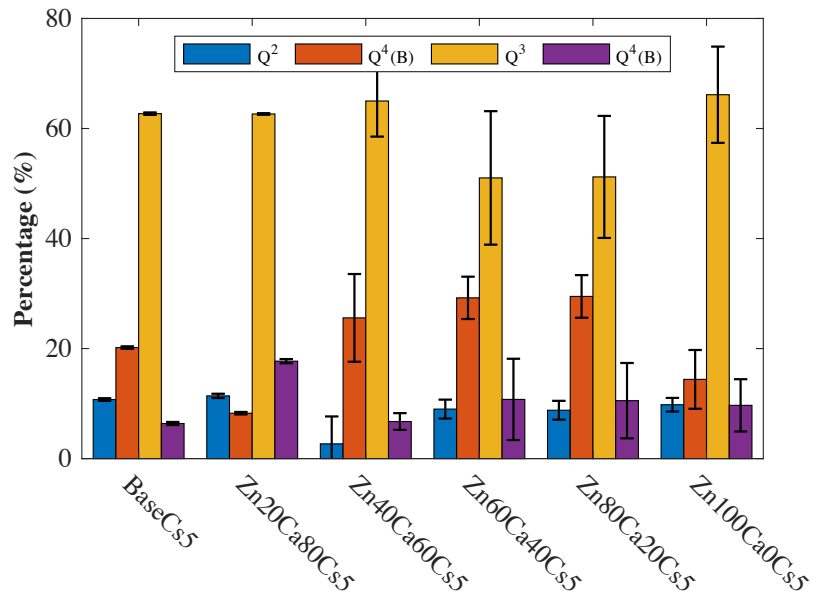


Figure 7.19: Q-speciation of NaBS-Cs5 glasses

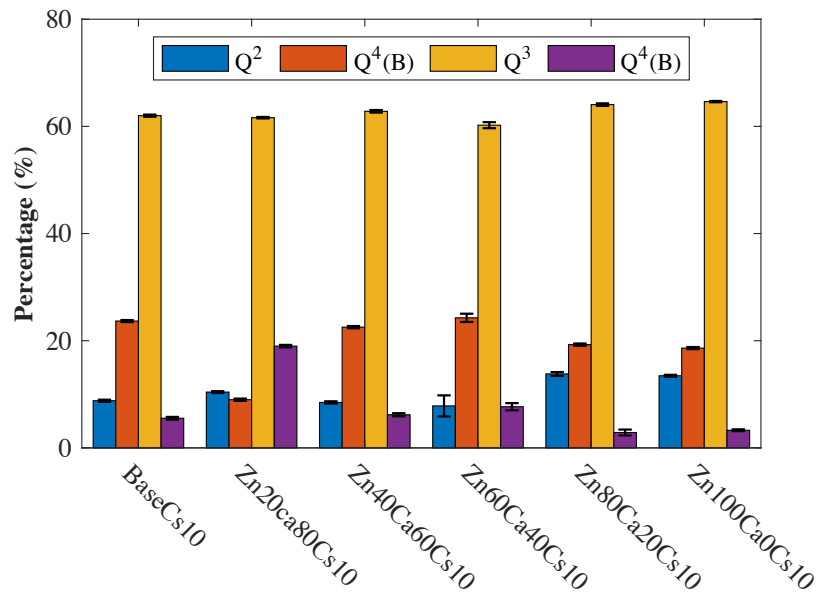


Figure 7.20: Q-speciation of NaBS-Cs10 glasses

7.6 Compositional Analysis and Density Measurements

XRF analysis shows the target and measured compositions to be in reasonable agreement as can be seen in Table 7.1 - Table 7.4. Some variation is seen in the Na₂O and ZnO values, possibly due to unresolved interference between the K_{α} line for Na and the K_{β} line for Zn. Figure 7.21 shows the density variation with glass composition and caesium loadings. A general increase in density is seen with increasing ZnO and Cs₂O concentrations. Figure 7.22 shows the caesium retention rates, calculated as a percentage of the target wt.% and the measured wt.% Cs₂O.

Table 7.1: Compositional data for NaBS base glasses

Sample ID	Target Composition (Measured Composition)						Density (s.d) g.cm ⁻³
	mol%						
	Al ₂ O ₃	B ₂ O ₃	CaO	Na ₂ O	SiO ₂	ZnO	
Base	2.74	17.99	-	20.42	58.84	-	2.523
	(4.03)	(13.68)	-	(16.32)	(65.96)	-	(0.001)
Zn20Ca80	2.40	15.74	10.00	17.87	51.49	2.50	2.610
	(2.72)	(13.61)	(9.40)	(16.28)	(54.04)	(3.95)	(0.010)
Zn40Ca60	2.40	15.74	7.50	17.87	51.49	5.00	2.655
	(2.76)	(13.31)	(7.17)	(16.38)	(56.54)	(3.84)	(0.002)
Zn60Ca40	2.40	15.74	5.00	17.87	51.49	7.50	2.708
	(2.82)	(14.09)	(4.74)	(17.14)	(54.56)	(6.64)	(0.002)
Zn80Ca20	2.40	15.74	2.50	17.87	51.49	10.00	2.744
	(2.79)	(13.91)	(2.69)	(16.65)	(54.45)	(9.50)	(0.004)
Zn100Ca0	2.40	15.74	-	17.87	51.49	12.50	2.658
	(2.82)	(13.69)	-	(17.27)	(54.50)	(11.73)	(0.033)

Table 7.2: Compositional data for NaBS-Cs2 glasses

Sample ID	Target Composition (Measured Composition)							Density (s.d) g.cm ⁻³
	mol%							
	Al ₂ O ₃	B ₂ O ₃	CaO	Na ₂ O	SiO ₂	ZnO	Cs ₂ O	
Base	4.02 (0.00)	13.62 (13.63)	-	16.25 (17.75)	65.66 (68.45)	-	0.46 (0.16)	2.526 (0.003)
Zn20Ca80	2.71 (2.64)	13.55 (12.80)	9.36 (10.82)	16.20 (12.53)	53.80 (57.07)	3.93 (4.01)	0.46 (0.13)	2.691 (0.022)
Zn40Ca60	2.74 (2.95)	13.25 (13.54)	7.14 (7.94)	16.31 (16.07)	56.28 (55.59)	3.82 (3.77)	0.46 (0.13)	2.676 (0.019)
Zn60Ca40	2.81 (2.92)	14.02 (13.71)	4.72 (7.14)	17.06 (14.93)	54.31 (56.67)	6.61 (6.07)	0.46 (0.37)	2.698 (0.009)
Zn80Ca20	2.78	13.85	2.68	16.57	54.20	9.46	0.47	
This data point has been removed due to a labelling error								
Zn100Ca0	2.80 (2.76)	13.62 (11.90)	-	17.19 (15.06)	54.24 (52.65)	11.68 (17.37)	0.47 (0.25)	2.785 (0.004)

Table 7.3: Compositional data for NaBS-Cs5 glasses

Sample ID	Target Composition (Measured Composition)							Density (s.d) g.cm ⁻³
	mol%							
	Al ₂ O ₃	B ₂ O ₃	CaO	Na ₂ O	SiO ₂	ZnO	Cs ₂ O	
Base	3.99 (3.89)	13.52 (15.23)	-	16.13 (18.24)	65.19 (62.13)	-	1.17 (0.51)	2.641 (0.001)
Zn20Ca80	2.69 (2.61)	13.46 (15.57)	9.29 (11.02)	16.09 (11.31)	53.43 (55.89)	3.90 (2.94)	1.13 (0.51)	2.557 (0.002)
Zn40Ca60	2.72 (3.17)	13.16 (11.09)	7.09 (8.22)	16.20 (15.29)	55.90 (56.36)	3.80 (5.13)	1.14 (0.74)	2.668 (0.001)
Zn60Ca40	2.79 (3.26)	13.92 (12.22)	4.69 (5.77)	16.94 (14.68)	53.93 (59.39)	6.57 (4.11)	1.15 (0.56)	2.718 (0.006)
Zn80Ca20	2.76 (3.23)	13.75 (11.17)	2.66 (2.92)	16.45 (16.55)	53.82 (57.14)	9.39 (8.10)	1.16 (0.89)	2.730 (0.002)
Zn100Ca0	2.78 (2.94)	13.53 (13.61)	-	17.07 (13.52)	53.86 (60.12)	11.59 (9.41)	1.17 (0.41)	2.818 (0.008)

Table 7.4: Compositional data for NaBS-Cs10 glasses

Sample ID	Target Composition (Measured Composition)							Density (s.d) g.cm^{-3}
	mol%							
	Al_2O_3	B_2O_3	CaO	Na_2O	SiO_2	ZnO	Cs_2O	
Base	3.94	13.36	-	15.94	64.40	-	2.37	2.585
	(5.51)	(13.08)	-	(14.18)	(65.31)	-	(1.92)	(0.002)
Zn20Ca80	2.66	13.29	9.18	15.89	52.76	3.85	2.43	2.721
	(2.80)	(15.06)	(9.55)	(15.85)	(52.69)	(2.70)	(1.36)	(0.003)
Zn40Ca60	2.69	12.99	7.00	15.99	55.20	3.75	2.37	2.724
	(2.83)	(13.43)	(7.29)	(16.49)	(52.89)	(5.56)	(1.53)	(0.004)
Zn60Ca40	2.76	13.75	4.63	16.73	53.26	6.48	2.39	2.737
	(2.95)	(12.95)	(5.27)	16.52)	(56.80)	(4.33)	(1.18)	(0.007)
Zn80Ca20	2.73	13.57	2.63	16.24	53.13	9.27	2.42	2.760
	(3.25)	(16.02)	(2.65)	(15.90)	(56.17)	(4.97)	(1.03)	(0.001)
Zn100Ca0	2.75	13.35	-	16.85	53.17	11.44	2.44	2.764
	(3.17)	(12.42)	-	(16.64)	(59.74)	(6.92)	(1.12)	(0.002)

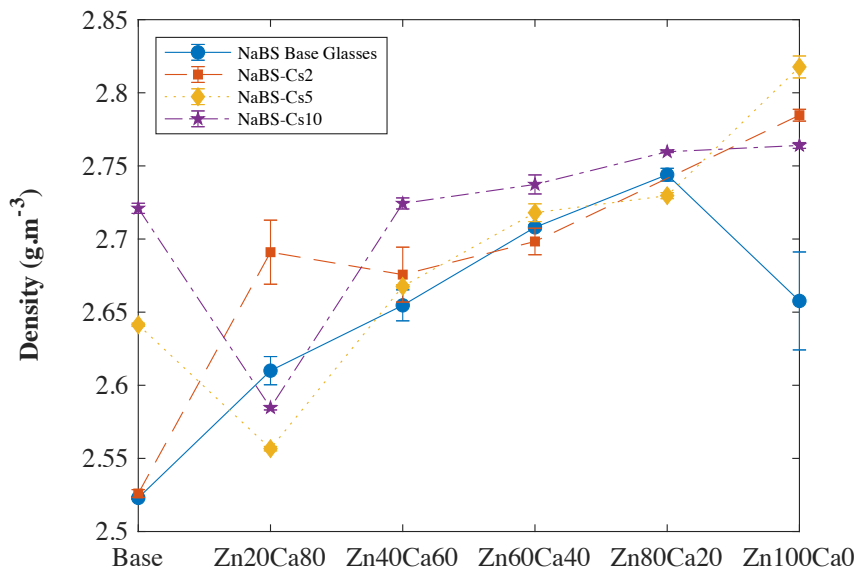


Figure 7.21: Density comparison of all NaBS glasses

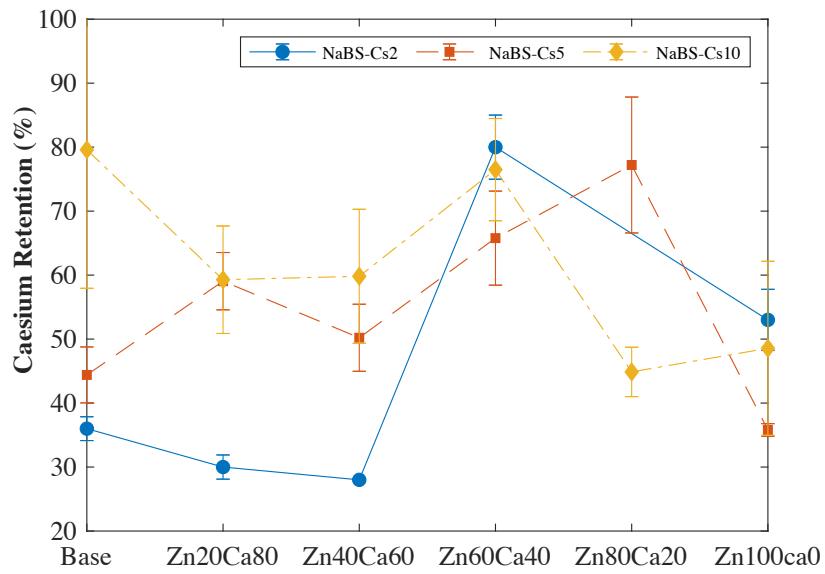


Figure 7.22: Caesium retention in NaBS glass series

Figure 7.22 shows the caesium retention at all three loadings. It can be seen that for NaBS-base and batched Zn:Ca ratios below Zn60Ca40, the retention rate generally increases as the batched caesium content increases, however beyond this point, the reverse is true and caesium retention decreases with increasing target concentrations. The NaBSZn60Ca40 composition performs well at all three Cs₂O loadings.

7.7 SEM

SEM-EDX was used to confirm all samples were homogenous and single phase. Figure 7.23 and Figure 7.24 show examples of typical EDX maps collected for the NaBS series.

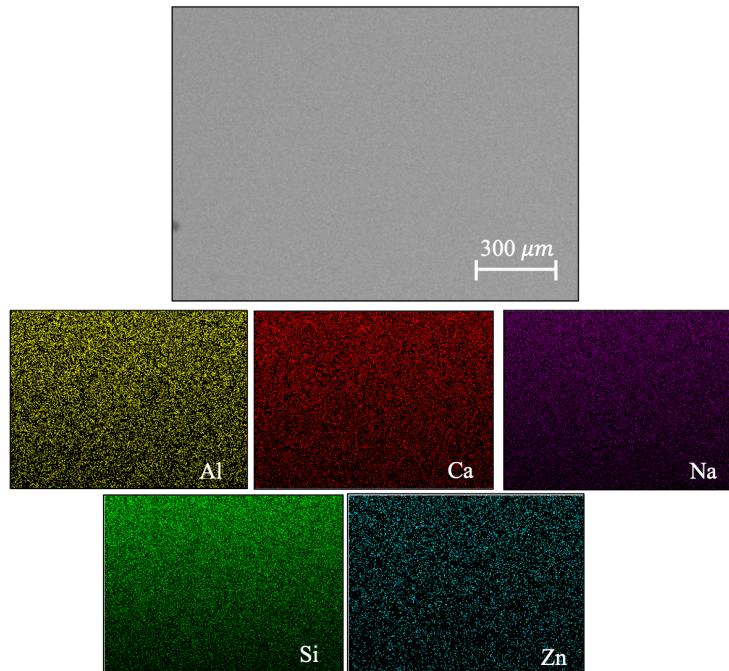


Figure 7.23: SEM-EDX elemental mapping of NaBSZn60Ca40 sample

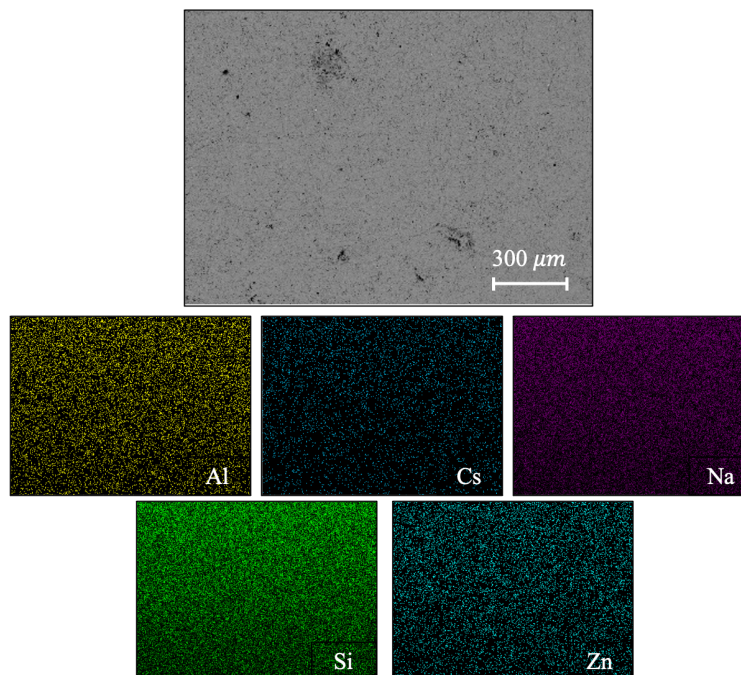


Figure 7.24: SEM-EDX elemental mapping of NaBSZn100Ca0Cs2 Sample

7.8 Off-gas Raman Spectroscopy

The following spectra were collected for each glass with the three different caesium loadings. The experimental set-up used to acquire these spectra can be found in Section 5.6. Figure 7.25 - Figure 7.30 show the summation of the intensities across the duration of each experiment and are separated by the glass compositions. All spectra were normalised to their respective maxima. An example of a 3-dimensional plot showing the variation in the intensities with time is shown in Appendix B.

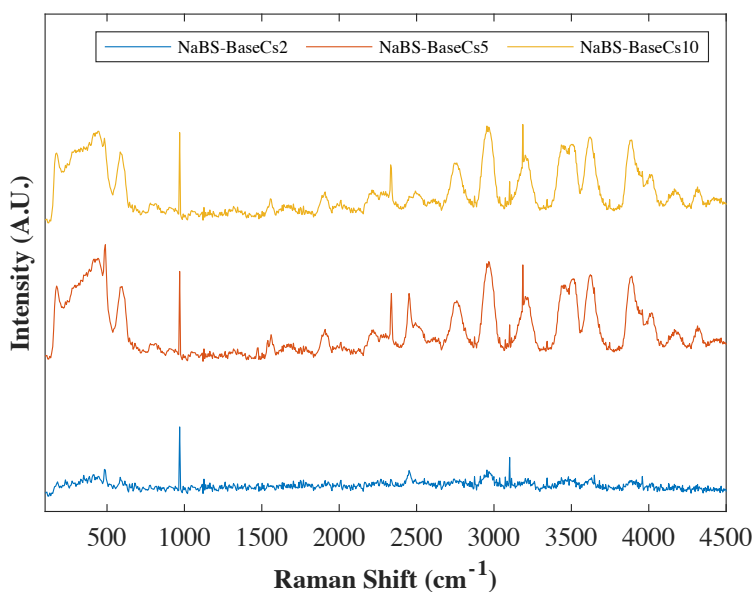


Figure 7.25: Gas phase Raman spectra for NaBS-Base glass with 2, 5, and 10 wt.% Cs_2O additions.

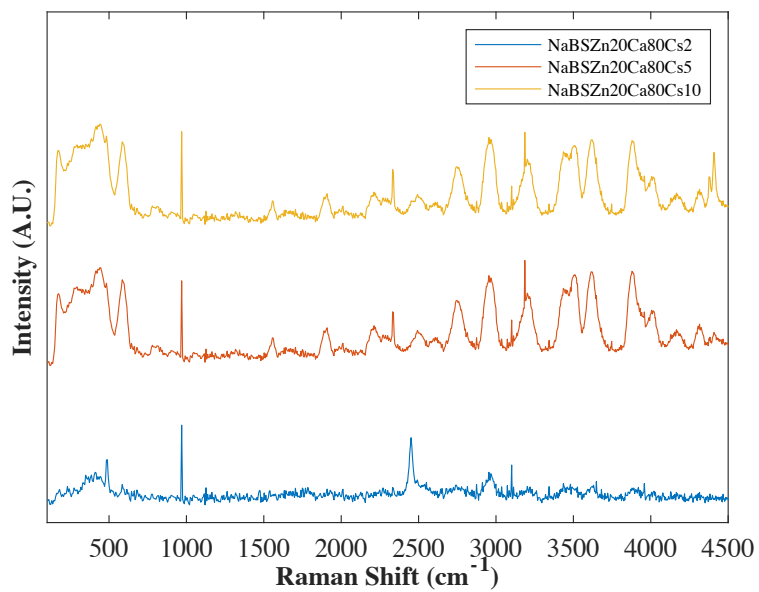


Figure 7.26: Gas phase Raman spectra for NaBSZn₂₀Ca₈₀ glass with 2, 5, and 10 wt.% Cs₂O additions.

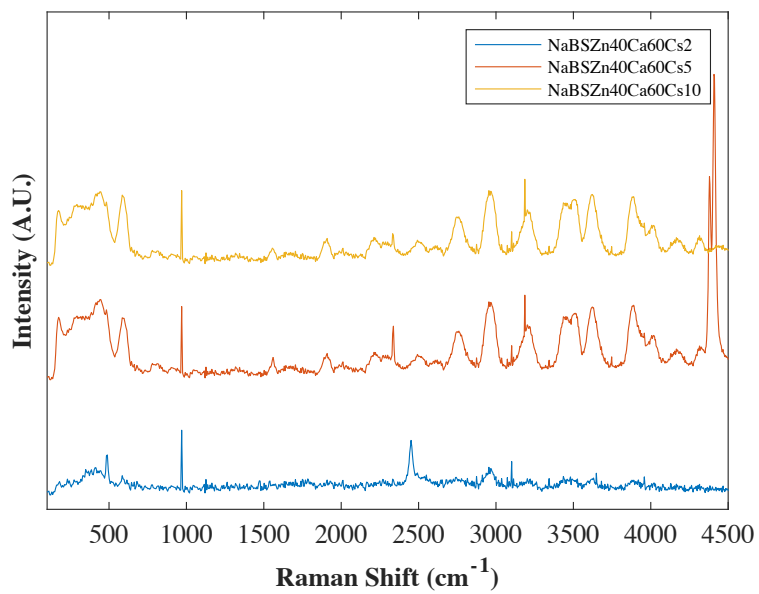


Figure 7.27: Gas phase Raman spectra for NaBSZn₄₀Ca₆₀ glass with 2, 5, and 10 wt.% Cs₂O additions.

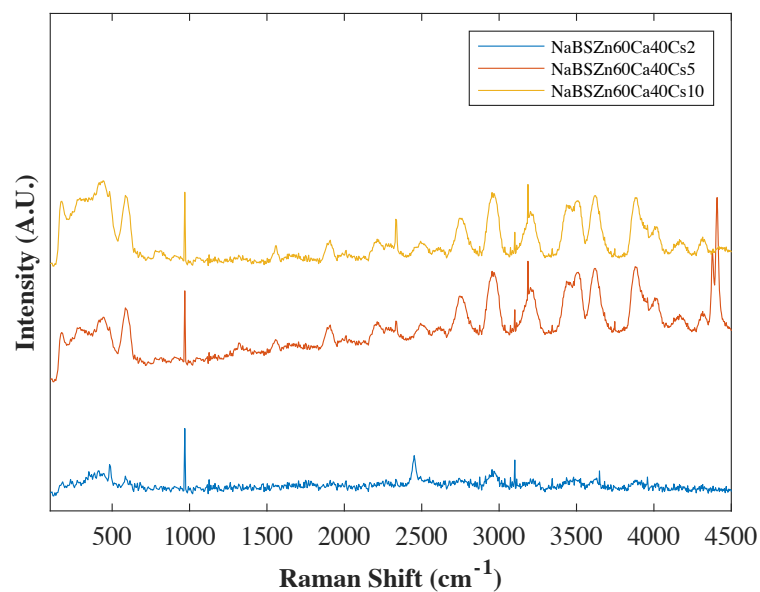


Figure 7.28: Gas phase Raman spectra for NaBSZn60Ca40 glass with 2, 5, and 10 wt.% Cs₂O additions

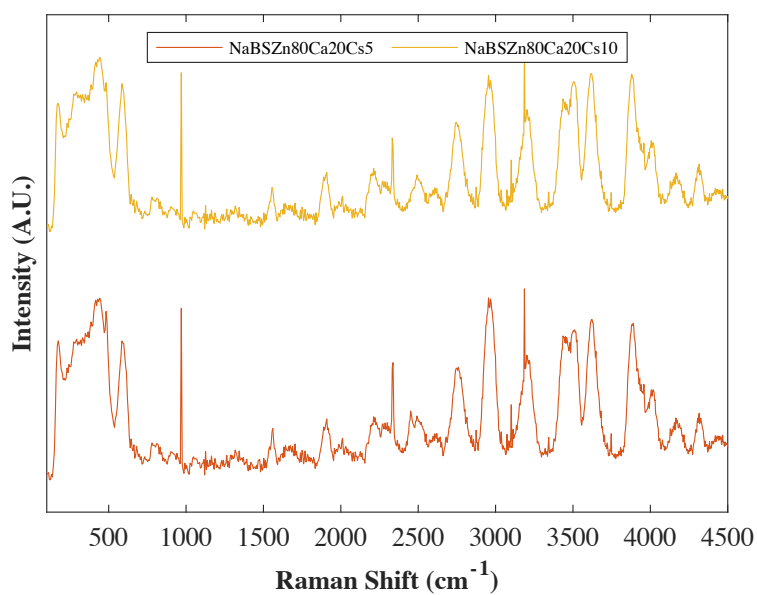


Figure 7.29: Gas phase Raman spectra for NaBSZn80Ca20 glass with 5, and 10 wt.% Cs₂O additions

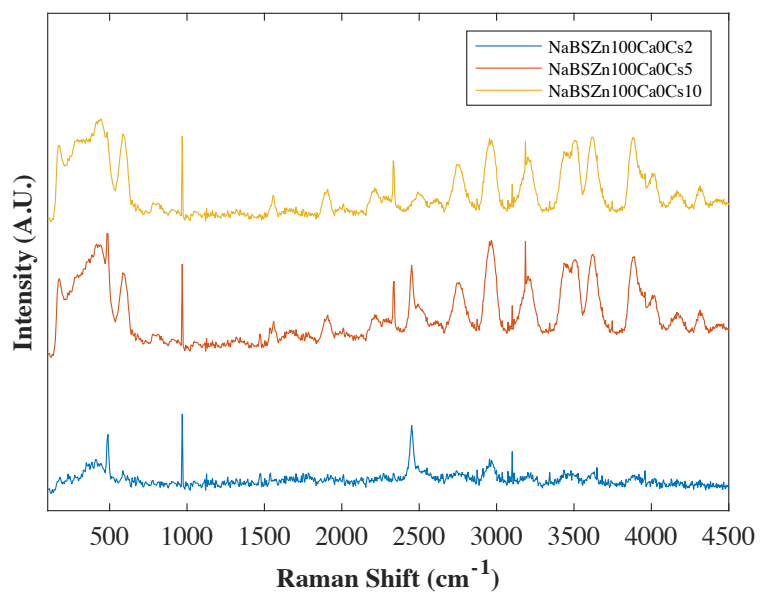


Figure 7.30: Gas phase Raman spectra for NaBSZn100Ca0 glass with 2, 5, and 10 wt.% Cs₂O additions.

Figure 7.31 - Figure 7.33 show the same data presented in Figure 7.25 - Figure 7.30 but separated into their respective caesium loading rather than their composition and plotted with the standard spectra that most closely matches the spectra of the glasses. For the NaBSCs2 series, these are the Cs_2O and CsBO_2 standards. For the 5 and 10 wt.% Cs_2O series, all three standards are shown. It can be observed in Figure 7.25 - Figure 7.33 the response for each glass is more dependent on the caesium concentration rather than the glass composition. This is evident due to the similarity in the data seen in Figure 7.31 - Figure 7.33.

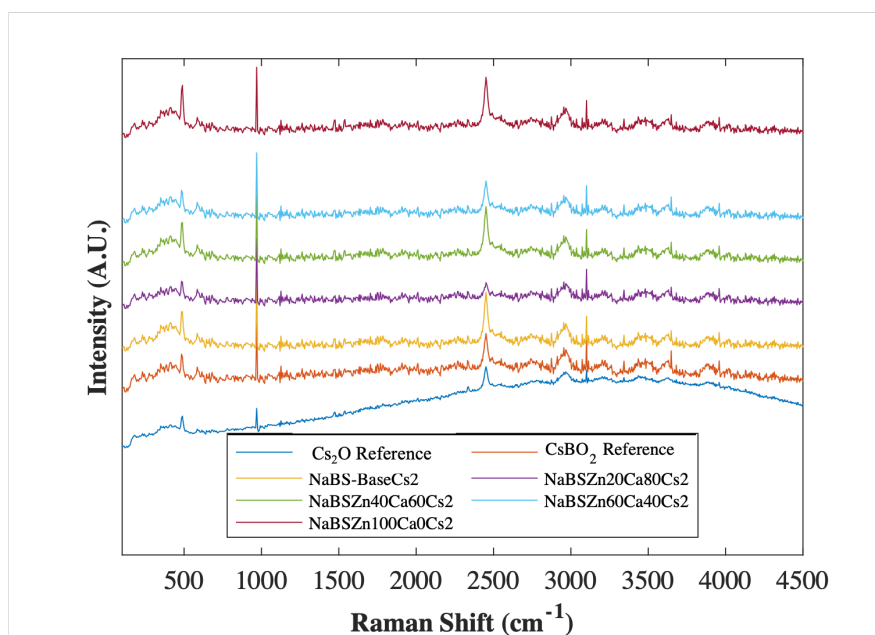


Figure 7.31: Gas phase Raman spectra for glasses doped with 2 wt.% Cs_2O .

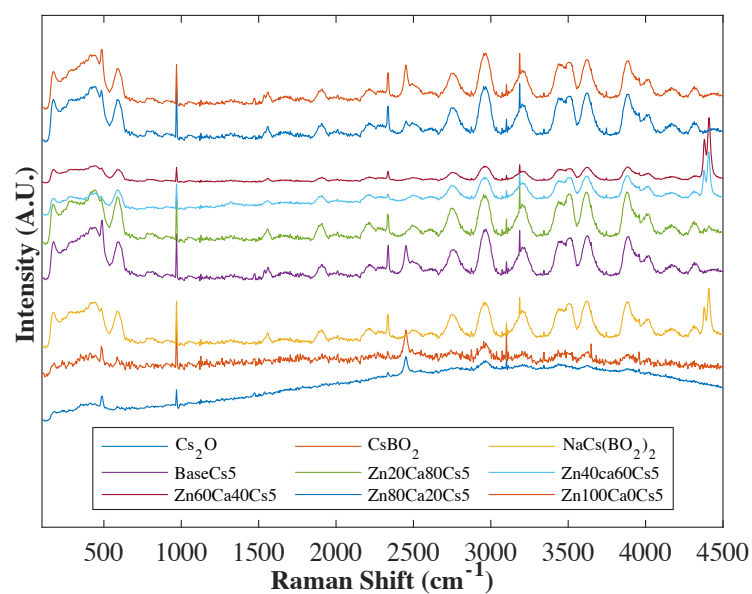


Figure 7.32: Gas phase Raman spectra for glasses doped with 5 wt.% Cs_2O .

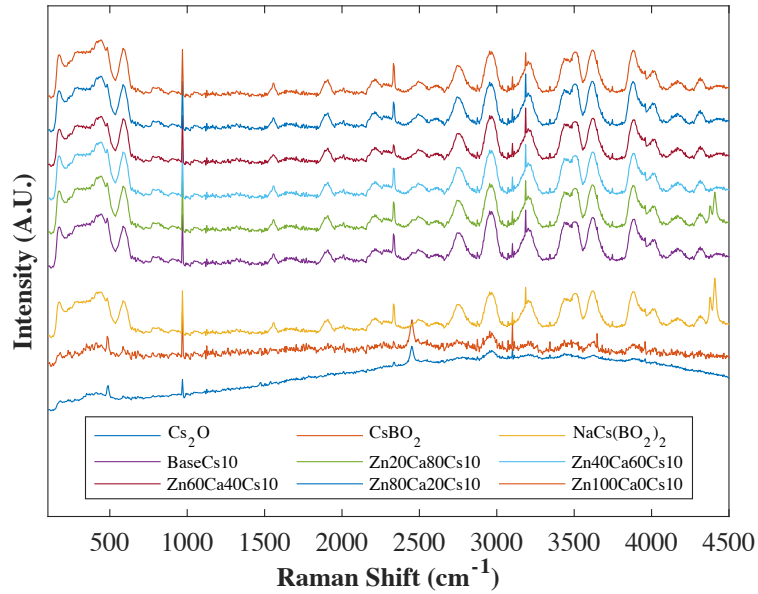


Figure 7.33: Gas phase Raman spectra for glasses doped with 10 wt.% Cs_2O

The off-gas Raman spectra for the glasses doped with 2 wt.% Cs_2O appear to match the standard spectra for both the Cs_2O standard and the CsBO_2 standard. However, a closer inspection around 3630 cm^{-1} indicates that the caesium vapours in these melts were CsBO_2 as a peak is present that is not seen in the Cs_2O standard. Between 100 cm^{-1} and $\sim 4250\text{ cm}^{-1}$, the spectra collected for the glasses doped with 5 and 10 wt.% Cs_2O indicate that the caesium vapours being measured are caesium (or mixed alkali) borate dimers. As seen in Figure 7.32 and Figure 7.33, the Raman spectra from the glass melts with 5 and 10 wt.% Cs_2O loadings largely match the spectra for the $\text{NaCs}(\text{BO}_2)_2$ standard. However, there are some small contributions from a Cs_2O phase in the 5 wt% Cs_2O glasses, with peaks present at $\sim 489\text{ cm}^{-1}$ and $\sim 2451\text{ cm}^{-1}$. A lack of peak at $\sim 3630\text{ cm}^{-1}$ confirms that the secondary species is Cs_2O . In the NaBSCs10 series, all peaks in the spectra can be attributed to the $\text{NaCs}(\text{BO}_2)_2$ standard. The doublet feature present at $\sim 4400 - 4500\text{ cm}^{-1}$ in the $\text{NaCs}(\text{BO}_2)_2$ spectra does not appear in all traces, however its presence does not correlate with caesium retention.

7.9 Discussion

All glasses remain X-Ray amorphous after caesium doping, regardless of the target waste loading. Thermal analysis and density measurements are inversely correlated, with T_g values decreasing with increasing density. The exceptions to this trend are the NaBS-Base glass and the NaBS-BaseCs2 glass as can be seen in Figure 7.7 - Figure 7.21. NaBSZn20Ca80 compositions see an increase in T_g compared to the base glass, then with increasing ZnO content, the T_g decreases, and the density values increase. Both density and T_g values show good agreement with similar glasses found in the literature [143]–[147]. Solid state Raman indicates that the structure of the glasses is not strongly influenced by caesium concentrations, however, there is evidence of MRO changes, as shown by the change in Raman spectra between 200 - 800 cm^{-1} .

A correlation between structural changes in the bulk glass and caesium retention was expected, as it has been suggested in the literature that the local environment of caesium within the glass will influence its volatility behaviour [8], [53], [55]. However, the relationship between caesium volatility and glass structure/composition is too complex to deduce correlations between variables that influence multiple aspects of a glass' properties. Furthermore, as this work investigated three different Cs_2O concentrations, it may not be possible to identify a universal trend to explain the caesium volatility behaviour at all three caesium loadings. Outlined below are what are believed to be the most likely explanations to the trends observed at different caesium loadings. The series have been separated based on the volatiles observed in the off-gas Raman spectra where the main volatile observed for the NaBSCs2 series was CsBO_2 and the main volatile for the NaBSCs5 and NaBSCs10 series was $\text{NaCs}(\text{BO}_2)_2$. Therefore it is expected that the behaviour of caesium in the NaBSCs2 series will be different to that of the NaBSCs5 and NaBSCs10.

Parkinson et al. found that Cs_2O additions to similar compositions to the ones studies here lead to a change in the fraction of danburite MRO units [8]. In Parkinson et al's work, caesium additions increased the fraction of danburite in glasses containing Al_2O_3 and decreased the danburite fraction in glasses with MgO present. It is likely that the inclusion of CaO in the glasses studied in this work would have a similar effect to MgO in Parkinson et al's work. From the Raman spectra of the glasses shown in Section 7.4, it can be seen that the danburite peak at $\sim 610 \text{ cm}^{-1}$ decreases significantly with ZnO and CaO additions. In contrast to the reedmergnerite peak at $\sim 500 \text{ cm}^{-1}$, the intensity of the danburite peak decreases with increasing ZnO concentrations. This change is highlighted in Figure 7.12 - Figure 7.15 and the change in

the MRO region of the Raman spectra due to caesium can be seen in Figure 7.34 - Figure 7.36. Here, the normalised intensities of the caesium doped glasses are subtracted from the corresponding base glass.

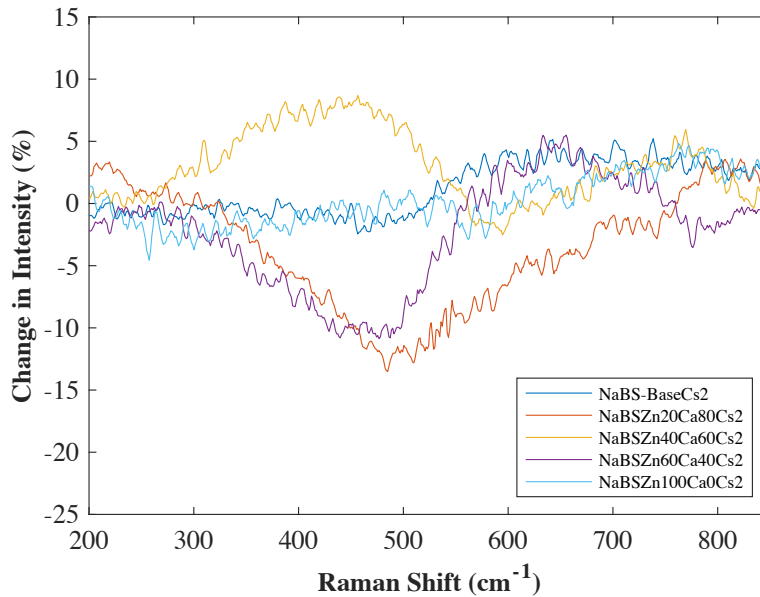


Figure 7.34: Residual difference between the base glasses and NaBS-Cs2 glasses

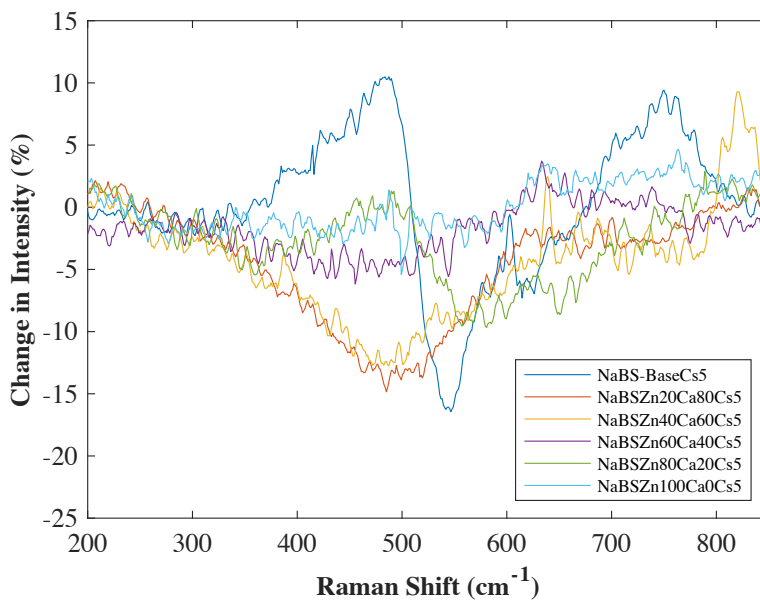


Figure 7.35: Residual difference between the base glasses and NaBS-Cs5 glasses

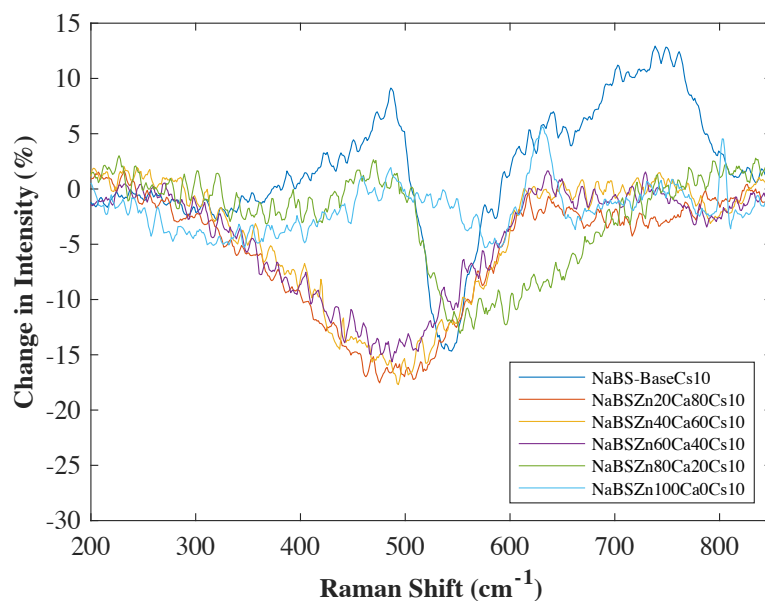


Figure 7.36: Residual difference between the base glasses and NaBS-Cs10 glasses

It has been suggested that ZnO tetrahedra occupy sites in MRO structures that would otherwise be occupied by BO_3 groups, leading to structures similar to willemite (Zn_2SiO_4) [148], [149]. Alternatively, it has been suggested that ZnO forms discrete tetrahedra that are charged balanced by alkali cations [148]. In both arrangements it is suggested that Cs^+ ions would associate with zinc tetrahedra, leading to improved caesium retention [55]. Banerjee et al. suggested that Cs^+ ions favoured ionic bonds with ZnO_4^{2-} tetrahedra over NBOs within the borate subnetwork (due to Zn tetrahedra being larger than BO_4^- units and forming more ionic bonds) [55]. Similarly, Parkinson et al. suggest that intermediate network formers removed alkali groups from the borate network, which would agree with Banerjee et al.'s suggestion of preferred association to ZnO_4^{2-} tetrahedra [8]. Furthermore, Banerjee et al. state that zinc can replace boron in reedmergnerite like MRO structures. In agreement with Banerjee et al., it is suggested here that at lower caesium concentrations (such as the NaBS-Cs2 series), caesium preferentially bonds to ZnO_4^{2-} tetrahedra, with each tetrahedra accommodating two caesium cations. However, Ca^{2+} ions may also associate with ZnO_4^{2-} tetrahedra, meaning caesium must associate with other structural units. As can be seen in Figure 7.37, the intensity of the peaks associated with reedmergnerite, danburite and BO_4 units all vary with the Zn:Ca ratio. Figure 7.37 shows the ratio of danburite:reedmergnerite and BO_4 :danburite against caesium retention. It can be observed that caesium volatility increases when BO_4 :danburite is high, which could indicate that Ca^{2+} are associating with the ZnO_4^{2-} units present in the reedmergnerite structure,

rather than forming danburite type structures. A high BO_4 :danburite ratio also indicates the increased presence of BO_4^- units, meaning there are boron units not associated with MRO structures available for caesium to associate with. This could explain CsBO_2 being the main volatile identified in the off-gas Raman spectra (see Figure 7.31), as it may suggest the formation CsBO_2 groups within the glass that then volatilise, which would be in agreement with the work of Stolyarova et al. [150].

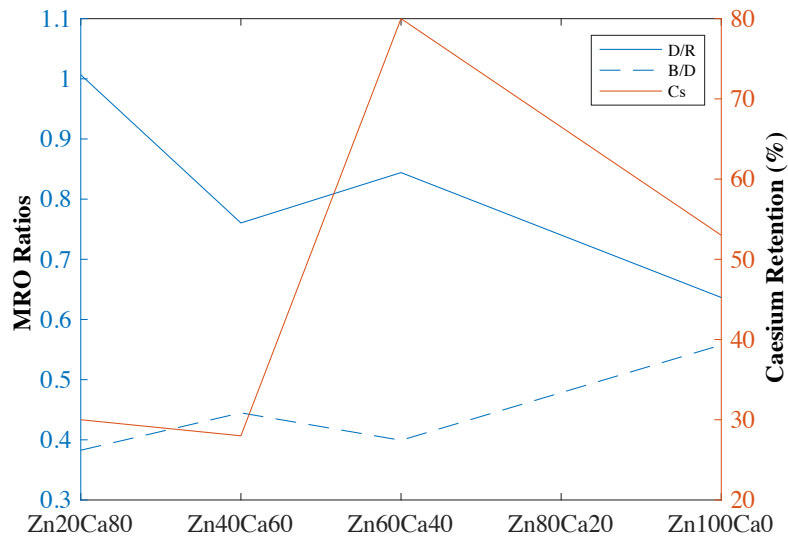


Figure 7.37: The ratio of MRO structures and caesium retention plotted against glass composition for the NaBS-Cs₂ series

However this explanation does not match the trends seen in the 5 and 10 wt.% Cs_2O loadings. For the higher Cs_2O loadings, a correlation exists between caesium retention and the Q^3 content of the glass, an observation also made by Parkinson et al. [54]. This idea was explored in this section of work by deconvoluting Raman spectra for all the glasses shown in this chapter. Figure 7.38 shows the concentration of Q^3 units against caesium retention, using the caesium retention values from Section 7.6. As can be observed in Figure 7.38, in the 5 and 10 wt.% Cs_2O loadings, there is an inverse correlation between caesium retention and Q^3 content, Q^3 appears to decrease as caesium retention increases, however no such correlation exists for the 2 wt.% Cs_2O series, the correlation seen at the 5 and 10 wt.% Cs_2O loadings is in agreement with Parkinson et al. [54]. This could be indicative of the change in the caesium coordination environment, as in low concentrations ($\sim 1 - 2$ mol%) caesium tends to be highly co-ordinated, with co-ordination numbers as high as 12. At higher concentrations (~ 4 mol%) the co-ordination number reduces to approximately 6 [151].

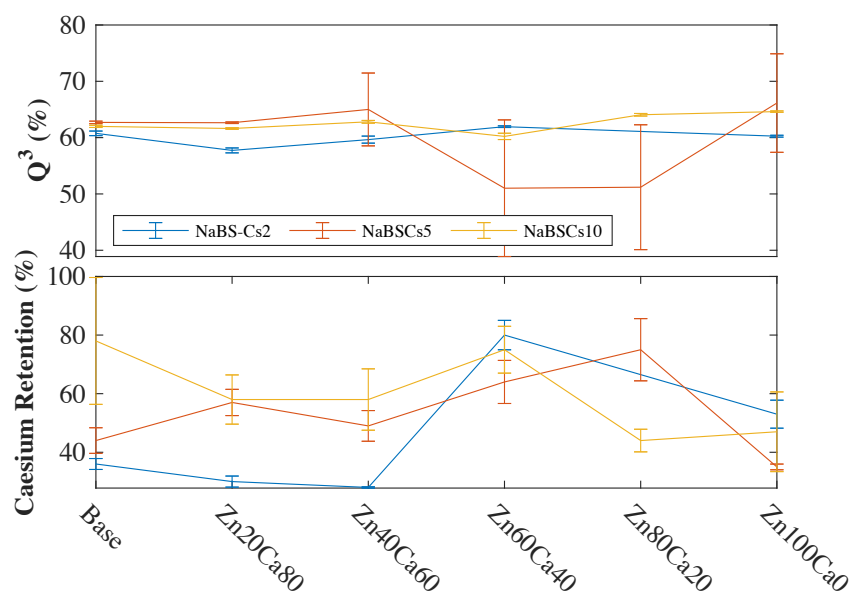


Figure 7.38: Q₃ concentrations (top) and caesium retention values (bottom) against glass composition

In the gas state Raman spectroscopy, it was observed that volatile species produced varied with the target caesium concentration. At 2 wt.% Cs₂O loadings the main volatile produced is CsBO₂. At 5 wt.% Cs₂O, peaks corresponding to Cs₂O are present, however the spectra generally match the spectra collected from the sodium caesium borate reference sample. Finally at 10 wt.% Cs₂O, the spectra closely resemble that of the sodium caesium borate sample. In the sodium caesium borate spectra and in some caesium doped glass spectra, a doublet feature is observed centred around ~4400 cm⁻¹. The feature is not present in all samples, despite the spectra being almost identical to the sodium caesium borate spectra below 4400 cm⁻¹. The cause of this peak is currently unknown.

7.10 Conclusion

XRD confirmed all glasses remain amorphous after remelting at all three caesium loading whilst SEM-EDS showed no signs of phase separation post caesium doping. Thermal analysis showed that high CaO concentrations increase T_g in comparison to NaBS-Base, whereas ZnO additions decreases T_g .

Solid state Raman spectroscopy showed that in the region responsible for MRO ($200 - 800 \text{ cm}^{-1}$) there was a notable decrease in peak height for reedmergnerite and danburite, whilst the BO_4 peak increases with increasing ZnO content. As CsBO_2 is the main volatile observed in the off-gas Raman for the NaBSCs2 series, it is suggested that a relationship exists between caesium retention, BO_4 units and zinc MRO units. In the NaBSCs5 and NaBSCs10 series, deconvolution of the main silica band revealed a trend in the NaBSCs5 and NaBSCs10 series between Q^3 and Cs retention as postulated by Parkinson et al. A change in the coordination environment of caesium may explain why a universal trend was not observed over all three caesium loadings.

Off-gas Raman spectroscopy was used to investigate the caesium species volatilised from the glass melts at all three caesium loadings. At 2 wt.% Cs_2O , the spectra for all glasses matched the peaks of the CsBO_2 standard. At 5 wt.% Cs_2O there was evidence of both the $\text{NaCs}(\text{BO}_2)_2$ and Cs_2O being present. At 10 wt.% Cs_2O , the spectra of all off-gas samples best matched $\text{NaCs}(\text{BO}_2)_2$. An intermittent doublet feature was observed in several traces at approximately 4400 cm^{-1} , however the cause of this feature is currently unknown.

8 Discussion

This work aimed to identify caesium bearing volatiles using a real time, in-situ system. Using a fibre coupled Raman spectrometer, a single pass flow cell and a custom made off-gas system, this has been achieved (see Section 4.12 for details). Three caesium reference materials were produced and analysed using the system described and the spectra collected were used to determine the caesium volatiles produced during glass melts as seen in Section 7.8. The three caesium reference materials used were, Cs_2O , CsBO_2 and $\text{NaCs}(\text{BO}_2)_2$, and were all identified as known caesium volatiles following a literature survey.

Off-gas Raman spectroscopy conducted on sodium borosilicate samples has shown that at the volatiles produced vary with caesium concentration. At lower concentrations, the spectra collected best match the CsBO_2 standard. At 5 wt.% Cs_2O , the primary caesium volatile the mixed alkali borate with some peaks associated with Cs_2O also present. Finally, at 10 wt.% Cs_2O , the spectra best match the mixed alkali borate, with no evidence of a second phase present. A comparison of literature values to the standard reference spectra collected showed little correlation and it is therefore suggested that reference materials would need to be measured in the same experimental setup to be useful.

Two glass series were investigated, iron phosphate glasses and sodium borosilicate glasses. Overall, the borosilicate glass series performed better in terms of caesium retention, with retention rates ranging from ~25% up to 80%, compared to 10 - 35% in the iron phosphate series. However, at low target caesium concentrations, the retention rates observed in the borosilicate series was notably lower, and off-gas Raman suggests that the primary volatiles produced changes with caesium content. Therefore it is possible that the retention rates observed in the IPG series could be improved with increased target caesium concentrations. These results also suggest a change in the local caesium environment, as the retention rates vary significantly and the volatiles produced change with the caesium concentrations present.

The borosilicate glasses were melted at 1050 °C, whilst the iron phosphate glasses were melted at 950 °C. However, these temperatures were arbitrary in the sense that they reflected typical melting temperatures reported in the literature and were not further optimised. It would be beneficial for future work to conduct viscosity measurements on these glass types and conduct volatility studies at viscosities appropriate for commercial melt processes. In doing so, this would give a better representation of the caesium losses that would be expected on a commercial scale.

However, even if the caesium retentions were optimised in the iron phosphate series, thermal stability of these glasses would still be of concern, as all glasses studied with additive concentrations less than 7.5 mol% crystallised after the caesium doped remelts. Whilst higher MnO or ZnO concentrations would mitigate this issue, caesium retention for both the IPG-Mn and IPG-Zn peaked at 5 mol% additions, indicating there would be a trade-off between caesium retention and thermal stability in these glasses. Of the four compositions that did not crystallise during the caesium doped remelt, the IPG-Zn10 composition is of the most interest to pursue further. The IPG-Zn10 composition would offer improved thermal stability when compared to the IPG-Base composition (currently the most promising phosphate composition considered for nuclear waste immobilisation) and improved caesium retention.

The NaBS series was also chosen to investigate the effect of ZnO on caesium volatility. Raman spectroscopy was used to observe structural changes with increasing ZnO content, with evidence of changes in the MRO region and an increase in the BO_4 peak intensity at 780 cm^{-1} . In borosilicate compositions, it has been suggested that ZnO tetrahedra occupy sites in MRO structures that would otherwise be occupied by BO_3 groups, leading to structures similar to willemite (Zn_2SiO_4) [148], [149]. Alternatively, it has been suggested that ZnO forms discrete tetrahedra that are charge balanced by alkali cations [148]. In both arrangements it is suggested that Cs^+ ions would associate with zinc tetrahedra, leading to improved caesium retention [55]. In the NaBSCs2 series, this appears to be true, with a correlation between the MRO unit changes and caesium retention. For the higher Cs_2O loadings, no such correlation exists, however a correlation was observed between caesium retention and the Q^3 content of the glass. The caesium retention observed across the NaBSCs2, NaBSCs5 and NaBSCs10 series varied, with no universal correlation that would explain the variation in caesium retention with composition. However, this could be due to a change in the caesium coordination environment, with the coordination number of caesium reducing with increasing concentration, which changes its bonding behaviour [151].

As can be seen in both the IPG and NaBS series, the effect of ZnO on caesium retention is highly dependent on the concentration it is present in. However, it appears to have a positive influence in both the IPG and NaBS series and this is something worthy of further research to target specific Zn:Cs ratios.

9 Conclusions and Further Work

9.1 Conclusions of Work to Date

An in-situ, real-time off-gas analyser system has been designed and commissioned. Building on information from the literature, a series of standard reference spectra were produced for expected volatiles in glass systems of interest to the nuclear sector. A series of borosilicate glasses were remelted with varying Cs_2O concentrations and the off-gases released from these melts were analysed using the system described above. It was found that the volatile species leaving the melt changed depending on the initial caesium concentration. At lower concentrations the primary volatile produced was suspected to be a caesium borate species. With increasing concentrations, a mixed alkali borate species was observed with a secondary caesium oxide peak present and at Cs_2O contents above 10 wt.%, the only volatile observed was a mixed alkali borate.

To improve our understanding of glass composition and caesium retention, two glass systems were produced and characterised before and after a caesium doped melt. Several possible links between the effect of glass composition and caesium retention were explored. In the borosilicate system, Q^3 content, MRO and the Zn structures were investigated but no correlation in the trends of these properties was observed that could explain the caesium retentions at all three waste loadings. At higher caesium concentrations, a correlation exists between caesium volatility and the Q^3 content. At the NaBSCs2 series, it is suggested that caesium preferentially associates with ZnO tetrahedra leading to increased retention. The addition of ZnO to the iron phosphate system was also seen to be beneficial to caesium retention and also helped improved the poor thermal stability that is typical of iron phosphate systems. Further research in this area is needed to establish the local environment of zinc.

The lab scale system commissioned in this project and the standard reference spectra collected offer the possibility of producing an off-gas Raman toolbox that if built upon, can be used by the wider scientific community to feed into glass formulations to improve the retention of problematic volatiles. Referring to the initial design criteria outlined in Section 4.12.1 (cost, caesium accountability, process compatibility and ease of modification), it can be seen that the system satisfies the design criteria (with the exception of caesium accountability where further work is needed to improve detection of caesium in the off-gas solutions, see Section 4.12.4). Several iterations of the system were outlined in Section 4.12, demonstrating that the system can be modified easily, without serious cost implications and can has the potential to be adapted

to suit new processing conditions (such as higher temperatures or change in processing atmosphere).

9.2 Suggestions for Further Work

In order to confirm the vapour species responsible for the off-gas Raman spectra presented in Sections 5.8 and 7.8, further characterisation of the reference materials is needed. Of particular interest would be repeated off-gas experiments with in-line mass spectroscopy, as this method would be able to determine the exact vapour species being analysed by the Raman spectrometer in real time. Basic characterisation of the reference materials (CsBO_2 and $\text{NaCs}(\text{BO}_2)_2$ samples) is on-going and will be included in any future publications.

Cs coordination environment has been reported to be high (typically 8-12 fold), however further work investigating the coordination environment of caesium in glasses range of compositions with varying caesium retention could prove useful to confirm statements made in the discussion section of Chapter 7. Similarly, confirming the local environment of zinc in these glasses types is of interest. Underpinned by the results of these experiments, a further series of glasses could be produced with targeted Cs:Zn ratios to confirm the role of zinc in caesium retention.

Work is ongoing on the IPG series with the aim of confirming the iron oxidation state both before and after the caesium doped melts, and the effect of the various additives on the iron oxidation state. In an effort to further explore IPGs in this line of work, it is suggested that the series be remade, using phosphoric acid as the P_2O_5 source in place of DAP. This should produce base glasses with a higher fraction of Fe^{3+} and could help suppress crystallisation during the caesium doped melts. It would also be of interest to investigate the local environment of zinc in these glass types to compare with the borosilicate series and to further explore the relationship between ZnO and caesium retention.

As mentioned in Section 4.12, there are several improvements that could be implanted to the off-gas design. For the purpose of this work, it was decided to delay any modifications to allow for comparable results across all samples analysed. However, the current system has shown that it is possible to implement an in-line, real time gas analyser system capable of speciating the volatiles produced from thermal treatment processes. Future designs should aim to incorporate a multi-pass cell to improve the system's sensitivity, and this system should be capable of operating at the temperatures associated with thermal treatment processes. Increasing the operating temperature of the analysis system would also allow for the

10 References

- [1] Pöyry Energy Ltd and Wood Nuclear Ltd., ‘UK Radioactive Waste Inventory 2019’, 2019.
- [2] M. T. Harrison, B. F. Dunnett, S. Morgan, C. R. Scales, and J. S. Small, ‘International research on vitrified HLW long-term behaviour: state of the art’, National Nuclear Laboratory, 2009.
- [3] C. M. Jantzen and M. I. Ojovan, ‘On Selection of Matrix (Wasteform) Material for Higher Activity Nuclear Waste Immobilization (Review)’, *Russ J Inorg Chem*, vol. 64, no. 13, pp. 1611–1624, 2019, doi: 10.1134/S0036023619130047.
- [4] C. L. Corkhill and N. C. Hyatt, *Nuclear Waste Management*. IOP Publishing, 2018. doi: 10.1088/978-0-7503-1638-5.
- [5] M. I. Ojovan and W. E. Lee, *An Introduction to Nuclear Waste Immobilisation*. Elsevier, 2014. doi: 10.1016/C2012-0-03562-4.
- [6] N. C. Hyatt and M. I. Ojovan, ‘Special issue: Materials for nuclear waste immobilization’, *Mater. Basel*, vol. 12, no. 21, pp. 12–15, 2019, doi: 10.3390/ma12213611.
- [7] Pöyry Energy Ltd and Wood Nuclear Ltd., ‘2019 UK Radioactive Waste Detailed Data’, 2019.
- [8] B. G. Parkinson, D. Holland, M. E. Smith, a. P. Howes, and C. R. Scales, ‘The effect of oxide additions on medium-range order structures in borosilicate glasses’, *J. Phys. Condens. Matter*, vol. 19, no. 41, p. 415114, 2007, doi: 10.1088/0953-8984/19/41/415114.
- [9] A. K. Varshneya, *Fundamentals of Inorganic Glasses*. Society of Glass Technology, 2014.
- [10] J. E. STANWORTH, ‘Oxide Glass Formation from the Melt’, *J. Am. Ceram. Soc.*, vol. 54, no. 1, pp. 61–63, Jan. 1971, doi: 10.1111/j.1151-2916.1971.tb12176.x.
- [11] K. -H Sun, ‘Fundamental Condition of Glass Formation’, *J. Am. Ceram. Soc.*, vol. 30, no. 9, pp. 277–281, 1947, doi: 10.1111/j.1151-2916.1947.tb19654.x.
- [12] W. H. Zachariasen, ‘The atomic arrangement in glass’, *J. Am. Chem. Soc.*, vol. 54, no. 10, pp. 3841–3851, 1932, doi: 10.1021/ja01349a006.
- [13] B. E. WARREN, ‘X-RAY DETERMINATION OF THE STRUCTURE OF GLASS’, *J. Am. Ceram. Soc.*, vol. 17, no. 1–12, pp. 249–254, Dec. 1934, doi: 10.1111/j.1151-2916.1934.tb19316.x.
- [14] B. E. Warren and A. D. Loring, ‘X-ray diffraction study of the structure of glass’, *Chem. Rev.*, vol. 26, no. 2, pp. 237–255, 1940, doi: 10.1021/cr60084a007.
- [15] G. N. Greaves, A. Fontaine, P. Lagarde, D. Raoux, and S. J. Gurman, ‘Local structure of silicate glasses’, *Nature*, vol. 293, no. 5834, pp. 611–616, 1981, doi: 10.1038/293611a0.
- [16] G. N. Greaves, ‘Exafs and the structure of glass’, *J. Non-Cryst. Solids*, vol. 71, pp. 203–217, 1985.

- [17] J. E. Shelby, *Introduction to Glass Science and Technology*. The Royal Society of Chemistry, 2005. doi: 10.1039/9781847551160.
- [18] D. W. Matson, S. K. Sharma, and J. A. Philpotts, 'The structure of high-silica alkali-silicate glasses. A Raman spectroscopic investigation', *J. Non-Cryst. Solids*, vol. 58, no. 2–3, pp. 323–352, Nov. 1983, doi: 10.1016/0022-3093(83)90032-7.
- [19] J. E. Shelby, *Introduction to Glass Science and Technology*. The Royal Society of Chemistry, 2005. doi: 10.1039/9781847551160.
- [20] W. J. Dell, P. J. Bray, and S. Z. Xiao, '11B NMR studies and structural modeling of Na₂O·B₂O₃·SiO₂ glasses of high soda content', *J. Non-Cryst. Solids*, vol. 58, no. 1, pp. 1–16, 1983, doi: 10.1016/0022-3093(83)90097-2.
- [21] J. O. Isard, 'The mixed alkali effect in glass', *J. Non-Cryst. Solids*, vol. 1, no. 3, pp. 235–261, Apr. 1969, doi: 10.1016/0022-3093(69)90003-9.
- [22] P. Maass, 'Towards a theory for the mixed alkali effect in glasses', *J. Non-Cryst. Solids*, vol. 255, no. 1, pp. 35–46, 1999, doi: 10.1016/S0022-3093(99)00422-6.
- [23] J. Zhong and P. J. Bray, 'Change in boron coordination in alkali borate glasses, and mixed alkali effects, as elucidated by NMR', *J. Non-Cryst. Solids*, vol. 111, no. 1, pp. 67–76, Sep. 1989, doi: 10.1016/0022-3093(89)90425-0.
- [24] R. K. Brow, 'Review: the structure of simple phosphate glasses', *J Non Cryst Solids*, vol. 263–264, pp. 1–28, 2000.
- [25] U. Hoppe, 'A structural model for phosphate glasses', *J Non Cryst Solids*, vol. 195, no. 1–2, pp. 138–147, 1996, doi: 10.1016/0022-3093(95)00524-2.
- [26] R. K. Brow, D. R. Tallant, J. J. Hudgens, S. W. Martin, and A. D. Irwin, 'The short-range structure of sodium ultraphosphate glasses', *J. Non-Cryst. Solids*, vol. 177, no. C, pp. 221–228, 1994, doi: 10.1016/0022-3093(94)90534-7.
- [27] U. Hoppe, 'A structural model for phosphate glasses', *J. Non-Cryst. Solids*, vol. 195, no. 1–2, pp. 138–147, 1996, doi: 10.1016/0022-3093(95)00524-2.
- [28] R. K. Brow, C. A. Click, and T. M. Alam, 'Modifier coordination and phosphate glass networks', *J. Non-Cryst. Solids*, vol. 274, no. 1–3, pp. 9–16, Sep. 2000, doi: 10.1016/S0022-3093(00)00178-2.
- [29] A. C. Wright *et al.*, 'The atomic and magnetic structure and dynamics of iron phosphate glasses', *Phys Chem Glas - Eur J Glas Sci Technol Part B*, vol. 53, no. 6, pp. 227–244, 2012.
- [30] G. K. Marasinghe *et al.*, 'Structural features of iron phosphate glasses', *J Non Cryst Solids*, vol. 222, pp. 144–152, 1997, doi: 10.1016/S0022-3093(97)90107-1.
- [31] S. T. Reis, W. M. Pontuschka, A. Mogaš-Milanković, and C. S. M. Partiti, 'Structural features of iron-phosphate glass', *J Am Ceram Soc*, vol. 100, no. 5, pp. 1976–1981, 2017, doi: 10.1111/jace.14731.
- [32] Nuclear Decommissioning Authority, 'Radioactive Wastes in the UK : UK Radioactive Waste Inventory Report', 2017.
- [33] M. I. Ojovan and W. E. Lee, *An Introduction to Nuclear Waste Immobilisation*. Elsevier, 2014. doi: 10.1016/C2012-0-03562-4.
- [34] C. L. Corkhill and N. C. Hyatt, *Nuclear Waste Management*, no. November. IOP Publishing, 2018. doi: 10.1088/978-0-7503-1638-5.

- [35] NDA - Nuclear Decommissioning Authority, 'What are the main waste categories?' <https://ukinventory.nda.gov.uk/about-radioactive-waste/what-is-radioactivity/what-are-the-main-waste-categories/>
- [36] W. E. Lee, M. I. Ojovan, M. C. Stennett, and N. C. Hyatt, 'Immobilisation of radioactive waste in glasses, glass composite materials and ceramics', *Adv Appl Ceram*, vol. 105, no. 1, pp. 3–12, 2006, doi: 10.1179/174367606X81669.
- [37] W. J. Weber, 'Radiation and Thermal Ageing of Nuclear Waste Glass', *Procedia Mater. Sci.*, vol. 7, pp. 237–246, 2014, doi: 10.1016/j.mspro.2014.10.031.
- [38] P. B. Rose, D. I. Woodward, M. I. Ojovan, N. C. Hyatt, and W. E. Lee, 'Crystallisation of a simulated borosilicate high-level waste glass produced on a full-scale vitrification line', *J Non Cryst Solids*, vol. 357, no. 15, pp. 2989–3001, Jul. 2011, doi: 10.1016/j.jnoncrysol.2011.04.003.
- [39] B. F. Dunnett, 'Review of the Development of UK High Level Waste Vitrified Product', NDA, 4, 2007.
- [40] M. I. Ojovan and W. E. Lee, 'Chapter 17 – Immobilisation of Radioactive Wastes in Glass', in *An Introduction to Nuclear Waste Immobilisation*, 2005, pp. 213–249. doi: 10.1016/B978-008044462-8/50019-3.
- [41] M. I. Ojovan and W. E. Lee, 'Immobilisation of Radioactive Wastes in Glass', in *An Introduction to Nuclear Waste Immobilisation*, 2005, pp. 213–249. doi: 10.1016/B978-008044462-8/50019-3.
- [42] B. F. Dunnett, 'Review of the Development of UK High Level Waste Vitrified Product', 2007.
- [43] V. Petitjean, C. Fillet, R. Boen, C. Veyer, and T. Flament, 'Development of Vitrification Process and Glass Formulation for Nuclear Waste Conditioning', 2002.
- [44] B. C. Childs, F. Poineau, K. R. Czerwinski, and A. P. Sattelberger, 'The nature of the volatile technetium species formed during vitrification of borosilicate glass', *J. Radioanal. Nucl. Chem.*, vol. 306, no. 2, pp. 417–421, 2015, doi: 10.1007/s10967-015-4203-5.
- [45] D.-S. Kim *et al.*, 'Development and Testing of ICV Glasses for Hanford LAW', Richland, WA (United States), Aug. 2003. doi: 10.2172/15008146.
- [46] B. Luckscheiter and M. Nesovic, 'Development of glasses for the vitrification of high level liquid waste (HLLW) in a joule heated ceramic melter', *Waste Manag.*, vol. 16, no. 7, pp. 571–578, Jan. 1996, doi: 10.1016/S0956-053X(97)88231-1.
- [47] A. A. Kruger, K. A. Matlack, I. L. Pegg, and W. Gong, 'Final Report - Glass Formulation Testing to Increase Sulfate Volatilization from Melter, VSL-04R4970-1, Rev. 0, dated 2/24/05', Richland, WA (United States), Nov. 2013. doi: 10.2172/1105971.
- [48] J. S. McCloy *et al.*, 'Rhenium Solubility in Borosilicate Nuclear Waste Glass: Implications for the Processing and Immobilization of Technetium-99', Nov. 2012. doi: 10.1021/es302734y.
- [49] K. Xu, D. A. Pierce, P. R. Hrma, M. J. Schweiger, and A. A. Kruger, 'Rhenium volatilization in waste glasses', *J. Nucl. Mater.*, vol. 464, pp. 382–388, 2015, doi: 10.1016/j.jnucmat.2015.05.005.
- [50] S. A. Luksic, P. R. Hrma, and A. A. Kruger, 'Materials for Tc Capture to Increase Tc Retention in Glass Waste Form', 2015.

- [51] M. Bertmer, L. Züchner, J. C. C. Chan, and H. Eckert, ‘Short and Medium Range Order in Sodium Aluminoborate Glasses. 2. Site Connectivities and Cation Distributions Studied by Rotational Echo Double Resonance NMR Spectroscopy’, *J. Phys. Chem. B*, vol. 104, no. 28, pp. 6541–6553, 2000, doi: 10.1021/jp9941918.
- [52] D. Cabaret, ‘Medium range structure of borosilicate glasses from Si K-edge XANES: a combined approach based on multiple scattering and molecular dynamics calculations’, *J. Non-Cryst. Solids*, vol. 289, no. 1–3, pp. 1–8, 2001, doi: 10.1016/S0022-3093(01)00733-5.
- [53] A. Vegiri, C. E. Varsamis, and E. I. Kamitsos, ‘Composition and temperature dependence of cesium-borate glasses by molecular dynamics’, *J. Chem. Phys.*, vol. 123, no. 1, p. 014508, Jul. 2005, doi: 10.1063/1.1943414.
- [54] B. G. Parkinson, D. Holland, M. E. Smith, A. P. Howes, and C. R. Scales, ‘Effect of minor additions on structure and volatilization loss in simulated nuclear borosilicate glasses’, *J. Non-Cryst. Solids*, vol. 353, no. 44–46, pp. 4076–4083, 2007, doi: 10.1016/j.jnoncrysol.2007.06.016.
- [55] D. Banerjee, A. Joseph, V. K. Sudarsan, P. K. Wattal, and D. Das, ‘Effect of composition and temperature on volatilization of Cs from borosilicate glasses’, *J. Am. Ceram. Soc.*, vol. 95, no. 4, pp. 1284–1289, 2012, doi: 10.1111/j.1551-2916.2012.05077.x.
- [56] T. Jin, D.-S. Kim, and M. J. Schweiger, ‘Effect of Sulfate on Rhenium Partitioning during Melting of Low-Activity-Waste Glass Feeds’, 2014.
- [57] M. Asano and Y. Yasue, ‘Vapor Species over Na₂O-B₂O₃-SiO₂-Cs₂O Glass’, *J Nucl Sci Technol*, vol. 22, no. 12, pp. 1029–1032, Dec. 1985, doi: 10.1080/18811248.1985.9735760.
- [58] M. Asano, T. Kou, and Y. Yasue, ‘Mass Spectrometric Study Of Vaporisation Of Caesium-Containing Borosilicate Glasses’, *J Non Cryst Solids*, vol. 92, pp. 245–260, 1987.
- [59] V. L. Stolyarova, S. I. Lopatin, and E. N. Plotnikov, ‘Mass spectrometric investigation of the thermodynamic properties of glass melts in the Cs₂O-B₂O₃-SiO₂ system at high temperatures’, *Glass Phys. Chem.*, vol. 32, no. 5, pp. 543–549, Oct. 2006, doi: 10.1134/S1087659606050087.
- [60] S. I. Lopatin and V. L. Stolyarova, ‘Thermodynamic properties and structure of gaseous metaborates’, *Glas Phys Chem*, vol. 32, no. 3, pp. 353–369, May 2006, doi: 10.1134/S1087659606030163.
- [61] V. L. Stolyarova, S. I. Lopatin, O. L. Belousova, and L. V. Grishchenko, ‘Phase equilibria and thermodynamic properties of components in the Cs₂O-B₂O₃-SiO₂ system at high temperatures’, *Glas Phys Chem*, vol. 32, no. 1, pp. 55–62, 2006, doi: 10.1134/S108765960601007X.
- [62] M. Asano and Y. Yasue, ‘Mass spectrometric study of the vaporization of sodium borosilicate glasses’, *J Nucl Mater*, vol. 138, no. 1, pp. 65–72, Mar. 1986, doi: 10.1016/0022-3115(86)90256-4.
- [63] M. Asano and Y. Yasue, ‘Vapor Species over Na₂O-B₂O₃-SiO₂-Cs₂O Glass’, *J. Nucl. Sci. Technol.*, vol. 22, no. 12, pp. 1029–1032, Dec. 1985, doi: 10.1080/18811248.1985.9735760.

- [64] I. W. Donald, *The science and technology of inorganic glasses and glass-ceramics: from the past to the present to the future*. Sheffield: Society of glass technology, 2016.
- [65] C. M. Jantzen, ‘Systems approach to nuclear waste glass development’, *J. Non-Cryst. Solids*, vol. 84, no. 1–3, pp. 215–225, 1986, doi: 10.1016/0022-3093(86)90780-5.
- [66] D. E. Day *et al.*, ‘Iron Phosphate Glass for Vitrifying Hanford AZ102 LAW in Joule Heated and Cold Crucible Induction Melters – 12240’, in *Waste Management*, 2012, pp. 1–16.
- [67] C.-W. Kim and D. E. Day, ‘Immobilization of Hanford LAW in iron phosphate glasses’, *J. Non-Cryst. Solids*, vol. 331, no. 1–3, pp. 20–31, Dec. 2003, doi: 10.1016/j.jnoncrysol.2003.08.070.
- [68] P. A. Bingham and R. J. Hand, ‘Sulphate incorporation and glass formation in phosphate systems for nuclear and toxic waste immobilization’, *Mater. Res. Bull.*, vol. 43, no. 7, pp. 1679–1693, 2008, doi: 10.1016/j.materresbull.2007.07.024.
- [69] M. G. Mesko, D. E. Day, and B. C. Bunker, ‘Immobilization of CsCl and SrF₂ in iron phosphate glass’, *Waste Manag.*, vol. 20, no. 4, pp. 271–278, 2000, doi: 10.1016/S0956-053X(99)00331-1.
- [70] A. S. Aloy, B. Ya. Galkin, B. S. Kuznetsov, R. I. Lyubtsev, and V. M. Esimantovskii, ‘Fractionation Of Liquid Highly-Radioactive Wastes And The Incorporation Of Long-Lived Radionuclides Into Ceramics And Vitreous Compositions’, in *Waste Management '89*, 1989, pp. 677–681.
- [71] D. E. Day, Z. Wu, C. S. Ray, and P. R. Hrma, ‘Chemically durable iron phosphate glass wastefoms’, *J. Non-Cryst. Solids*, vol. 241, no. 1, pp. 1–12, 1998, doi: 10.1016/S0022-3093(98)00759-5.
- [72] M. Karabulut, B. Yuce, O. Bozdogan, H. Ertap, and G. M. Mammadov, ‘Effect of boron addition on the structure and properties of iron phosphate glasses’, *J. Non-Cryst. Solids*, vol. 357, no. 5, pp. 1455–1462, 2011, doi: 10.1016/j.jnoncrysol.2010.11.023.
- [73] G. K. Marasinghe *et al.*, ‘Structural features of iron phosphate glasses’, *J. Non-Cryst. Solids*, vol. 222, pp. 144–152, 1997, doi: 10.1016/S0022-3093(97)90107-1.
- [74] A. Moguš-Milanković, A. Santic, and D. E. Day, ‘Structural and Electrical properties of Iron phosphate glasses’.
- [75] M. Karabulut, G. K. Marasinghe, C. S. Ray, D. E. Day, O. Ozturk, and G. D. Waddill, ‘X-ray photoelectron and Mössbauer spectroscopic studies of iron phosphate glasses containing U, Cs and Bi’, *J. Non-Cryst. Solids*, vol. 249, no. 2–3, pp. 106–116, Jul. 1999, doi: 10.1016/S0022-3093(99)00332-4.
- [76] C. S. Ray, X. Fang, M. Karabulut, G. K. Marasinghe, and D. E. Day, ‘Effect of melting temperature and time on iron valence and crystallization of iron phosphate glasses’, *J. Non-Cryst. Solids*, vol. 249, no. 1, pp. 1–16, 1999, doi: 10.1016/S0022-3093(99)00304-X.
- [77] X. Yu, D. E. Day, G. J. Long, and R. K. Brow, ‘Properties and structure of sodium-iron phosphate glasses’, *J. Non-Cryst. Solids*, vol. 215, no. 1, pp. 21–31, 1997, doi: 10.1016/S0022-3093(97)00022-7.
- [78] M. Karabulut *et al.*, ‘An investigation of the local iron environment in iron phosphate glasses having different Fe(II) concentrations’, *J. Non-Cryst. Solids*, vol. 306, no. 2, pp. 182–192, 2002, doi: 10.1016/S0022-3093(02)01053-0.

- [79] C.-W. Kim *et al.*, ‘Chemically durable iron phosphate glasses for vitrifying sodium bearing waste (SBW) using conventional and cold crucible induction melting (CCIM) techniques’, *J. Nucl. Mater.*, vol. 322, no. 2–3, pp. 152–164, 2003, doi: 10.1016/S0022-3115(03)00325-8.
- [80] G. K. Marasinghe *et al.*, ‘Properties and structure of vitrified iron phosphate nuclear wasteforms’, *J. Non-Cryst. Solids*, vol. 263, pp. 146–154, 2000, doi: 10.1016/S0022-3093(99)00631-6.
- [81] A. C. Wright *et al.*, ‘The atomic and magnetic structure and dynamics of iron phosphate glasses’, *Phys. Chem. Glas. - Eur. J. Glass Sci. Technol. Part B*, vol. 53, no. 6, pp. 227–244, 2012.
- [82] A. K. Varshneya and J. C. Mauro, ‘Glass formation principles’, in *Fundamentals of Inorganic Glasses*, 2019. doi: 10.1016/b978-0-12-816225-5.00003-1.
- [83] A. Hrubý, ‘Evaluation of glass-forming tendency by means of DTA’, *Czechoslov J Phys*, vol. 22, no. 11, pp. 1187–1193, 1972, doi: 10.1007/BF01690134.
- [84] X. Li, A. Lu, and H. Yang, ‘Structure of ZnO-Fe₂O₃-P₂O₅ glasses probed by Raman and IR spectroscopy’, *J Non Cryst Solids*, vol. 389, pp. 21–27, 2014, doi: 10.1016/j.jnoncrysol.2014.01.051.
- [85] P. A. Bingham, R. J. Hand, and S. D. Forder, ‘Doping of iron phosphate glasses with Al₂O₃, SiO₂ or B₂O₃ for improved thermal stability’, *Mater. Res. Bull.*, vol. 41, no. 9, pp. 1622–1630, 2006, doi: 10.1016/j.materresbull.2006.02.029.
- [86] I. W. Donald, B. L. Metcalfe, S. K. Fong, and L. A. Gerrard, ‘The influence of Fe₂O₃ and B₂O₃ additions on the thermal properties, crystallization kinetics and durability of a sodium aluminum phosphate glass’, *J. Non-Cryst. Solids*, vol. 352, no. 28–29, pp. 2993–3001, 2006, doi: 10.1016/j.jnoncrysol.2006.04.007.
- [87] D. E. Day, ‘An Alternative Host Matrix Based On Iron Phosphate Glasses For The Vitrification Of Specialized Waste Forms’, Dec. 2000. doi: 10.2172/827407.
- [88] A. Moguš-Milanković, A. Furic, and D. E. Day, ‘No Title’, in *Materials Research Society Symposium - Proceedings*, 2001, p. 153.
- [89] P. A. Bingham, R. J. Hand, and S. D. Forder, ‘Doping of iron phosphate glasses with Al₂O₃, SiO₂ or B₂O₃ for improved thermal stability’, *Mater Res Bull*, vol. 41, no. 9, pp. 1622–1630, 2006, doi: 10.1016/j.materresbull.2006.02.029.
- [90] A. J. Fisher *et al.*, ‘Short communication: The dissolution of UK simulant vitrified high-level-waste in groundwater solutions’, *J. Nucl. Mater.*, vol. 538, p. 152245, Sep. 2020, doi: 10.1016/j.jnucmat.2020.152245.
- [91] B. Ravel and M. Newville, ‘ATHENA , ARTEMIS , HEPHAESTUS : data analysis for X-ray absorption spectroscopy using IFEFFIT’, *J. Synchrotron Radiat.*, vol. 12, no. 4, pp. 537–541, Jul. 2005, doi: 10.1107/S0909049505012719.
- [92] K. Lagarec and D. G. Rancourt, ‘Recoil. Mossbauer Spectral Analysis Software for Windows’. University of Ottawa, Ottawa, 1998.
- [93] P. A. Bingham, R. J. Hand, S. D. Forder, and A. Lavaysierre, ‘Vitrified metal finishing wastes: II. Thermal and structural characterisation’, *J. Hazard. Mater.*, vol. 122, no. 1–2, pp. 129–138, 2005, doi: 10.1016/j.jhazmat.2005.03.031.
- [94] C. Le Losq, D. R. Neuville, R. Moretti, and J. Roux, ‘Determination of water content in silicate glasses using Raman spectrometry: Implications for the study of explosive

- volcanism', *Am. Mineral.*, vol. 97, no. 5–6, pp. 779–790, 2012, doi: 10.2138/am.2012.3831.
- [95] H. Behrens, J. Roux, D. R. Neuville, and M. Siemann, 'Quantification of dissolved H₂O in silicate glasses using confocal microRaman spectroscopy', *Chem. Geol.*, vol. 229, no. 1–3, pp. 96–112, 2006, doi: 10.1016/j.chemgeo.2006.01.014.
- [96] WaveMetrics, 'Igor Pro 8'. WaveMetrics, Oregon.
- [97] H. Kamizono, S. Kikkawa, Y. Togashi, and S. Tashiro, 'Volatilization of ¹³⁷Cs and ¹⁰⁶Ru from Borosilicate Glass Containing Actual High-Level Waste', *J. Am. Ceram. Soc.*, vol. 72, no. 8, pp. 1438–1441, Aug. 1989, doi: 10.1111/j.1151-2916.1989.tb07669.x.
- [98] C. W. Sill, 'Volatility of cesium and strontium from a synthetic basalt', *Nucl. Chem. Waste Manag.*, vol. 8, no. 2, pp. 97–105, Jan. 1988, doi: 10.1016/0191-815X(88)90068-X.
- [99] K. Nakamoto, *Infrared and Raman Spectra of Inorganic and Coordination Compounds, Part A: Theory and Applications in Inorganic Chemistry*. New York, UNITED STATES: John Wiley & Sons, Incorporated, 2009.
- [100] P. Larkin, 'Chapter 1 - Introduction: Infrared and Raman Spectroscopy', P. B. T.-I. and R. S. Larkin, Ed. Oxford: Elsevier, 2011, pp. 1–5. doi: <https://doi.org/10.1016/B978-0-12-386984-5.10001-1>.
- [101] N. Colthup, *Introduction to Infrared and Raman Spectroscopy*. Saint Louis, UNITED STATES: Elsevier Science & Technology, 1975.
- [102] D. R. Neuville, D. De Ligny, and G. S. Henderson, 'Advances in Raman spectroscopy applied to earth and material sciences', *Rev. Mineral. Geochem.*, vol. 78, pp. 509–541, 2014, doi: 10.2138/rmg.2013.78.13.
- [103] M. Hass, 'Temperature dependence of the Raman spectrum of vitreous silica', *Solid State Commun.*, vol. 7, no. 15, pp. 1069–1071, 1969, doi: 10.1016/0038-1098(69)90473-6.
- [104] I. Daniel, P. Gillet, B. T. Poe, and P. F. McMillan, 'In-situ high-temperature Raman spectroscopic studies of aluminosilicate liquids', *Phys. Chem. Miner.*, vol. 22, no. 2, pp. 74–86, 1995, doi: 10.1007/BF00202467.
- [105] W. L. Konijnendijk and J. M. Stevels, 'The structure of borosilicate glasses studied by Raman scattering', *J. Non-Cryst. Solids*, vol. 20, no. 2, pp. 193–224, 1976, doi: 10.1016/0022-3093(76)90132-0.
- [106] B. G. Parkinson *et al.*, 'Quantitative measurement of Q₃ species in silicate and borosilicate glasses using Raman spectroscopy', *J. Non-Cryst. Solids*, vol. 354, no. 17, pp. 1936–1942, 2008, doi: 10.1016/j.jnoncrysol.2007.06.105.
- [107] A. A. Osipov, L. M. Osipova, and V. E. Eremyashev, 'Structure of Alkali Borosilicate Glasses and Melts according to Raman Spectroscopy Data', vol. 39, no. 2, pp. 105–112, 2013, doi: 10.1134/S1087659613020119.
- [108] O. N. Koroleva, L. A. Shabunina, and V. N. Bykov, 'Structure of borosilicate glass according to raman spectroscopy data', *Glass Ceram. Engl. Transl. Steklo Keram.*, vol. 67, no. 11–12, pp. 340–342, 2011, doi: 10.1007/s10717-011-9293-0.
- [109] C. Le Losq, D. R. Neuville, P. Florian, G. S. Henderson, and D. Massiot, 'The role of Al³⁺ on rheology and structural changes in sodium silicate and aluminosilicate glasses

- and melts', *Geochim Cosmochim Acta*, vol. 126, pp. 495–517, 2014, doi: 10.1016/j.gca.2013.11.010.
- [110] D. Möncke, G. Tricot, A. Winterstein-Beckmann, L. Wondraczek, and E. I. Kamitsos, 'On the connectivity of borate tetrahedra in borate and borosilicate glasses', *Phys. Chem. Glas. Eur. J. Glass Sci. Technol. Part B*, vol. 56, no. 5, pp. 203–211, 2015, doi: 10.13036/17533562.56.5.203.
- [111] P. A. Bingham, R. J. Hand, O. M. Hannant, S. D. Forder, and S. H. Kilcoyne, 'Effects of modifier additions on the thermal properties, chemical durability, oxidation state and structure of iron phosphate glasses', *J. Non-Cryst. Solids*, vol. 355, no. 28–30, pp. 1526–1538, 2009, doi: 10.1016/j.jnoncrysol.2009.03.008.
- [112] X. Li, Z. Xiao, M. Luo, X. Dong, T. Du, and Y. Wang, 'Low melting glasses in ZnO-Fe₂O₃-P₂O₅ system with high chemical durability and thermal stability for sealing or waste immobilization', *J. Non-Cryst. Solids*, vol. 469, no. February, pp. 62–69, 2017, doi: 10.1016/j.jnoncrysol.2017.04.023.
- [113] K. Joseph *et al.*, 'Iron phosphate glass containing simulated fast reactor waste: Characterization and comparison with pristine iron phosphate glass', *J. Nucl. Mater.*, vol. 452, no. 1–3, pp. 273–280, 2014, doi: 10.1016/j.jnucmat.2014.05.038.
- [114] A. Moguš-Milanković, A. Gajović, A. Šantić, and D. E. Day, 'Structure of sodium phosphate glasses containing Al₂O₃ and/or Fe₂O₃. Part I', *J. Non-Cryst. Solids*, vol. 289, no. 1–3, pp. 204–213, Aug. 2001, doi: 10.1016/S0022-3093(01)00701-3.
- [115] S. I. Lopatin and V. L. Stolyarova, 'Thermodynamic properties and structure of gaseous metaborates', *Glass Phys. Chem.*, vol. 32, no. 3, pp. 353–369, May 2006, doi: 10.1134/S1087659606030163.
- [116] A. Büchler, J. L. Stauffer, and W. Klemperer, 'Electric-deflection studies of the geometry of some molecules containing cesium', *J. Chem. Phys.*, vol. 46, no. 2, pp. 605–608, 1967, doi: 10.1063/1.1840711.
- [117] R. C. Spiker and L. Andrews, 'Matrix reactions of alkali metal atoms with ozone: Infrared spectra of the alkali metal ozonide molecules', *J. Chem. Phys.*, vol. 59, no. 4, pp. 1851–1862, 1973, doi: 10.1063/1.1680270.
- [118] R. C. Spiker and L. Andrews, 'Matrix reactions of Na, K, Rb, and Cs atoms with N₂O: Infrared spectra and geometries of K₂O, Rb₂O, and Cs₂O', *J. Chem. Phys.*, vol. 58, no. 2, pp. 713–721, 1973, doi: 10.1063/1.1679258.
- [119] M. Asano and Y. Yasue, 'Mass spectrometric study of the vaporization of sodium borosilicate glasses', *J. Nucl. Mater.*, vol. 138, no. 1, pp. 65–72, Mar. 1986, doi: 10.1016/0022-3115(86)90256-4.
- [120] V. L. Stolyarova, 'High temperature mass spectrometric study of oxide systems and materials', *Rapid Commun. Mass Spectrom.*, vol. 7, no. 11, pp. 1022–1032, 1993, doi: 10.1002/rcm.1290071112.
- [121] D. W. Bonnell, E. R. Plante, and J. W. Hastie, 'Vaporization of simulated nuclear waste glass', *J. Non-Cryst. Solids*, vol. 84, no. 1–3, pp. 268–275, 1986, doi: 10.1016/0022-3093(86)90785-4.
- [122] A. A. Osipov and L. M. Osipova, 'Structure of Cs₂O-B₂O₃ glass and melts: The Raman spectroscopy data', *Glass Phys. Chem.*, vol. 40, no. 4, pp. 391–401, 2014, doi: 10.1134/S1087659614040075.

- [123] A. Band *et al.*, ‘Characterization of oxides of cesium’, *J. Phys. Chem. B*, vol. 108, no. 33, pp. 12360–12367, 2004, doi: 10.1021/jp036432o.
- [124] L. Andrews and R. C. Spiker, ‘Argon matrix raman and infrared spectra and vibrational analysis of ozone and the oxygen-18 substituted ozone molecules’, *J. Phys. Chem.*, vol. 76, no. 22, pp. 3208–3213, 1972, doi: 10.1021/j100666a018.
- [125] T. Livneh, A. Band, and R. Tenne, ‘Raman scattering from the peroxide ion in Cs₂O₂’, *J. Raman Spectrosc.*, vol. 33, no. 8, pp. 675–676, 2002, doi: 10.1002/jrs.900.
- [126] B. G. Parkinson, ‘Influence of Composition on Structure and Caesium Volatilisation from Glasses for HLW Confinement’, The University of Warwick, 2007.
- [127] M. Kodama and S. K. Kodama, ‘Raman scattering study of boson peaks in cesium borate glass’, *Jpn. J. Appl. Phys.*, vol. 33, no. 5S, pp. 2886–2889, 1994, doi: 10.1143/JJAP.33.2886.
- [128] B. N. Meera and J. Ramakrishna, ‘Raman spectral studies of borate glasses’, *J. Non-Cryst. Solids*, vol. 159, no. 1–2, pp. 1–21, 1993, doi: 10.1016/0022-3093(93)91277-A.
- [129] C. M. Gordon, W. F. Pearman, J. C. Carter, J. W.-J. Chan, and S. M. Angel, ‘Raman analysis of common gases using a Multi-pass Capillary Cell (MCC)’, Aug. 2008, no. September 2008, p. 70610L. doi: 10.1117/12.795586.
- [130] W. F. Pearman, J. C. Carter, S. M. Angel, and J. W. J. Chan, ‘Multipass capillary cell for enhanced Raman measurements of gases’, *Appl. Spectrosc.*, vol. 62, no. 3, pp. 285–289, 2008, doi: 10.1366/000370208783759650.
- [131] M. Hippler, ‘Cavity-Enhanced Raman Spectroscopy of Natural Gas with Optical Feedback cw-Diode Lasers’, *Anal. Chem.*, vol. 87, no. 15, pp. 7803–7809, 2015, doi: 10.1021/acs.analchem.5b01462.
- [132] R. C. Weast, *CRC Handbook of Chemistry and Physics*, 52nd ed. The Chemical Rubber Company.
- [133] K. Nakajima, T. Takai, T. Furukawa, and M. Osaka, ‘Thermodynamic study of gaseous CsBO₂ by Knudsen effusion mass spectrometry’, *J Nucl Mater*, vol. 491, pp. 183–189, 2017, doi: 10.1016/j.jnucmat.2017.05.001.
- [134] A. A. Osipov and L. M. Osipova, ‘Structure of Cs₂O-B₂O₃ glass and melts: The Raman spectroscopy data’, *Glas Phys Chem*, vol. 40, no. 4, pp. 391–401, 2014, doi: 10.1134/S1087659614040075.
- [135] M. D. Dyar, D. G. Agresti, M. W. Schaefer, C. A. Grant, and E. C. Sklute, ‘Mössbauer Spectroscopy of Earth and Planetary Materials’, *Annu. Rev. Earth Planet. Sci.*, vol. 34, no. 1, pp. 83–125, 2006, doi: 10.1146/annurev.earth.34.031405.125049.
- [136] P. A. Bingham, R. J. Hand, O. M. Hannant, S. D. Forder, and S. H. Kilcoyne, ‘Effects of modifier additions on the thermal properties, chemical durability, oxidation state and structure of iron phosphate glasses’, *J Non Cryst Solids*, vol. 355, no. 28–30, pp. 1526–1538, 2009, doi: 10.1016/j.jnoncrysol.2009.03.008.
- [137] K. Joseph, K. V. Govindan Kutty, P. Chandramohan, and P. R. Vasudeva Rao, ‘Studies on the synthesis and characterization of cesium-containing iron phosphate glasses’, *J. Nucl. Mater.*, vol. 384, no. 3, pp. 262–267, 2009, doi: 10.1016/j.jnucmat.2008.11.016.
- [138] N. J. Kim, S. H. Im, D. H. Kim, D. K. Yoon, and B. K. Ryu, ‘Structure and properties of borophosphate glasses’, *Electron. Mater. Lett.*, vol. 6, no. 3, pp. 103–106, 2010, doi: 10.3365/eml.2010.09.103.

- [139] S. T. Reis, W. M. Pontuschka, A. Moguš-Milanković, and C. S. M. Partiti, ‘Structural features of iron-phosphate glass’, *J. Am. Ceram. Soc.*, vol. 100, no. 5, pp. 1976–1981, 2017, doi: 10.1111/jace.14731.
- [140] R. K. Brow, ‘Review: the structure of simple phosphate glasses’, *J. Non-Cryst. Solids*, vol. 263–264, pp. 1–28, 2000.
- [141] S. T. Reis, M. Karabulut, and D. E. Day, ‘Chemical durability and structure of zinc-iron phosphate glasses’, *J. Non-Cryst. Solids*, vol. 292, no. 1–3, pp. 150–157, 2001, doi: 10.1016/S0022-3093(01)00880-8.
- [142] M. H. Langowski, J. G. Darab, and P. A. Smith, ‘Volatility literature of chlorine, iodine, cesium, strontium, technetium, and rhenium; technetium and rhenium volatility testing’, Richland, WA, Mar. 1996. doi: 10.2172/211388.
- [143] M. Neyret, M. Lenoir, A. Grandjean, N. Massoni, B. Penelon, and M. Malki, ‘Ionic transport of alkali in borosilicate glass. Role of alkali nature on glass structure and on ionic conductivity at the glassy state’, *J. Non-Cryst. Solids*, vol. 410, pp. 74–81, 2015, doi: 10.1016/j.jnoncrysol.2014.12.002.
- [144] N. Chouard *et al.*, ‘Thermal stability of SiO₂-B₂O₃-Al₂O₃-Na₂O-CaO glasses with high Nd₂O₃ and MoO₃ concentrations’, *J. Alloys Compd.*, vol. 671, pp. 84–99, 2016, doi: 10.1016/j.jallcom.2016.02.063.
- [145] N. J. Cassingham, C. L. Corkhill, M. C. Stennett, R. J. Hand, and N. C. Hyatt, ‘Alteration layer formation of Ca- and Zn-oxide bearing alkali borosilicate glasses for immobilisation of UK high level waste: A vapour hydration study’, *J. Nucl. Mater.*, vol. 479, pp. 639–646, 2016, doi: 10.1016/j.jnucmat.2016.06.009.
- [146] E. R. Vance *et al.*, ‘The influence of ZnO incorporation on the aqueous leaching characteristics of a borosilicate glass’, *J. Nucl. Mater.*, vol. 494, pp. 37–45, 2017, doi: 10.1016/j.jnucmat.2017.06.035.
- [147] J. Sułowska, I. Waclawska, and M. Szumera, ‘Comparative study of zinc addition effect on thermal properties of silicate and phosphate glasses’, *J. Therm. Anal. Calorim.*, vol. 123, no. 2, pp. 1091–1098, 2016, doi: 10.1007/s10973-015-5044-8.
- [148] A. B. ROSENTHAL and S. H. GAROFALINI, ‘Structural Role of Zinc Oxide in Silica and Soda-Silica Glasses’, *J. Am. Ceram. Soc.*, vol. 70, no. 11, pp. 821–826, 1987, doi: 10.1111/j.1151-2916.1987.tb05634.x.
- [149] D. G. Minser, B. Walden, and W. B. White, ‘Structure of Alkali-Zinc Silicate Glasses by Raman Spectroscopy’, *J. Am. Ceram. Soc.*, vol. 67, no. 3, p. C-47-C-49, 1984, doi: 10.1111/j.1151-2916.1984.tb19753.x.
- [150] V. L. Stolyarova, S. I. Lopatin, O. L. Belousova, and L. V. Grishchenko, ‘Phase equilibria and thermodynamic properties of components in the Cs₂O-B₂O₃-SiO₂ system at high temperatures’, *Glass Phys. Chem.*, vol. 32, no. 1, pp. 55–62, 2006, doi: 10.1134/S108765960601007X.
- [151] S. V. Stefanovsky and J. J. Purans, ‘Cesium speciation in nuclear waste glasses’, *Phys. Chem. Glas. Eur. J. Glass Sci. Technol. Part B*, vol. 53, no. 5, pp. 186–190, 2012.

11 Appendix

11.1 Appendix A

Below is the MATLAB script used to read the .txt files outputted from the off-gas spectrometer software. The script reads both columns of data within the .txt file and adds it to a MATLAB table. The script also applies a wavenumber correction as can be seen in line 5 ($X = A\{:,1\} + 23.3$).

```
data = dir('*.*txt');
N = numel(data);
T = zeros(1044,N);
A = readtable(data(1).name);
X = A{:,1}+23.3;

for i = 1:N
    Y = readtable(data(i).name);
    T(:,i) = Y{:,2};
end

%end of data read
```

11.2 Appendix B

Figure 11.1 shows an example of the data collected during a standard NaBS experiment. It can be seen that several peaks vary with time, something that could be further interrogated in future work.

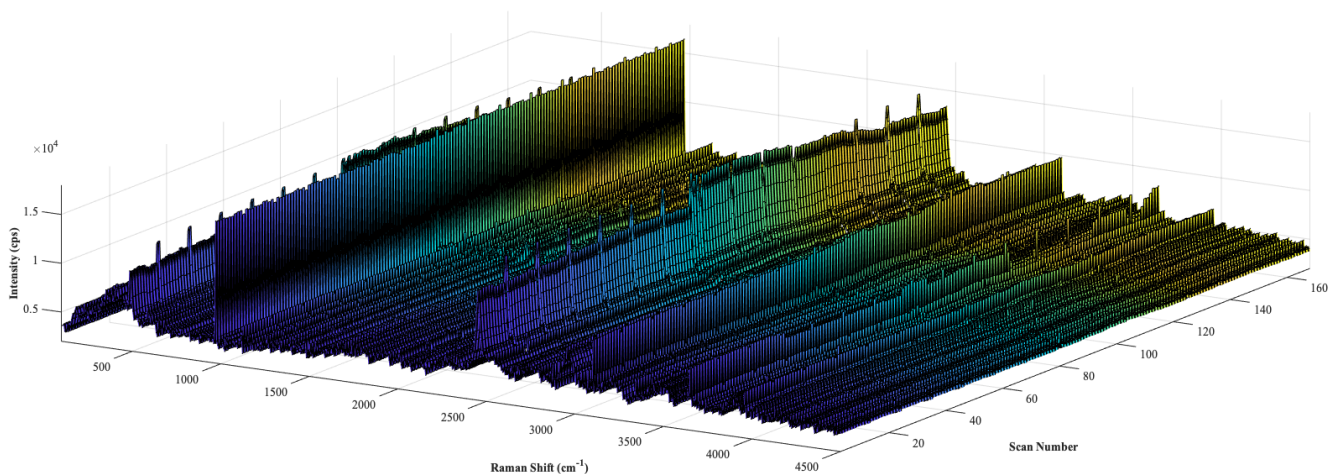


Figure 11.1: NaBSZn60Ca40Cs2 off-gas Raman spectra plotted in 3-dimensions to show intensity variation with time

11.3 Appendix C

Thermal analysis of the caesium carbonate used for all the experiments shown in Chapters 5,6 and 7 is shown in Figure 11.2. It can be seen that the drying temperature of 120 °C is sufficient to ensure the removal of any H₂O prior to batching.

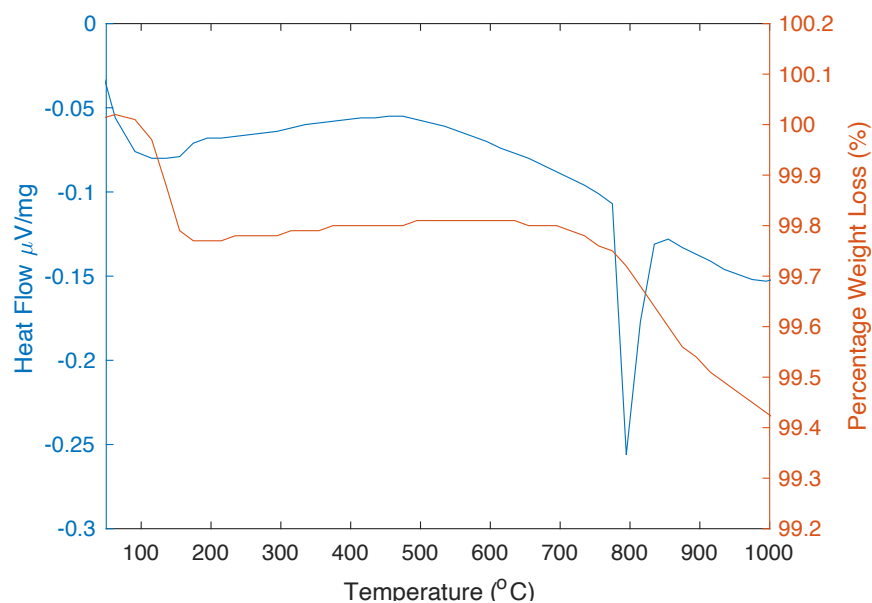


Figure 11.2: Thermal analysis of Cs₂CO₃